THE UNIVERSITY OF CALGARY

MIXING OF AN ACOUSTICALLY EXCITED AIR JET WITH A CONFINED HOT CROSSFLOW

BY

PIOTR GRABINSKI

A THESIS

SUBMITTED TO THE FACULTY OF GRADUATE STUDIES

IN PARTIAL FULFILLMENT OF THE REQUIREMENTS FOR THE

DEGREE OF MASTER OF SCIENCE

DEPARTMENT OF MECHANICAL ENGINEERING

CALGARY, ALBERTA

APRIL, 1990

THE UNIVERSITY OF CALGARY

FACULTY OF GRADUATE STUDIES

The undersigned certify that they have read, and recommend to the Faculty of graduate Studies for acceptance, a thesis entitled, "Mixing of an acoustically excited air jet with a confined hot crossflow" submitted by Piotr Grabinski in partial fulfillment of the requirements for the degree of Master of Science.

Dr. Reader, G.
Chairman
Department of Mechanical
Engineering

Dr. Walker, G.
Department of Mechanical
Engineering

Dr. Wierzba, I.
Department of Mechanical
Engineering

Dr. Jeje, A.
Department of Chemical and
Peroleum Engineering

Date: April 26, 1990

ABSTRACT

This thesis presents a study of the mixing characteristics of an acoustically modulated jet with a confined hot uniform crossflow.

The experiments were performed in two stages; investigation of the effects of the acoustic excitation level of the jet, and the Strouhal number influence on the mixing ability of the jet with the crossflow. The first stage was carried out near the optimum Strouhal number condition as indicated by a previous "cold flow" study, whilst the second stage attempted to find the optimum Strouhal number response independent of other main variables such as momentum flux ratio, excitation level and temperature.

The mixing of the acoustically pulsed air jet with the confined hot crossflow was assessed by temperature profile measurements. These novel experiments were designed to examine the effects of acoustic driver power and Strouhal number on jet structure, penetration and mixing. The results showed that excitation produced strong changes in the measured temperature profiles. This resulted in significant increases in mixing, mixing zone size, and jet penetration (at least 100% increase). The length to achieve a given mixed state was shortened by at least 70%. There was strong modification to the jet-wake region. The jet response as determined by penetration and mixing was optimum at a Strouhal number of 0.27. Overall, pulsating the jet flow significantly improved the jet mixing processes in a controllable manner.

ACKNOWLEDGEMENTS

The author is greatly indebted to his supervisor Dr. P.J.Vermeulen who supervised this research. His continued interest, discussions and suggestions, guidance, support and encouragement are gratefully acknowledged.

The author is also indebted to Dr. V. Ramesh, Research Associate; Mr. R. Bechtold, Chief Technical Supervisor; Mr. W. Crews, Mr. G. East, Mr. A. Moehrle Mr. R.W. Gustafson and Mr. B. Sanders, Technicians, for their careful work in building and operation of the test rig. The author's special gratitude is extended to Mr. L. Raciborski, Research Associate, for valuable help with data acquisition and computer programming.

Canadian Western Natural Gas Co., Ltd., generously supplied the natural gas for operation of the test rig.

The work was supported financially by the Natural Sciences and Engineering Research Council of Canada, under Grant No. A7801.

TABLE OF CONTENTS

LIST OF TABLES

LIST OF FIGURES

NOMENCLATURE

(SI units used throughout to establish numerical values)

a	- jet thermal axis, point where $\Theta = \Theta max$
A_j	- area of the jet exit orifice
A_∞	- cross-sectional area of the test section
D	- jet orifice diameter
DIA.	- diameter
f	- driving frequency
F, F_1	- functions
FFT	- fast Fourier transform
F.S.D.	- full scale deflection
H	- tunnel height or position of maximum on contour maps
I.DIA.	- inside diameter
j	- approximate boundary of the jet-wake zone
J	- momentum flux ratio, i.e. $J = (\rho_j V_j^2)/(\rho_\infty U_\infty^2)$
L	- position of minimum on contour maps
Ma	- Mach number
$\dot{M}_f$	- main mass flow rate measured by Pitot-tube flow meter
$\dot{M}_j$	- constant average mass flow rate through the jet orifice
$\dot{M}_\infty$	- constant average crossflow mass flow rate
n	- number of data points
O.DIA.	- outside diameter
p	- pressure
p_a	- atmospheric pressure

p_f	-	static pressure of the flow at the Pitot tube flow meter
p_j	-	static pressure of the jet at the orifice exit
p_r	-	static pressure of the flow at the jet orifice meter
p_∞	-	crossflow static pressure at X/D = -2.23, Y/H = 0.5, Z/D = 2.26
Δp_f	-	differential pressure at the Pitot tube flow meter
Δp_r	-	differential pressure at the jet orifice meter
R	-	specific gas constant
Re_j	-	Reynolds number of jet at the orifice
Re_∞	-	Reynolds number of crossflow based on hydraulic diameter
S_m	-	standard deviation for mixing effectiveness
ΔS_m	-	change in standard deviation for mixing effectiveness caused by acoustic excitation
St	-	jet Strouhal number at the jet orifice, $St = fD/V_j$
T	-	local mean stagnation temperature (due to low velocity is closely static temperature)
T_f	-	temperature of the flow at the Pitot tube flow meter
T_j	-	temperature of the jet flow at the orifice exit
T_m	-	average temperature in a particular transverse plane
T_r	-	temperature of the flow at the jet orifice meter
T_{set}	-	setting reference mean temperature at X/D = 0.0, Y/H = 0.65, Z/D = 0.0
T_∞	-	crossflow local mean temperature in the reference transverse plane at X/D = -1.43

$\bar{T}_{\infty}$	- reference plane average temperature
U	- local mean velocity in XY plane at a particular X locatiom
U_{∞}	- average crossflow velocity at the reference transverse plane
V	- voltage (volts)
V_e	- jet velocity excitation pulsation amplitude, or pulsation strength, at the orifice exit plane centre (unsteady flow)
V_j	- steady mean jet velocity at the orifice exit plane
$\dot{W}$	- power at acoustic driver
X, Y, Z	- rectangular coordinates, see Fig. 3.1 for origin location
$Y_{\circ}$	- jet penetration without acoustic driver at a particular X location
ΔY	- change in jet penetration, caused by acoustic excitation, at a particular X location
Θ	- dimensionless temperature difference ratio
Θ_m	- dimensionless relative temperature or mixing parameter
Θmax	- maximum value of Θ
ρ_j	- density of the jet flow at the orifice exit plane
ρ_f	- density of the flow at the Pitot-tube flow meter
ρ_r	- density of the flow at the jet orifice meter
ρ_{∞}	- crossflow density at X/D = -2.23
NW	- difference between "no drive" and "with drive" conditions

CHAPTER 1

INTRODUCTION

1.1 PROLOGUE

Jets in a crossflow are of great practical relevance in a variety of engineering applications. The simplest and most common examples are smoke plumes rising from chimneys, a flare from the safety system of a petroleum plant, or waste disposal into water bodies. Some more technically advanced examples can be found in gas turbines for instance mixing jets in combustors, or V/STOL aircraft in transition flight configuration.

Whenever jet injection into a crossflow is considered, there is the same technical problem related to the prediction of the jet behaviour as to penetration and mixing and to its control. However, this problem is well documented in the literature and techniques have been sought for a way to control these phenomena. The problem of the control of jet behaviour is generally one of modifying a turbulent shear layer. Published results of laboratory experiments have established that even apparently chaotic flow fields can contain deterministic, non random elements. Moreover, recent studies on jets, wakes, boundary layers, and separated flow, have proved that acoustic excitation of these coherent structures has a significant effect on the mixing characteristics of the shear layers. Therefore, controlled modification of jet behaviour in a crossflow is expected to be achieved by the application of acoustic excitation.

The benefits from this study could be an improvement in the jet mixing process and therefore in better combustor design (typical combustor Fig. 1.1). The effectiveness of the "jet mixing process" is vital to combustor performance. First of all, in the primary zone, an improvement in mixing could result in better efficiency of combustion; a higher burning rate, lower soot and oxides of nitrogen pollutants formation. This could accelerate soot oxidation and conversion of any dissociated products of combustion into normal products of combustion in the secondary zone. Finally, in the dilution zone, an improved mixing process may promote the better achievement of the required temperature profile at the combustor exit.

1.2 ORIGIN OF THE PRESENT WORK

Although, the effect of excitation on jets, boundary layers and separated flows has been quite widely investigated by flow mechanics scientists, the study of the behaviour of excited jets in a confined crossflow has only recently been conducted at the University of Calgary. This research on acoustically excited jets, with application to combustor design, has been a long term goal of studies performed under Dr Vermeulen's supervision (Refs. 1 to 8). The overall results prove that the acoustic excitation of jets results in significant improvement of the entrainment rate and mixing behaviour. These effects were proven by work on free jet behaviour and led to the study of jet penetration into a cold crossflow. The new work of this thesis on a jet penetrating into a hot crossflow is a continuation of these previous studies (Refs. 1 and 2). The "cold flow" study was based on velocity and turbulence profiles of the jet/crossflow, whilst the "hot flow" studies are based on the jet/crossflow temperature profiles measurements. The overall results lead to a better understanding of this phenomenon and its application to new combustor design. A preliminary study of this application has already been done by Vermeulen (Refs. 6, 7 and 8; Fig. 1.2), which showed the beneficial influence of acoustic excitation on the mixing processes in the dilution zone of a combustor.

1.3 SCOPE OF THE THESIS

The experimental work presented in this thesis consists of studies of the mixing characteristics of an acoustically modulated jet with a confined hot uniform crossflow by means of temperature profile measurements.

The experiments were performed in two stages; investigation of the effect of the acoustic excitation level of the jet, and the Strouhal number influence on the mixing ability of the jet with the crossflow.

The first stage was carried out near the optimum Strouhal number condition indicated by the previous "cold flow" study (Refs. 1 and 2), whilst the second attempted to find the optimum Strouhal number response independent of other main variables such as momentum flux ratio, excitation level and temperature.

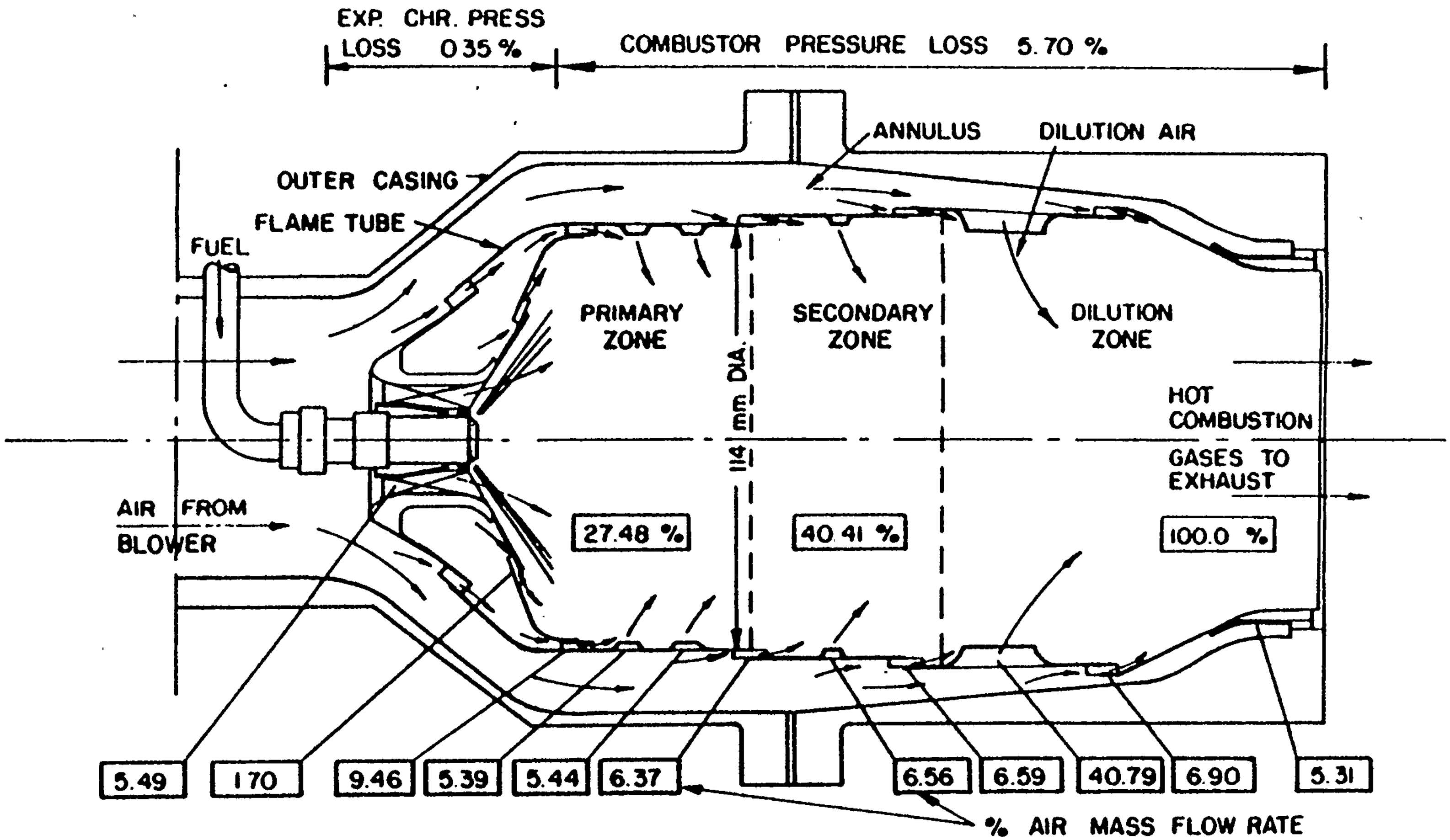

Fig. 1.1 Cross Section of Typical Tubular Combustor Chamber Showing the Air Distribution (from Ref. 6).

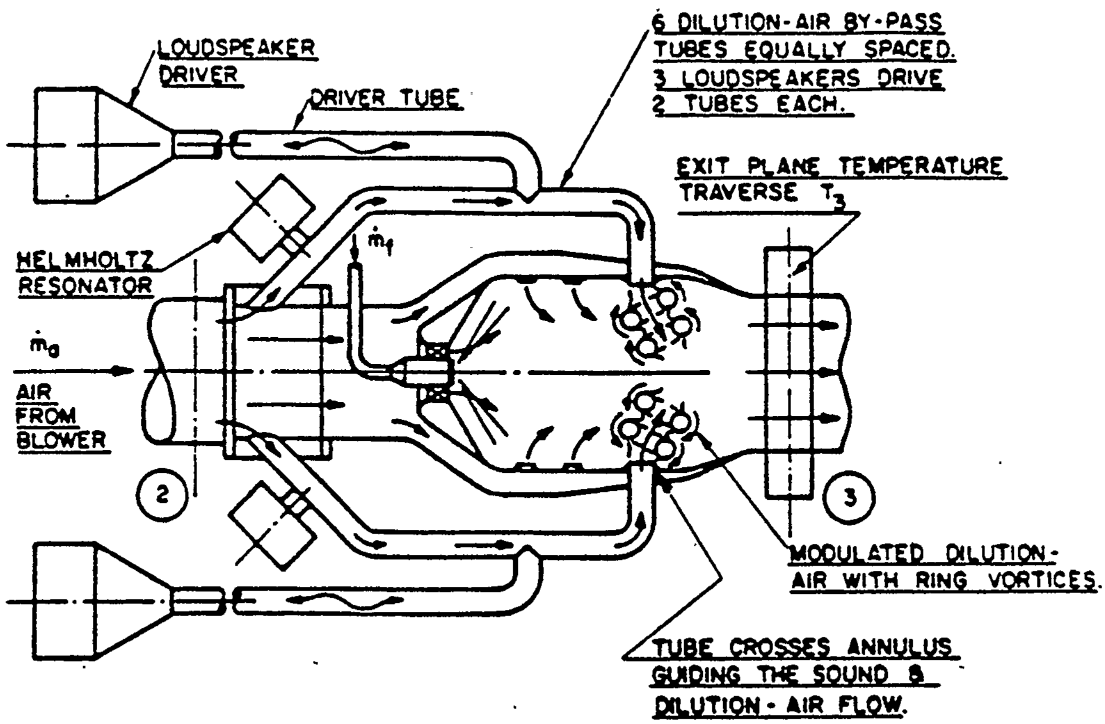

Fig. 1.2 Schema of Acoustically Controlled Dilution Mixing Processes (from Ref. 7).

CHAPTER 2

LITERATURE STUDIES

The main purpose of this research was to experimentally study the behaviour of an acoustically excited air jet mixing with a confined hot crossflow. As such, current knowledge on unexcited and excited free jets and jets mixing with a crossflow is most important. Thus the goal of this literature review is to present an up to date summary of scientific achievements in these fields. The review is concluded by the presentation of the results of recent experiments on acoustically excited jets in a cold crossflow and their practical application to the turbojet combustor.

2.1 CHARACTERISTICS OF NON-EXCITED GASEOUS JETS IN CROSSFLOW

The mixing of steady free gaseous jets and steady gaseous jet mixing with a confined crossflow have been extensively studied. For instance Abramovich (Ref. 15) and Lefebvre (Ref. 14) present experimental and theoretical predictions of jet behaviour in a crossflow.

Flow-visualization studies led to the description of the jet-in-crossflow flow pattern, while the quantitative description of this phenomenon resulted from velocity, turbulence and temperature field measurements.

The three-dimensional representation of the jet-in-crossflow flow pattern is shown in Fig. 2.1 (from Moussa, Ref. 9). The most obvious feature is the mutual deflection of both jet and crossflow. The jet is bent over by the cross-stream while the latter is deflected as if it were blocked by a rigid obstacle. The jet interacts with the deflected flow and entrains fluid from it. Right from the outlet section, at which the velocity profile is relatively uniform and the turbulence intensity is low, the jet undergoes strong shearing owing to the velocity gradient. The sides of the jet, which possess less momentum, are displaced towards the rear forming bound vortices (Fig. 2.1). As long as the jet possesses a relatively high energy, it constitutes a real obstacle for the external flow. Therefore, the flow pattern in this region is similar to that around a circular cylinder. The main flow retards along the upstream side of the jet causing a pressure rise, then bends around the jet column and separates downstream forming a lower pressure wake zone. This flow pressure distribution provides the force necessary to deflect and deform the jet. The interaction of the crossflow wake zone with the jet bound vortices results in an intensive intermixing and forms the characteristic "horseshoe" or "kidney" shape of the jet cross section based on velocity or temperature profiles.

According to Chassing (Ref. 10, Fig. 2.2), the following three zones can be distinguished in the evolution of the jet in the presence of a crossflow;

(1) - zone of residual inlet velocity

(2) - zone of accommodation

(3) - zone of velocity profile similarity.

The boundary of the residual inlet velocity zone is defined by the remains of the jet potential core. The jet in this zone is characterized by a relatively uniform velocity profile and the mixing process is confined only to the outer circumference part of the jet. The process of entrainment results in the spread of the jet which is, however, less extensive than for the same free jet. The initiation of the jet curvature causes the existing core to become asymmetrical.

The zone of accommodation starts when the maximum axial velocity begins to decrease (where the entire jet section participates in the turbulent mixing process). Moreover, this zone is characterized by increase of the jet curvature and obvious appearance of the wake region.

The zone of velocity profile similarity appears when a law of similarity can be established for the velocity profiles.

The delineation of the jet boundary in a crossflow is shown in Fig. 2.3, taken from Bojic, Ref. 11. This figure describes the flow region at X/D=2.0 distance downstream from the jet outlet in terms of dimensionless velocity and turbulence intensity. Peaks of the turbulence intensity describe various flow field regions. The jet region is clearly defined between the peaks of turbulence intensity, and its centre by maximum velocity. Also the vortex region could be distinctly separated from the wake and the jet region. The free-stream region is characterized by the lowest turbulence level and by its relatively uniform velocity.

The flow pattern of the jet-in-crossflow described above is for a relatively high jet-to-crossflow velocity ratio and therefore of quite uniform velocity profile at the jet outlet. However, detailed study by Andreopoulos (Refs. 12 and 13) has shown that at conditions of low jet-to-crossflow velocity ratio, the jet exit velocity is significantly distorted by the crossflow. Thus for a jet-to-crossflow velocity ratio of 0.5, the crossflow can penetrate up to a distance of 3-diameters into the jet orifice, causing radical distortion of the jet velocity profile at the outlet. As result, the near field in such a condition undergoes modification, and the jet streamlines are bent while still in the discharge tube.

In general, the behaviour of a jet in a crossflow is influenced mainly by the following factors (from Lefebvre, Ref. 14):

- geometry of the jet outlet and the crossflow duct,
- initial angle of jet penetration,
- jet to crossflow velocity ratio,
- jet to crossflow density ratio,

- jet turbulence properties,
- inlet velocity profile of the jet and the crossflow.

These research studies were performed in different thermal conditions, i.e in either cold or preheated jet or crossflow.

The cold flow analytical approach is based mainly on the jet-to-crossflow velocity ratio since there is no density difference in the flow. However, for temperature and the resulting density difference between jet and crossflow the momentum flux ratio $J=(\rho_j V_j^2)/(\rho_\infty U_\infty^2)$ (Lefebvre and Norster Ref. 14, Abramovich Ref. 15, Fearn Ref. 16, Kamotani Ref. 17, Holdeman Ref. 18) or blowing rate $(\rho_j V_j)/(\rho_\infty U_\infty)$ (injection rate; Andreopoulos Refs. 12 and 13) are more appropriate, accounting in one form for both velocity and density ratios. Therefore, most of the analytical flow predictions use the jet-to-crossflow momentum flux ratio as the main characteristic parameter.

2.2 CHARACTERISTICS OF EXCITED GASEOUS FREE JETS

Studies on acoustic excitation of jets are very diversified. Mainly, interest has been focused on the investigation of:

- large structure generation in a free jet,
- vortex creation,
- jet noise generation or suppression,
- shear layer instability,

- properties of acoustically excited jets (entrainment rate and mixing).

Since the main focus of the present work was oriented towards the application of these phenomena to gas turbines, and more precisely to combustor design, this literature survey pays special attention to the behaviour and properties of excited subsonic jets.

Research on the structure of axisymmetrical turbulent jets has been a long term subject in fluid dynamics. Observations have detected a large-scale pattern existing in the jet structure under certain flow conditions (Michalke Ref. 19, Browand and Laufer Ref. 20, Sarohia Ref. 21, Yule Ref. 22, Ho Ref. 23). These works provide evidence of increased mixing effects due to the existence of large scale structures in the jet. It was found that this disturbance mode of the jet column depends upon the boundary layer thickness, which is associated with the Reynolds number and the jet orifice geometry (Refs. 19, 20 and 23). The first theoretical approach to the problem of the existence of large-scale structures in the flow, based on shear layer stability, was done by Michalke (1971, Ref. 19). Crow and Champagne (Ref. 24) stated that as the Reynolds number increases from 10^2 to 10^3, the instability of the jet evolves from a sinusoid to a helix, and finally to a train of axisymmetric waves. At a Reynolds number of approximately 10^4, they distinguished two kinds of axisymmetric structures: surface ripples on the jet column, and a more tenuous train of large-scale vortex puffs. This observation was later confirmed by Ito and Seno (Ref. 25) in experiments also involving an investigation of the effect of exit geometry on jet behaviour. The phenomenon of jet noise provided some evidence of natural organized structures in jets (Anderson Refs. 26 and 27) and led Crow and Champagne (Ref. 24) to a detailed investigation of this problem. This observation directed them to the search for a large-scale pattern in acoustically excited jets. The visualization of excited jets confirmed their assumption. Moreover, the extremum mode of jet behaviour was found at a Strouhal number of St=0.3 (based on frequency, exit speed and diameter). This mode relates to the largest increase of spreading angle, volume flow and decay of centre-line velocity of the jet. This phenomenon was explained by the existence of a violent coalescence of vortex rings supposedly responsible for the production of subharmonics in the mixing layer (Anderson Refs. 26 and 27, and Petersen Ref. 28). In summary two instability mechanisms are possible (Refs. 24, 26, 27, Kibens Ref. 29, Becker and Massaro Ref. 30); the first one involves the initial thin laminar boundary layer, which develops waves before rolling up into toroidal vortices on progression along the jet, and the second occurs when the boundary layer is turbulent and cannot sustain oscillations, whereas the jet column can, and on excitation develops wave motion growing into a train of toroidal vortices.

Detailed information on vortex shedding and coalescence modes for different Strouhal number regimes of excited jets was recently presented by Seno, Kageyama and Ito (Ref. 31). This experiment was performed with water with the use of a special pulse generator having close to harmonic characteristics. For a non-excited (natural) jet, they confirmed that the frequency and position of vortex ring formation depends upon Reynolds number. They also found that the position of the vortex coalescence for a natural jet to be random in the range $1 \leq X/D \leq 3$ for $1700 \leq Re \leq 8000$, while for pulsed jet, there was correlation with Strouhal number with $X/D = 1.2 St^{-1}$. The position of vortex ring formation for the pulsed jet was closer to the exit ($X/D<1$) and independent of Re and St. When the Strouhal number was $St<0.9$, they observed that each large vortex ring induced by the pulsation at the jet exit was followed by up to three smaller vortex rings (especially for larger Re, experimental range $2000 \leq Re \leq 6000$) caused by fluctuations on the annular shear layer due to the preceding larger one. They observed the coalescence of the large ring with the smaller trailing vortex ring, resulting in the rapid disintegration of the large vortex ring into turbulent eddies. In the next regime of $0.9 \leq St \leq 2.6$ they observed equal size vortex rings shedding at the same periodic intervals as the pulsation. The coalescence of up to three following rings was observed in this regime. The final regime of $St \geq 2.6$ resembled the mode of a non-excited jet. However, the pulsation caused the vortex rings to be created closer to the jet exit. In summary, they stated that at $St=0.3$ the spreading of the jet and the decay of the centre-line velocity were more abrupt than at other Strouhal numbers. This result supports the conclusion of the Crow and Champagne experiments performed in a gaseous environment (Ref. 24). The velocity pulsation amplitude or pulsation strength was observed to have little effect on the position of vortex ring formation and none on frequency of formation. It also had no effect on the pattern of vortex ring coalescence. For large amplitudes more clearly distinct vortex rings were formed.

An interesting experimental study on vortex ring creation was done by Maxworthy (Ref. 32), who showed that the mechanism of excitation was associated with the creation of two kinds of vortices shed in opposite directions and with opposite circulation, i.e. a positive vortex, traveling with the flow and associated negative one, shed from the lips of the jet orifice into the jet tube. The evidence of sink type flow at the jet orifice in the presence of acoustic excitation was also confirmed by Disselhorst and van Wijngaarden (Ref. 33) and Vermeulen in studies on an acoustically excited flame (Ref. 34).

From a gas turbine aspect, quantitative studies on the mixing of excited jets are of major importance. Following Crow and Champagne, various scientists observed an increase in jet entrainment rate due to excitation (Vermeulen Refs. 2, 3 and 5, Sarohia and Massier Ref. 21, Yule Ref. 22, Crow and Champagne 24, Binder and Favre-Marinet Ref. 35). The overall achievements indicate a significant increase in entrainment due to excitation. Particularly studies carried out by Vermeulen, Ramesh and Yu (Ref. 3) surpassed the previous results derived from velocity profiles (Refs. 5, 8, 21 and 35) Their experiments were based on the method of entrainment measurement developed by Ricou and Spalding (Ref. 36). The experiments confirmed an improvement in entrainment rate by the considerably large factor of 5.6 at X/D>15 (distance from orifice) for a Strouhal number of 0.274 (orifice 6.35 mm DIA.) and a driver power of 16 W. They also showed nonlinearity (saturation effect) of the jet response with the pulsation strength and estimated the optimum response at a Strouhal number of 0.25.

2.3 STUDY OF ACOUSTICALLY EXCITED JET BEHAVIOR IN A CROSSFLOW

The entrainment and mixing properties of acoustically excited jets indicate the possibility of favourable application to combustor design. This possibility requires an additional investigation of the behaviour of acoustically excited jets in the presence of a crossflow. The first study was done by Vermeulen, Chin and Yu (Refs. 1 and 2). The experimental studies were performed in "cold-flow" conditions; therefore, the results were based on the analysis of mean velocity and turbulence profiles for different pulsation strength and Strouhal number conditions. The results showed significant improvement in jet spread, penetration (up to 92%; Fig. 2.4) and mixing, with saturation tendencies at higher excitation levels. The optimum response was obtained at an estimated Strouhal number St of 0.22, which is some 12% smaller than that previously assessed in the free jet experiment. The overall results proved the possibility of acoustic control of mixing processes by means of jet excitation. The studies on excited jets in "cold" and "hot" crossflows (work of this thesis) will help to define the optimal operational regimes of an acoustically controlled gas turbine combustor which has already been designed at the University of Calgary (Refs. 6 and 7; Figs. 1.1 and 1.2). Preliminary experiments on this combustor successfully showed the possibility of controlling the combustor exit temperature profile by means of acoustically driving the dilution air jets (Refs. 6, 7).

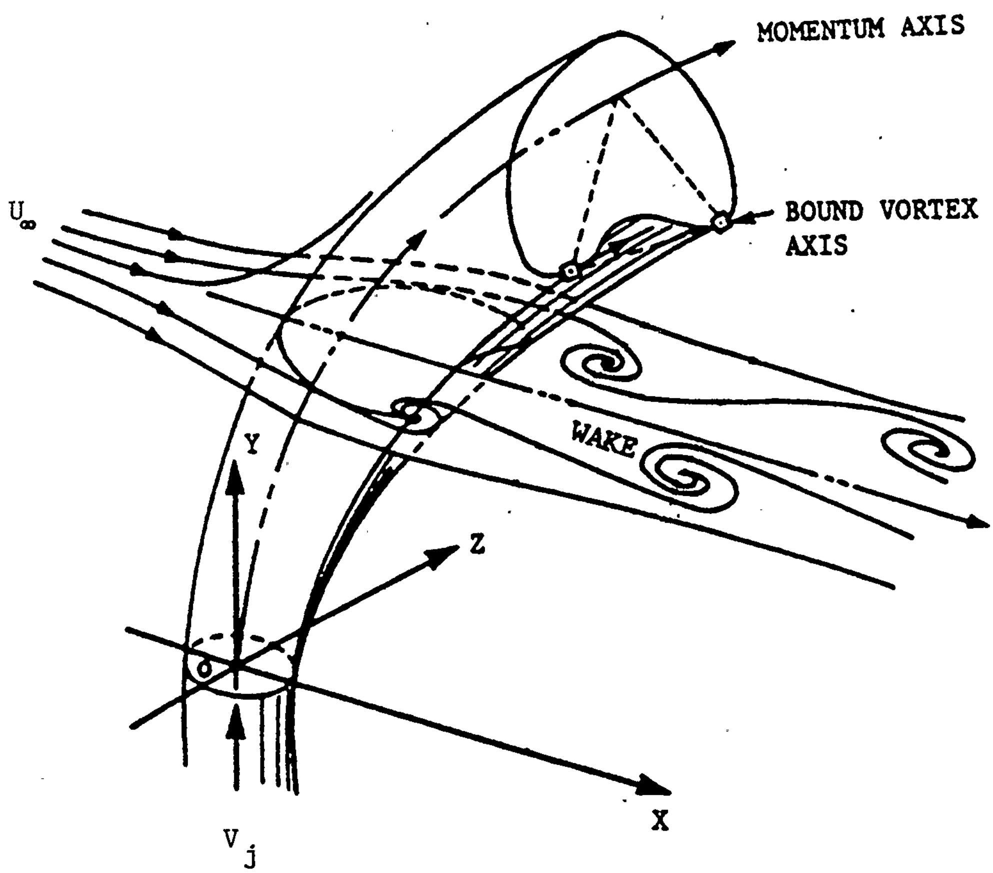

Fig. 2.1 Jet in Crossflow, Three-Dimensional Sketch (from Ref. 9).

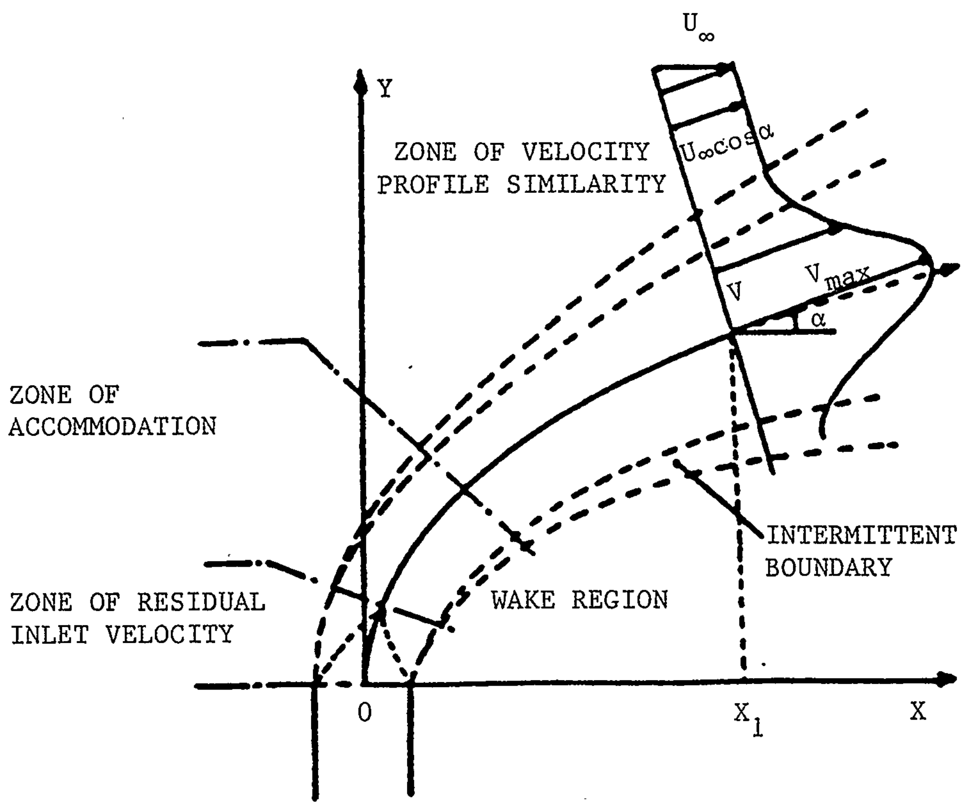

Fig. 2.2 Configuration of the Jet Flow in the Plane of Symmetry (from Ref. 10).

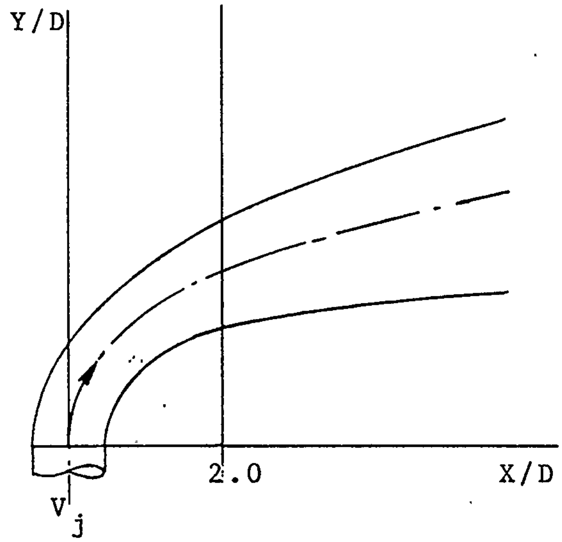

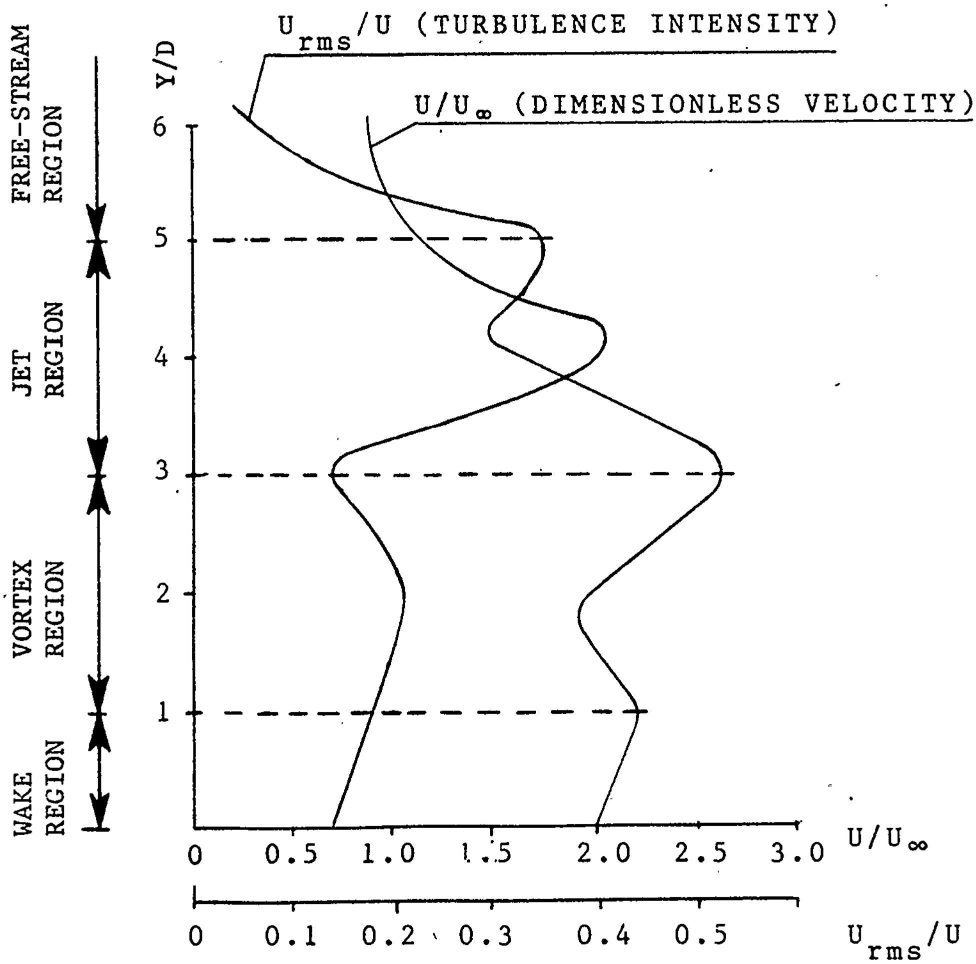

Fig. 2.3 The Delineation of Jet Boundaries in a Crossflow

for X/D=2.0, Z/D=0.0 (from Ref. 11)

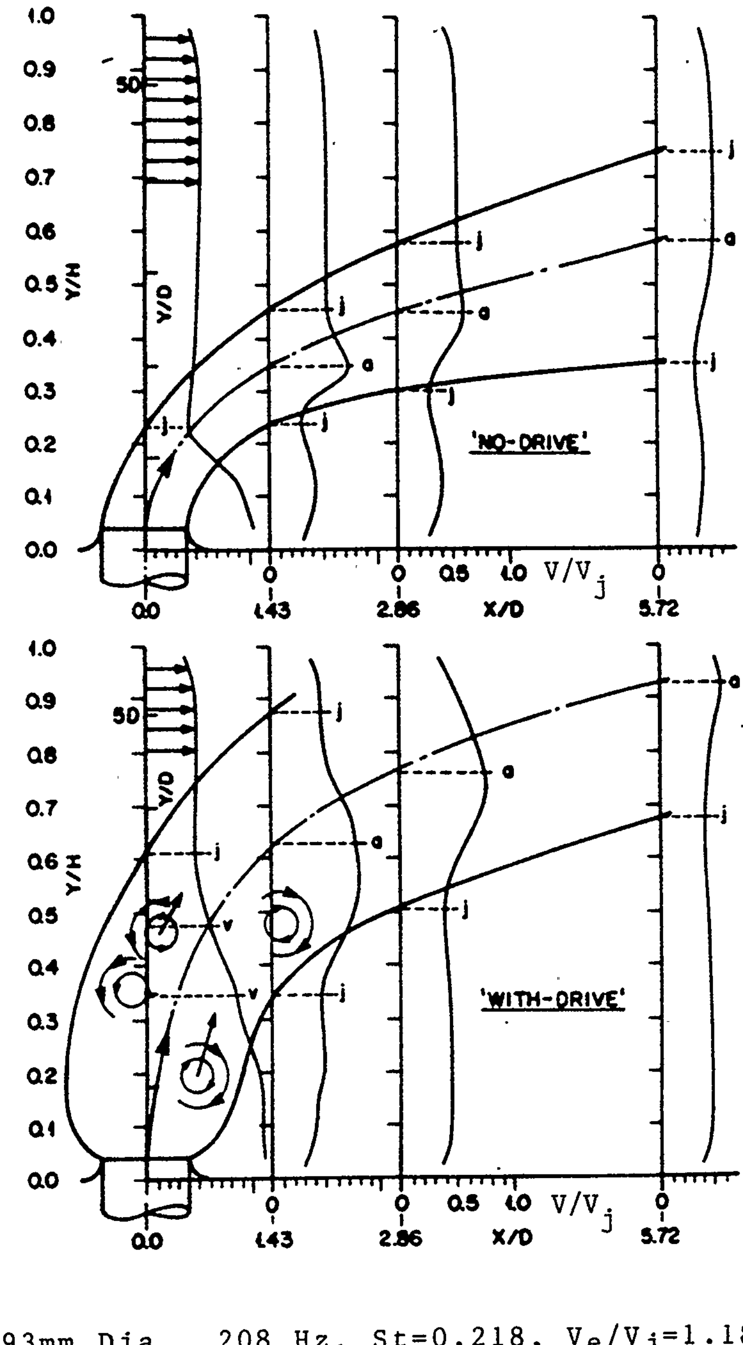

D=19.93mm Dia., 208 Hz, St=0.218, V_e/V_j=1.18

Fig. 2.4 Structure of Jet in Cold Crossflow, V_j=19.0 m/s, V_j/U_∞=1.93, 75.3W (from Ref. 2).

CHAPTER 3

EXPERIMENTAL APPARATUS

The experimental set-up, Fig. 3.1(a), (b) and (c) is basically the same as that used for the previous "cold flow" study (Refs. 1 and 2). The difference consists of the built-in required heating system for the crossflow. The overall set-up can be subdivided as follows;

(1) - air delivery system,

(2) - crossflow assembly,

(3) - jet flow assembly,

(4) - acoustic excitation system,

(5) - test section,

(6) - exhaust system.

3.1 THE AIR DELIVERY SYSTEM

The air flow requirements are fulfilled by a centrifugal blower driven by a 56 kW induction motor. The blower was able to supply the air to a 203 mm I.DIA. pipe system at a rate of about 2.5 kg/s at 3560 rpm. However, the changes necessary to meet the flow experimental conditions (i.e. mounting a heating combustor and flow straighteners), cause additional pressure losses in the system, reducing the maximum flow rate to about 0.9 kg/s.

The air delivery pipe system, because of laboratory space constraints, was constructed so that the longest straight section preceded the Pitot-tube flow meter (about 12 pipe diameters). Thus, the air flow from the blower transition section is directed through four pipe bends (Figs. 3.1(a) and 3.2(a)) prior to the straight section. At the start of the straight section 8 fine screens and a honey cone flow straightener, about 0.3 m long, were mounted. This precaution was taken in order to ensure steady flow in the flow meter section. The rate of flow delivery was regulated by a throttle valve mounted between the first and second bends downstream from the blower.

The Pitot-tube flow meter (Fig. 3.2(b) and 3.3) is an integral part of the pipe system and consists of a pipe segment with a set of four static pressure taps and four built-in Pitot-tube rakes of five tubes each. The Pitot-tube rakes form two sets of ten tubes placed on two perpendicular diameters. The flow meter dimensions are according to the ten-point log-linear method specified by B.S.1042; Part 2A (Ref. 37). This is a Class A accuracy flow meter (including pipe roughness up to a sand roughness of one-thirtieth of the pipe diameter) resulting in a mean-square error of about 0.5 %. This accuracy applies even to measurements of pipe flow that is not fully developed, or of irregular, even markedly asymmetric, velocity distribution.

The flow meter is followed by a flow divider (Figs. 3.1(a) and 3.2(b)). This element splits the flow into three streams, the main crossflow and two identical, top and bottom, by-pass streams, for creation of the jet flows. The 50mm I.DIA. by-pass branches inclined at 45^{o} to the main flow. In order to ensure sufficient by-pass flow an additional orifice resistance plate of 140 mm I.DIA. was mounted between the downstream flange of the flow divider and the upstream flange of the combustor.

3.2 THE CROSSFLOW ASSEMBLY

The crossflow assembly consists of a combustor, a settling chamber and a contractor element (Fig. 3.1(a)).

The experimental objectives were to achieve a crossflow of 450-600 K temperature and a relatively flat temperature profile. These requirements were fulfilled by a modified version of a primitive "pepper pot" combustor (Fig. 3.4), previously used by Vermeulen in research on the acoustic control of mixing processes (Ref. 8). The "pepper pot" combustor flame tube was mounted in the 203 mm I.DIA. pipe as shown in Fig. 3.4. The outlet of the flame tube was a specially designed mixing nozzle (Fig. 3.5), of star-shaped cross-section, with a 76 mm DIA. blocking plate attached by struts at about 50 mm from the end (Fig. 3.4 and 3.5).

This design increases the mixing between the hot combustor exhaust gases and the cold air flow by-passing the flame tube. The blocking plate was mounted in order to eliminate a central hot spot in the flow. The combustor operates on natural gas. The overall equivalence ratio for the combustor was estimated to be in the range of 0.05 for operation conditions of about 600 K flow temperature.

The main settling chamber was a rectangular duct of 610x310x920 mm size made out of stainless steel. In order to eliminate swirls and large-scale turbulence, three equally spaced 16 mesh screens were mounted in the chamber. The settling chamber was connected to the test section via a two-dimensional nozzle of contraction area ratio of 5.3 .

3.3 THE JET FLOW ASSEMBLY

The jet flow assembly (Fig. 3.1(a), 3.2(d) and (e)) consists of a throttle valve, an orifice meter, a settling chamber and a jet tube. The orifice meter was designed according to British Standards, B.S.1042; Part 1, with a throat to pipe ratio of 0.3818. The orifice meter pipe (50mm I.DIA.) was then connected through a diffuser to the settling chamber.

The settling chamber, similar to that of the main branch, was of size 457x305x156 mm with two built-in 16 mesh screens. The chamber was terminated by a nozzle of contraction ratio of 8.0. The diffuser outlet forms a rectangular slot (305x14 mm) with five outlets in order to serve the future purpose of multiple jet studies. However, because of the need to keep the flow field simple, in order to develop a basic understanding, only a single jet from the centre of the test section floor was investigated.

The jet tube is an "L" shaped 20 mm I.DIA. copper tube that ends in an orifice of 19.93 mm I.DIA. mounted into the floor of the test section. The jet orifice, shown in Fig. 3.1(c), has a lip with outside geometry corresponding to that of the dilution air holes of the combustor used by Vermeulen in Ref. 6 and 7. There are four pressure taps placed in the vertical part of the jet tube, about seven diameters from the jet orifice, serving the purpose of jet static pressure measurement. The acoustic excitation system is attached through a "T" connector placed at the mid point of the horizontal part of the jet tube. A thermocouple tap T_j is positioned at a distance of about 1.5 pipe diameters downstream from the "T" connector, also see Fig. 4.8.

3.4 THE ACOUSTIC EXCITATION SYSTEM

A JBL Sound, Inc. 200 W loudspeaker was used as the source of acoustic pulsation. The speaker was built into a conical ended container (Figs. 3.1(a), 3.2(d) and (e)). The conical end of the container directs the pulsations into a 20 mm I.DIA. copper tube joining the jet flow tube assembly at the "T" connector. The driving power was generated by a sinusoidal function generator and amplifier (Fig. 4.8).

3.5 THE TEST SECTION

The test section (Figs. 3.1(b) and 3.2(c) and (d)) is a straight duct of rectangular cross-section (889x343x114 mm). This unit is similar to Walker and Kors' (Ref. 38) design, except that the height of the test section is a duplication of the flame tube diameter of the typical combustion chamber used in previous experiments on the acoustically controlled mixing process (Ref. 6 and 7).

Parts of the bottom and top wall were removable covers made out of mild steel. Both covers contain holes for the jet orifices located at the mid-length of the test section. There are six rows of seventeen thermocouple access holes bored in the top cover, Fig. 3.1(b). The access holes are at distances X/D=-1.43, 1.43, 2.86, 5.72, 11.44, 14.30 from the jet orifice. Special easily removable plug sets were designed to close unused thermocouple holes. The spare jet holes were also closed by appropriate flush plugs. The top central plug was drilled through for the purpose of mounting a reference thermocouple. One of the top jet hole plugs was modified to serve as a mount for static tube (Fig. 4.6). The top cover served as a mounting base for the 17 shielded thermocouple gantry traversing mechanism (Fig. 3.2(c) and 3.6). The traversing system and gantry allow simultaneous projection of the seventeen thermocouples into a particular transverse plane of the test section.

Two windows made out of heat resistant glass were mounted in the side walls of the test section for the future purpose of Schlieren visualization of the flow pattern, Figs. 3.2(c) and (d).

3.6 THE EXHAUST SYSTEM

Safety requirements necessitated that an exhaust gas cooling system be designed (Figs. 3.2(d) and 3.7). The hot exhaust gases are cooled in a two stage system; a tube type water cooler followed by a water spray.

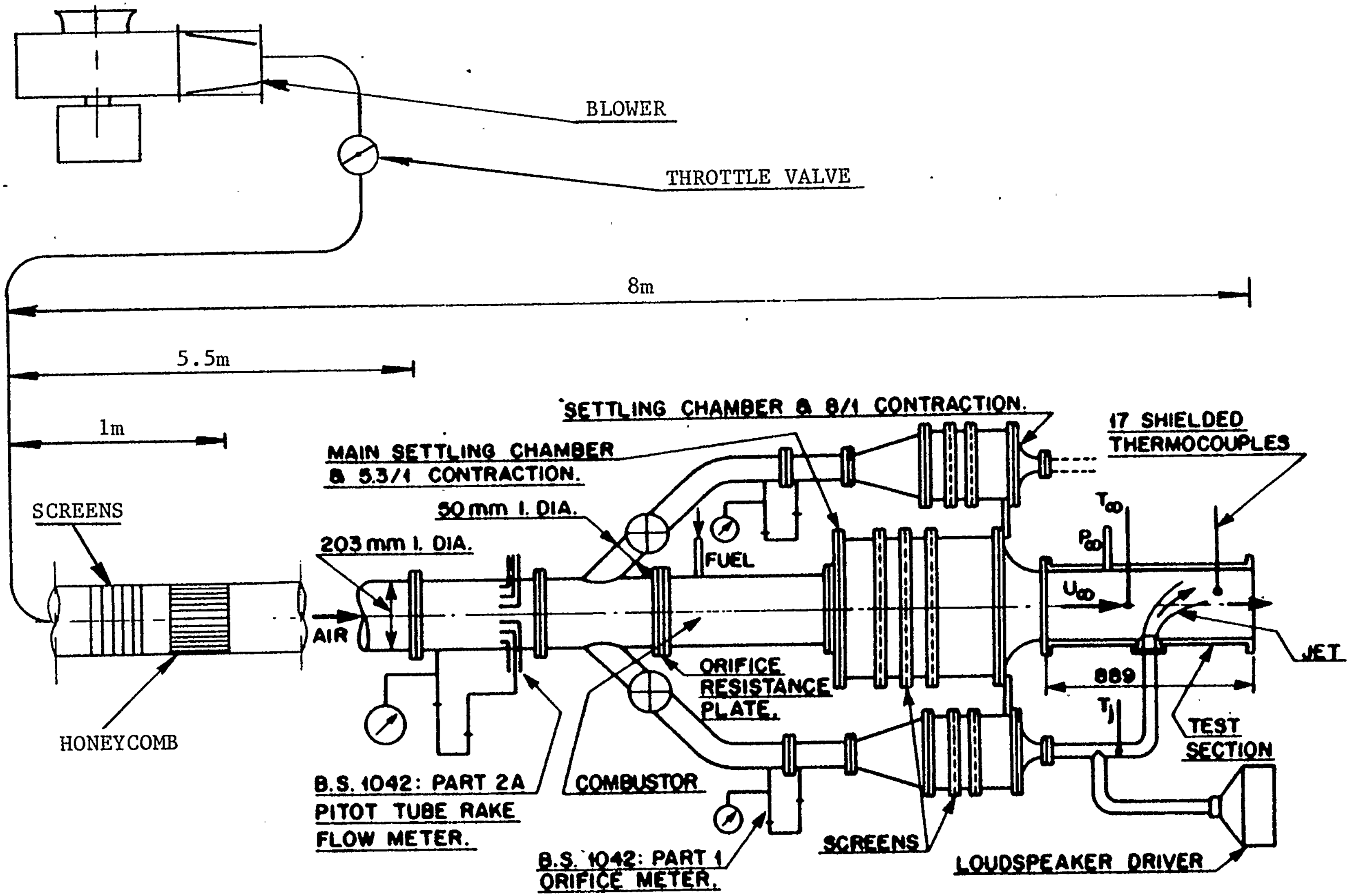

Fig. 3.1(a) Apparatus for Acoustically Pulsed Air Jets in Confined Hot Crossflow; - Layout.

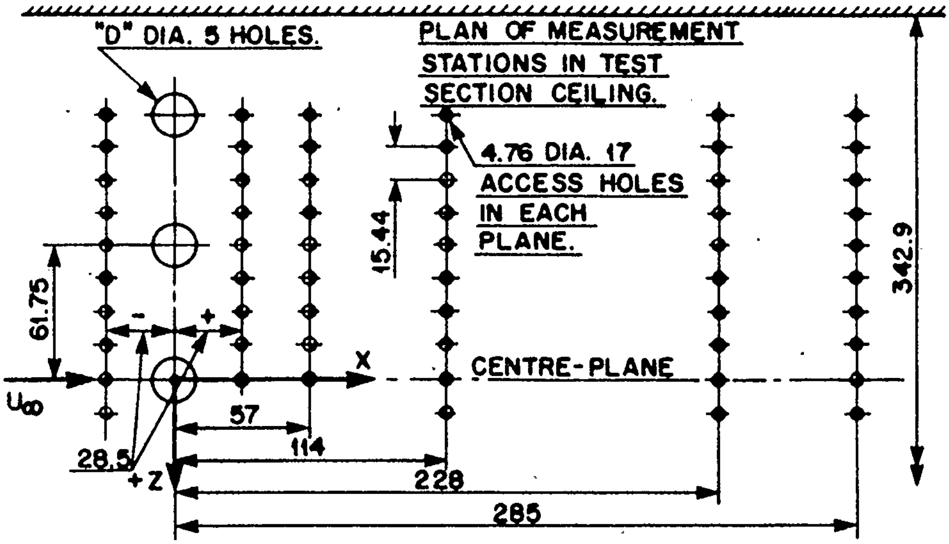

Dimensions in mm, Not to Scale

Fig. 3.1(b) Plan of Measurement Stations in Test Section Ceiling.

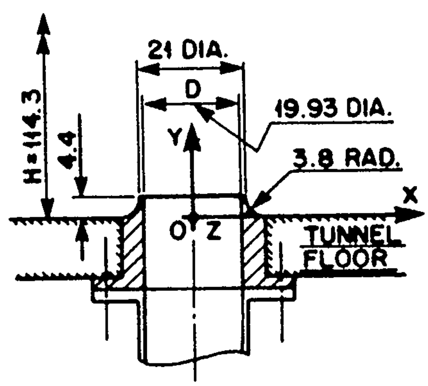

JET ORIFICE DETAILS.

DIMENSIONS IN mm.

NOT TO SCALE.

Fig. 3.1(c) Jet Orifice Geometry.

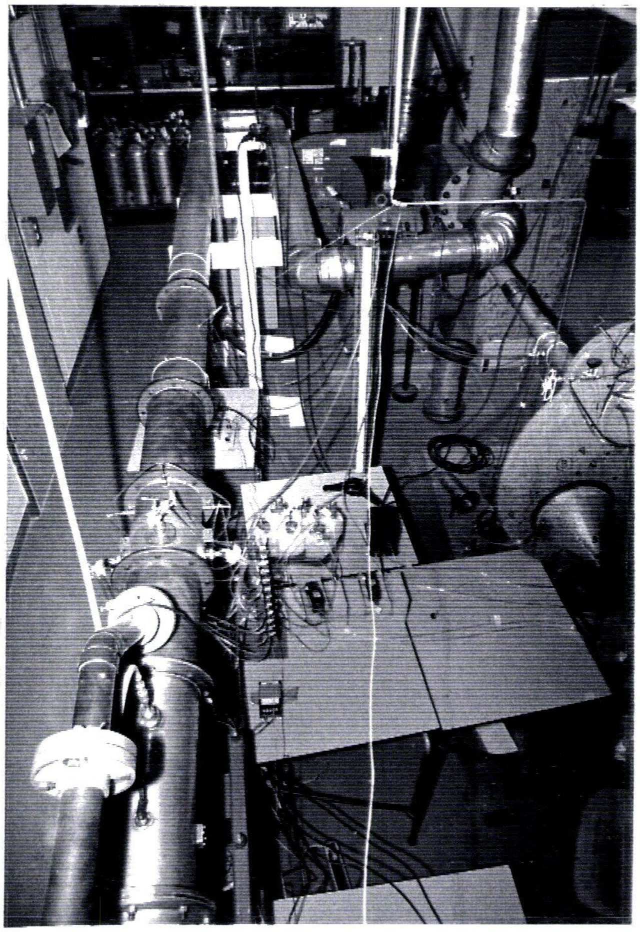

Fig. 3.2 (a)   Air Delivery Pipe System.

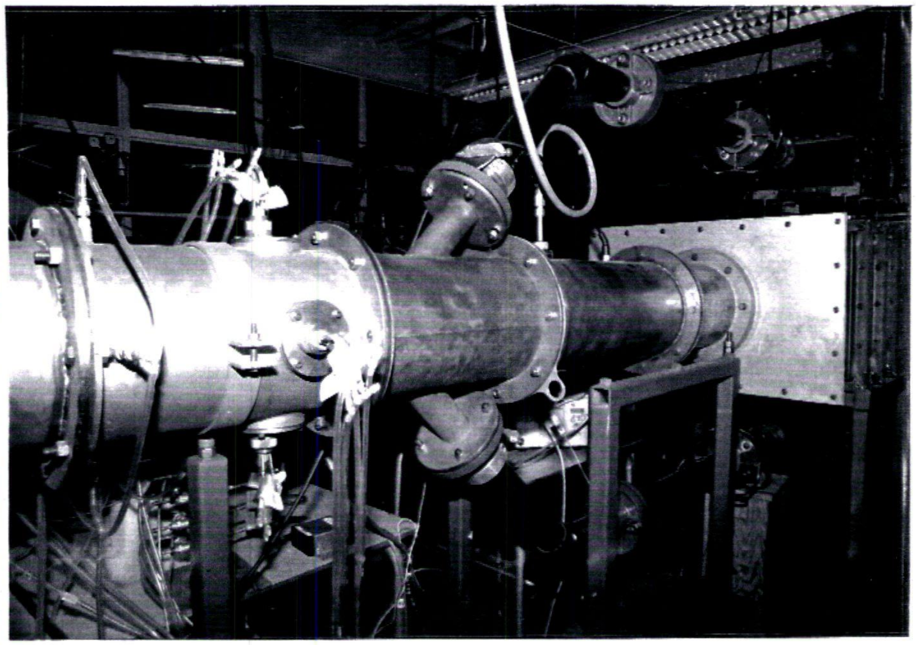

Fig. 3.2(b) View of Pitot-Tube Flow Meter, Flow Divider, Combustor and Settling Chamber.

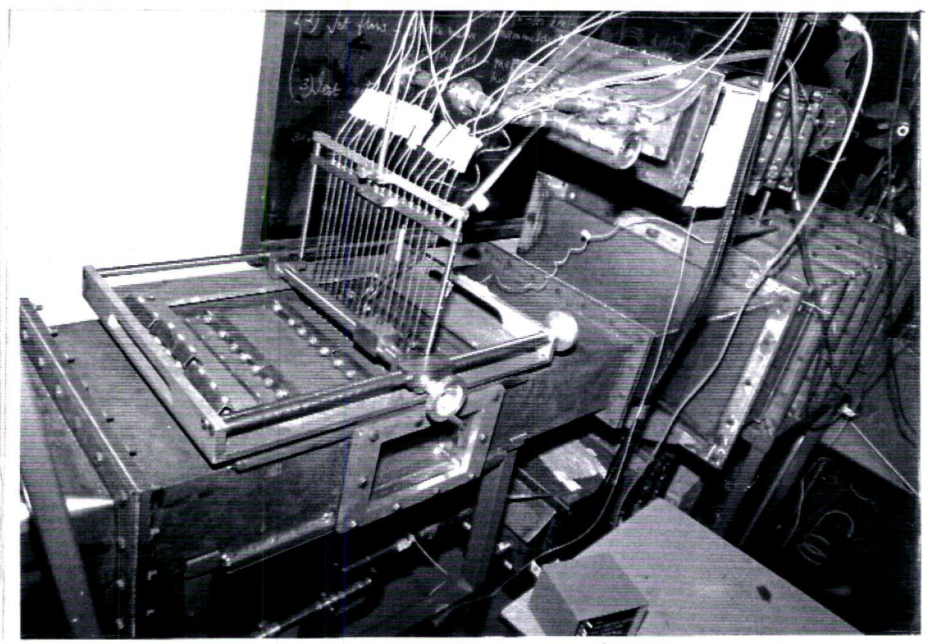

Fig. 3.2(c) The Test Section with Thermocouple Gantry Traversing System.

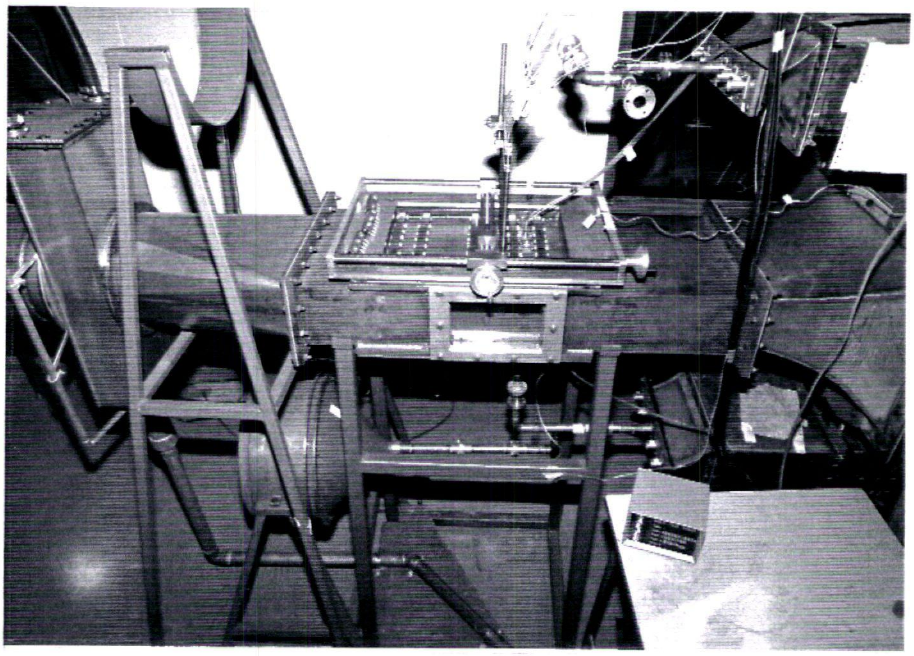

Fig. 3.2(d) The Cooling System, Test Section, Jet Flow Assembly (below) and Digital Switch Box (in foreground).

Fig. 3.2 (e) The Jet Flow Assembly.

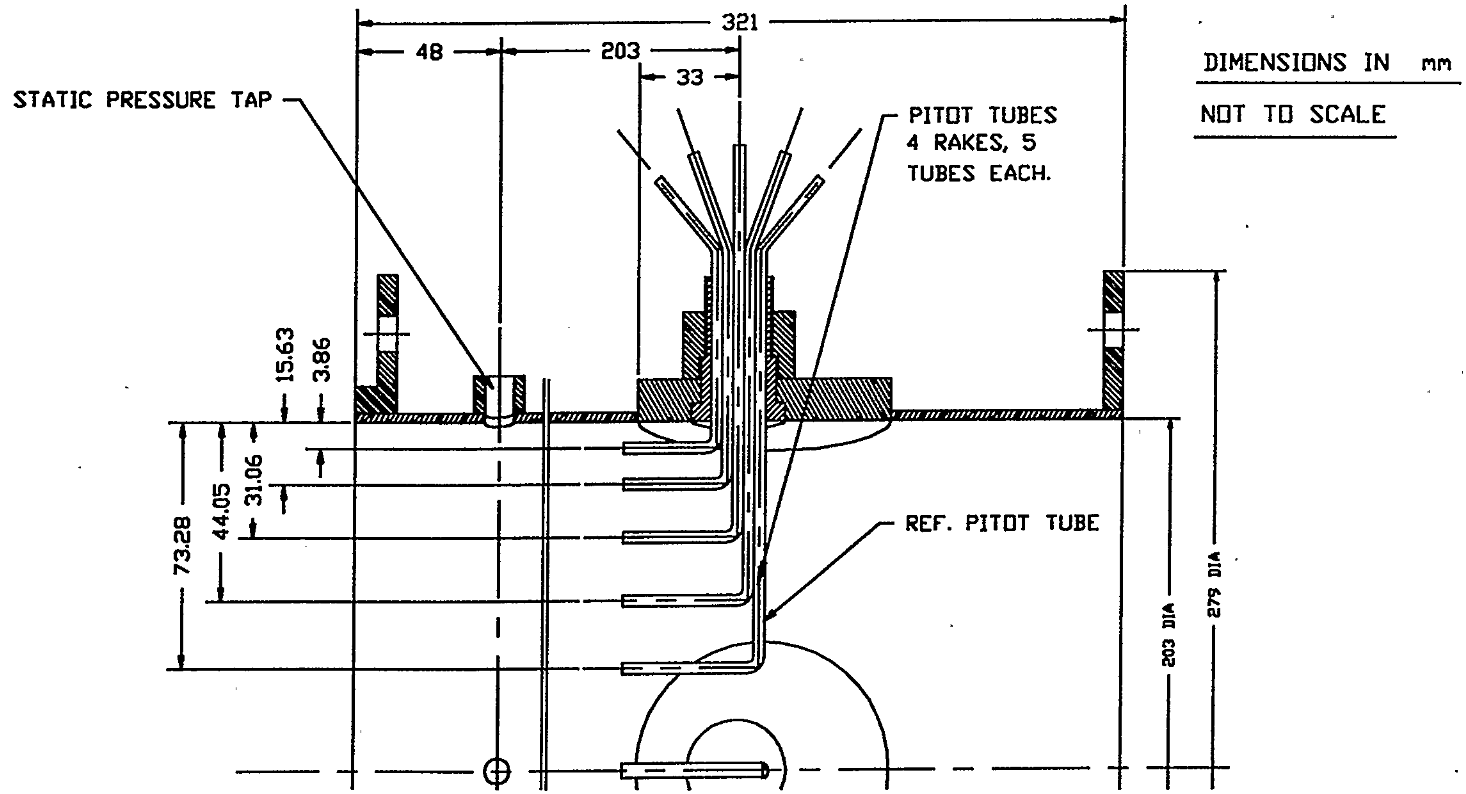

Fig. 3.3 The Pitot-Tube Flow Meter Design (Part Section).

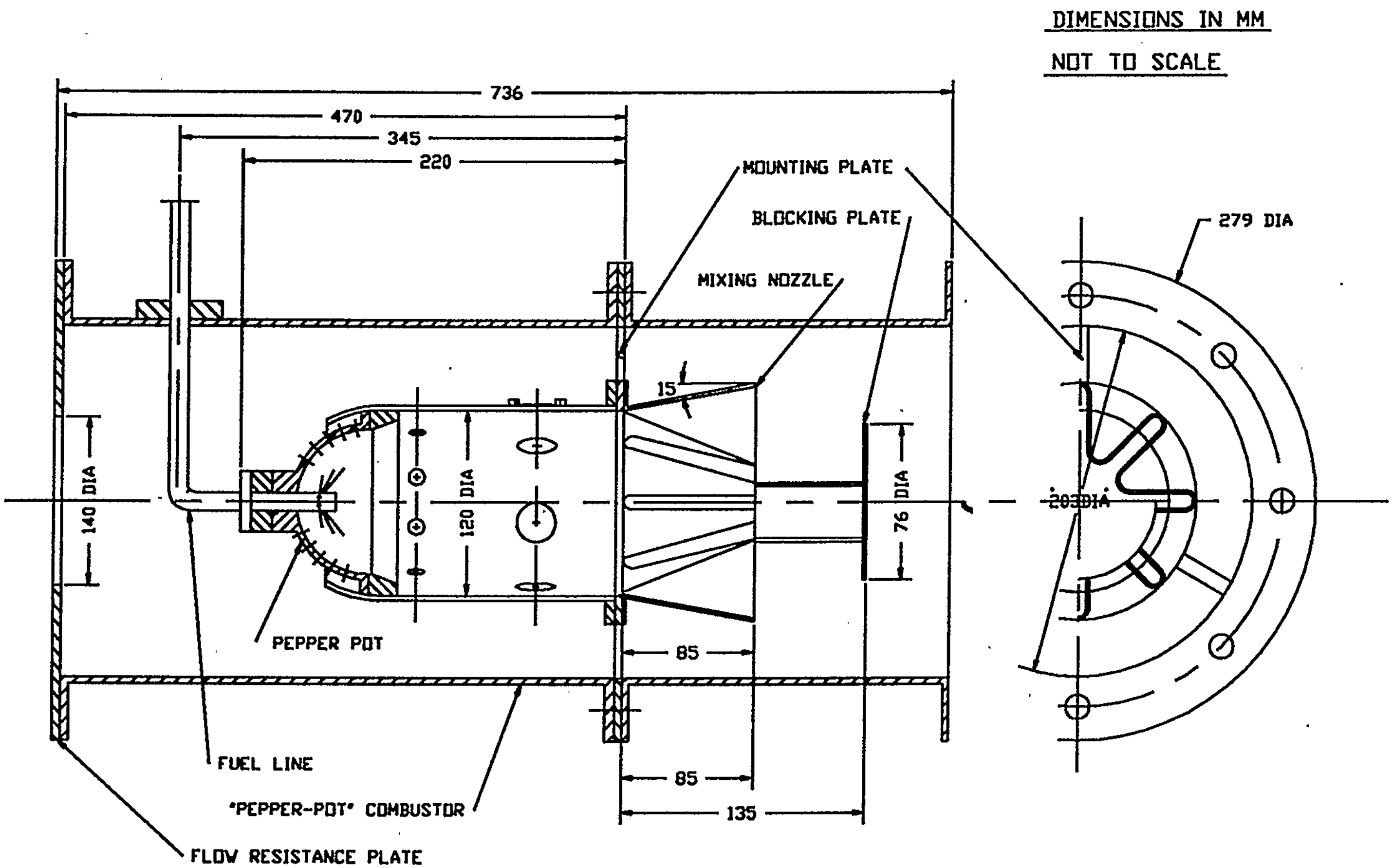

Fig. 3.4 "Pepper-Pot" Combustor Set-up.

Fig. 3.5 The "Pepper-Pot" Combustor Mixing Nozzle.

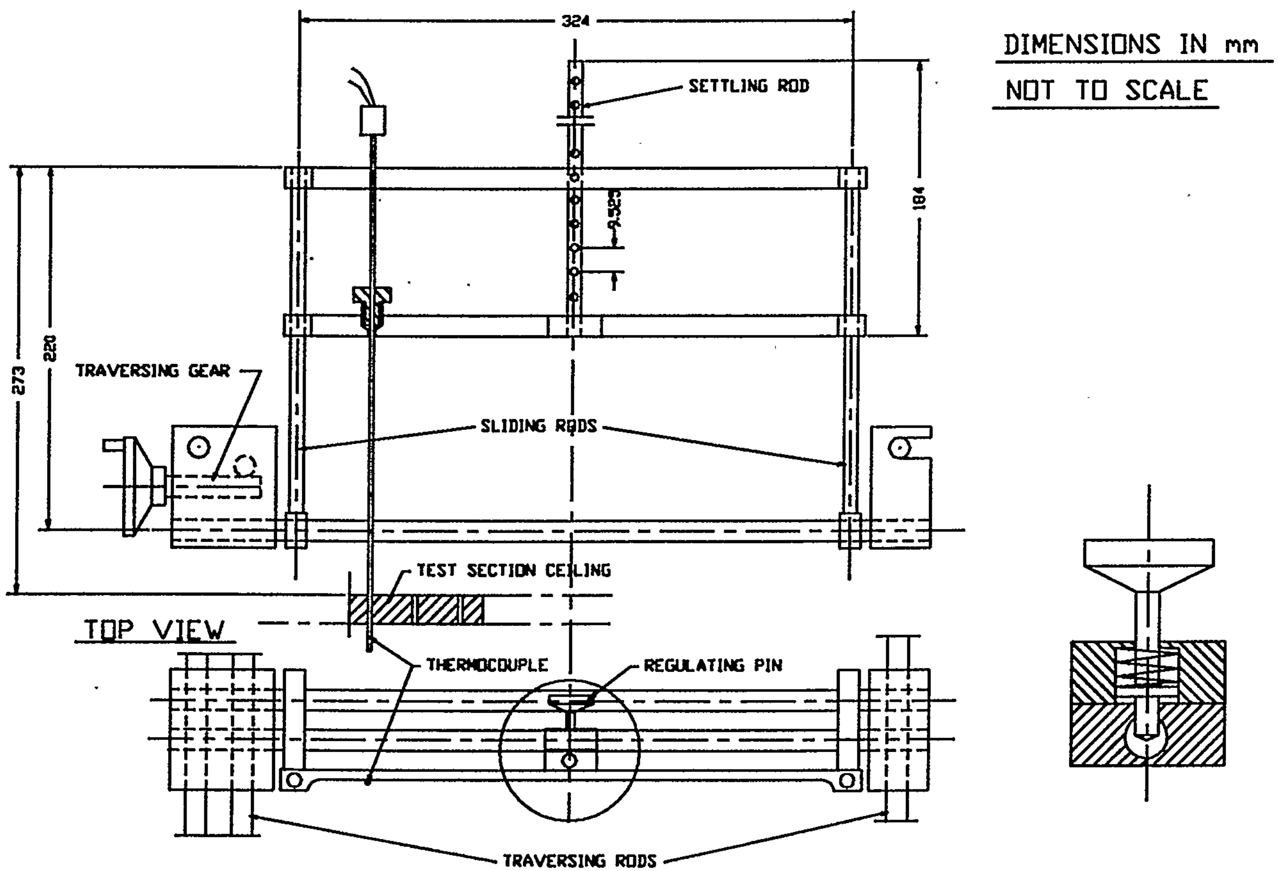

Fig. 3.6 The Thermocouple Gantry Traversing System.

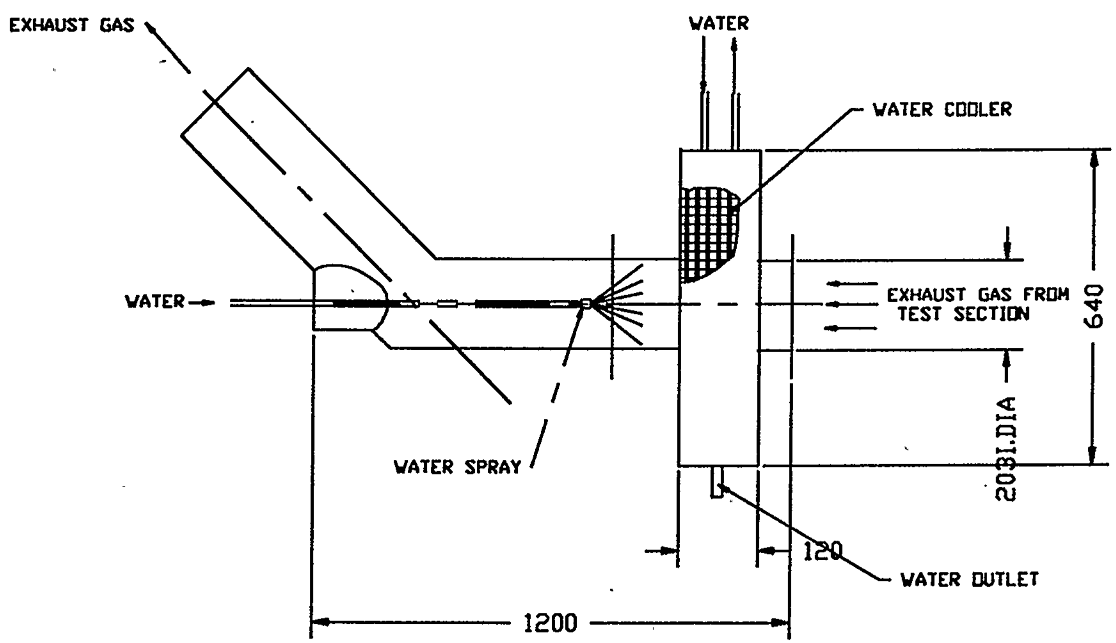

Fig. 3.7 The Cooling System.

CHAPTER 4

MEASUREMENT TECHNIQUES AND EQUIPMENT

The experimental measurements may be classified into three divisions, as follows;

(1) - flow quantity measurement,

(2) - acoustic excitation measurement,

(3) - measurement of the mixing process in the test section.

The complexity of the measurements and number of variables resulted in extensive use of a data acquisition system based on a MacBasic 350 microcomputer (Fig. 4.1). The overall characteristics of the data acquisition system are presented in an additional subchapter 4.4.

4.1 THE FLOW QUANTITY MEASUREMENTS

The required flow measurements consisted of crossflow and jet flow mass flow rate measurements.

The jet mass flow rate was measured directly by an orifice type meter built according to B.S.1042; Part 1. The orifice plate was made out of aluminum with a thickness of 3.18 mm. The flow meter was placed in 50mm I.DIA. pipe linking the flow divider section with the jet settling chamber. The calibration curve of the meter is shown in Fig. 4.2 and the linear representation is given by equation (4.1);

$$\dot{M}_j = 7.407\ 10^{-4} \sqrt{\rho_r\ \Delta p_r} \qquad \text{kg/s} \tag{4.1}$$

$$\rho_r = \frac{p_r}{R\ T_r} \qquad \text{kg/m}^3 \tag{4.2}$$

The properties of the jet flow entering the test section were established by temperature and static pressure measurement in the 20 mm I.DIA. jet pipe;

$$\rho_j = \frac{p_j}{R\ T_j} \qquad \text{kg/m}^3 \tag{4.3}$$

$$V_j = \frac{\dot{M}_j}{\rho_j\ A_j} \qquad \text{m/s} \tag{4.4}$$

The crossflow mass flow rate was measured indirectly, as the difference between the total mass flow measured by the Pitot-tube flow meter (Fig. 3.3) and the jet mass flow;

$$\dot{M}_\infty = \dot{M}_f - \dot{M}_j \tag{4.5}$$

The total mass flow measurements were conducted prior to the main research experiment by using the Pitot-tube flow meter at different settings of the main throttle valve. A schematic diagram of the measurement set-up is shown in Fig 4.3. Each of these measurements consisted of 20 differential pressures (between flow meter Pitot-tubes and static pressure taps) and the temperature of the flow. All differential pressures were measured by the same VALIDYNE P305D-20 differential type transducers (548 Pa range). A special 20-valve switch system was used for selection of the flow meter Pitot tubes. The pressure transducer was connected to the MacBasic computer through the ANALOG DEVICES AINO3 analogue card. The flow temperature was measured by a chromel-alumel type-K thermocouple connected to the computer by the ANALOG DEVICES AINO2 analogue card. Each recorded measurement (Pitot pressures and temperature)was an average of 25 values recorded in 0.425 sec time interval. The data recording was controlled by a remote system consisting of a digital box connected to the computer through the ANALOG DEVICES DINO2 digital card. The total mass flow was obtained by integration of the measured velocity profiles. A sample of the velocity profiles measured by the flow meter are shown in Figs. 4.4(a) and (b). These profiles are within British Standard requirements for this type of flow meter. Fig. 4.5 presents total mass flow versus the square root of product of density and differential pressure between the flow meter reference Pitot tube (Fig. 3.3) and the flow meter static pressure. The linear representation of this calibration is given by equation (4.6);

$$\dot{M}_f = 0.03657 \sqrt{\rho_f \; \Delta p_f} \qquad \text{kg/s} \tag{4.6}$$

where

$$\rho_f = \frac{p_f}{R \;\; T_f} \qquad \text{kg/m}^3 \tag{4.7}$$

The mass flow averaged crossflow velocity (main flow velocity in the test section) was defined by;

$$U_\infty = \frac{\dot{M}_\infty}{\rho_\infty \quad A_\infty} \qquad \text{m/s} \tag{4.8}$$

$$\rho_\infty \cong \frac{p_\infty}{R \quad T_{set}} \qquad \text{kg/m}^3 \tag{4.9}$$

The static probe (p_∞ measurement) was designed according to the N.P.L. Standards (Ref. 40, Fig. 4.6).

The setting reference flow temperature value T_{set} is a first approximation to $\overline{T}_\infty$ and was used to estimate ρ_∞ (Eq. 4.9) and then values of U_∞ (Eq. 4.8), U_∞/V_j and J, which were approximate test conditions.

4.2 THE ACOUSTIC EXCITATION MEASUREMENT

As discussed in Chapters 2.2 and 2.3 the acoustic excitation pulses the jet flow at the orifice exit, causing the jet flow to develop a wave motion growing into a train of toroidal vortices. Fig. 4.7 presents examples of the jet center-line velocity pulsation measured by a hot-wire anemometer (Ref. 5). This figure shows the previously discussed possibility of sink type flow related to the negative magnitude of the center-line jet velocity (Refs. 2, 3, 4, 5 and 33).

The power applied to the loudspeaker $\dot{W}$ was measured by an a.c. voltmeter and ammeter (Fig. 4.8), ignoring the power factor correction since previous work had shown it to be small (Ref. 1). In addition, an oscilloscope was used to check the shape of the amplifier output voltage to ensure that the amplifier was not saturating at high powers.

Provided the crossflow velocity is not too large the jet behaviour close to the orifice plane should essentially be that of a free jet, and therefore the result of dimension analysis from Refs. 1, 2 and 3 should apply, i.e.;

$$\left[\frac{V_e}{V_j}\right]^2 = F\left[\frac{\dot{W}}{\rho_j\, D^2\, V_j^3}\right] \tag{4.10}$$

or

$$\left[\frac{V_e}{V_j}\right] = F_1\left[\frac{\sqrt{\dot{W}}}{V_j\ \sqrt{\dot{M}_j}}\right] \tag{4.11}$$

Fig. 4.9 presents a set of curves showing the experimental results for the jet relative pulsation strength at different jet-to-crossflow velocities and for a frequency of 208 Hz. This data was collected by Chin Ref. 1 and 2. For the tests of this thesis carried out at an average value of J=3.17 an equivalent value of V_j/U_∞ was calculated from $\sqrt{J}$, i.e., V_j/U_∞=1.81, and the corresponding line at V_j/U_∞=1.81 was interpolated as shown on Fig. 4.9. This was then taken to be the calibration line for these tests and used to estimate required values of V_e/V_j, in effect establishing F of Eq. 4.10 to be the slope constant 0.045.

Despite the identical geometry of the jet flow assembly for the "cold" and "hot" flow studies, the frequency response of the system was measured as a check of Chin's results. The experimental set-up (Fig. 4.10) for this measurement was the same as that used by Chin (Ref. 1). The response (Fig. 4.11) was determined by means of dual channel FFT analysis at zero flow conditions. As shown good response of the system was found to be at 204 Hz, which is acceptably close to the 208 Hz obtained in the former work. The apparent better response at 996 Hz was not used since it was desired to test at Chin's conditions for comparative purposes, and at 204 Hz strong driving was obtained. The method for this response measurement was based on that of Crow and Champagne (Ref. 24).

4.3 ASSESSMENT OF THE MIXING PROCESS IN THE TEST SECTION

The nature of the mixing process was assessed by a detailed investigation of measured temperature profiles in various transverse planes of the test section. The measurement of the temperature profiles was performed simultaneously at each vertical location by seventeen thermocouples traversed through holes in the test section ceiling (Fig. 3.1(b)). The traversing mechanism and gantry (Fig. 3.6) positioned the thermocouples in a parallel array so that accurate, simultaneous vertical traverses could be made to determine the mean temperature profiles in particular transverse planes. The 17-thermocouple array was moved in 9.53 mm steps to give 12 different vertical positions, i.e., a total of 12x17=204 temperature measurements (Fig. 4.12). The thermocouples were shielded assemblies of standard design for measuring stagnation temperature, and had an O.DIA. of 3.26 mm (Fig. 4.13). The maximum total geometrical blockage due to the projection of thermocouples into the test section was 16% which was assumed to have no significant influence on the collected data.

4.4 MEASUREMENT TRANSDUCERS AND THE DATA ACQUISITION SYSTEM

Table A1 provides information about the pressure transducers used during the experiment. Most of these transducers were connected through an ANALOG DEVICES AINO3 analogue card to the computer (Fig. 4.14). The lack of adequate transducers with electrical ports (due to cost) prevented the development of a fully automatic system for "data input". This problem was accommodated by manually inputting some pressure readings through the computer keyboard. These pressures were measured by NATIONAL LX 1801 AX absolute type pressure transducers built into a box with a channel type selection system. The following pressures were recorded in this manner:

p_a - atmospheric pressure, Channel 3 (calibration Fig. A1),

p_f - Pitot-tube flow meter static pressure, Ch. 7 (calibration Fig.A2),

p_∞ - test section static pressure, Ch. 4 (calibration Fig. A3).

From the perspective of the estimation of flow properties the measurement of the differential pressure for the Pitot tube reference flow meter Δp_f, and orifice meter Δp_r, were of the highest importance. Both of them were measured by sensitive VALIDYNE P305D-20 differential type transducers (548 Pa range; calibration Fig.A4 and A5). The jet orifice meter static pressure p_r and the jet static pressure p_j were measured by differential transducers VALIDYNE P305D-30 and D-26 (calibration Figs. A6 and A7) respectively. All of these transducers were connected to the computer through the ANALOG DEVICES AINO3 analogue card.

The low velocity magnitude of the flow presented a problem with respect to the accuracy of the pressure measurements. For this reason, low velocity magnitude calibrations (10% of F.S.D.) of the transducers were very carefully performed with the aid of a precise oil (0.82 specific gravity) micromanometer of 1.5" oil range. Each calibration point consisted of 25 computer averaged readings. The hysteresis was also checked. Overall as can be seen from the data all calibrations were linear and highly repeatable. The calibrations showed practically zero hysteresis for all transducers used.

Fluctuation in the differential pressure readings in the flow meter section due to flow turbulence were damped by volumetric dampers (about 1.0 liter) connected to each pressure tap. The precision of the readings was further upgraded by averaging over 25 values recorded by the computer in a 0.425 sec time interval.

Chromel-alumel type-K thermocouples were used for the temperature measurements. Each thermocouple was checked against a precise mercury thermometer and showed agreement within the manufacturer's specification of ±0.55% accuracy. The thermocouples were connected to the computer through interfaces and the ANALOG DEVICES AINO2 analogue card (Fig. 4.14). Each recorded temperature was an average of 25 measurements recorded in a 0.425 sec time interval.

The data acquisition system (Fig. 4.15) had to serve two main purposes, i.e.;

- data collection,
- data monitoring.

The experimental recording time was considerable, therefore ensuring consistency of experimental conditions was of great importance. Such a requirements could only be solved by computer monitoring of the measured flow properties. A software package specially developed for the experiment allowed instantaneous data collection, its mathematical analysis and display in the form of various experimental parameters. The monitoring system employed a computer screen as a multiple purpose read-out, simultaneously displaying the flow parameters. This option allowed the setting of the experimental flow conditions to good accuracy. The main experimental parameters were momentum flux ratio J, reference test section temperature T_{set}, crossflow and jet velocity magnitudes.

The collection of temperature measurements in the test section was performed according to the positioning of the 17-thermocouple gantry. Each measurement was indexed to one of six transverse sections and to one of twelve vertical positions. The software provided an adequate numeration system for data organization. The transverse section set of measurements was finalized by monitoring (and recording) of the overall flow parameters. Each temperature measurement was automatically delayed by the required settling time of 15 sec. An additional software mode for temperature monitoring allowed free settling time adjustment with the help of a "built-in" settling time adjusted.

A special remote control system was adopted to operate the computer. This system allowed centralization of the work station by the test section and simplified the measuring procedure. The remote system consisted of a 5-switch digital box connected to the computer through the ANALOG DEVICES DINO2 digital card.

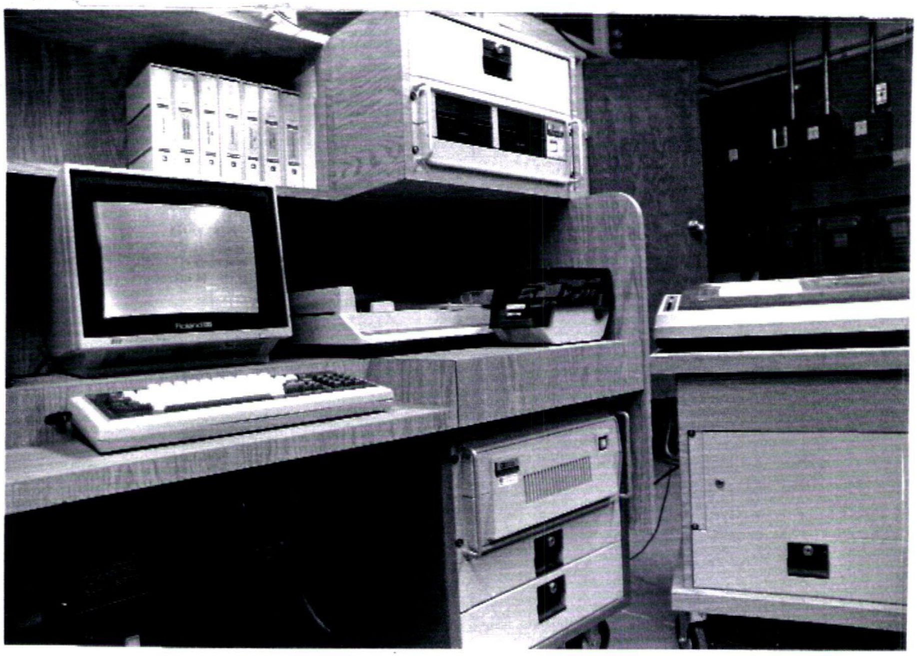

Fig. 4.1 The MacBasic 350 Computer.

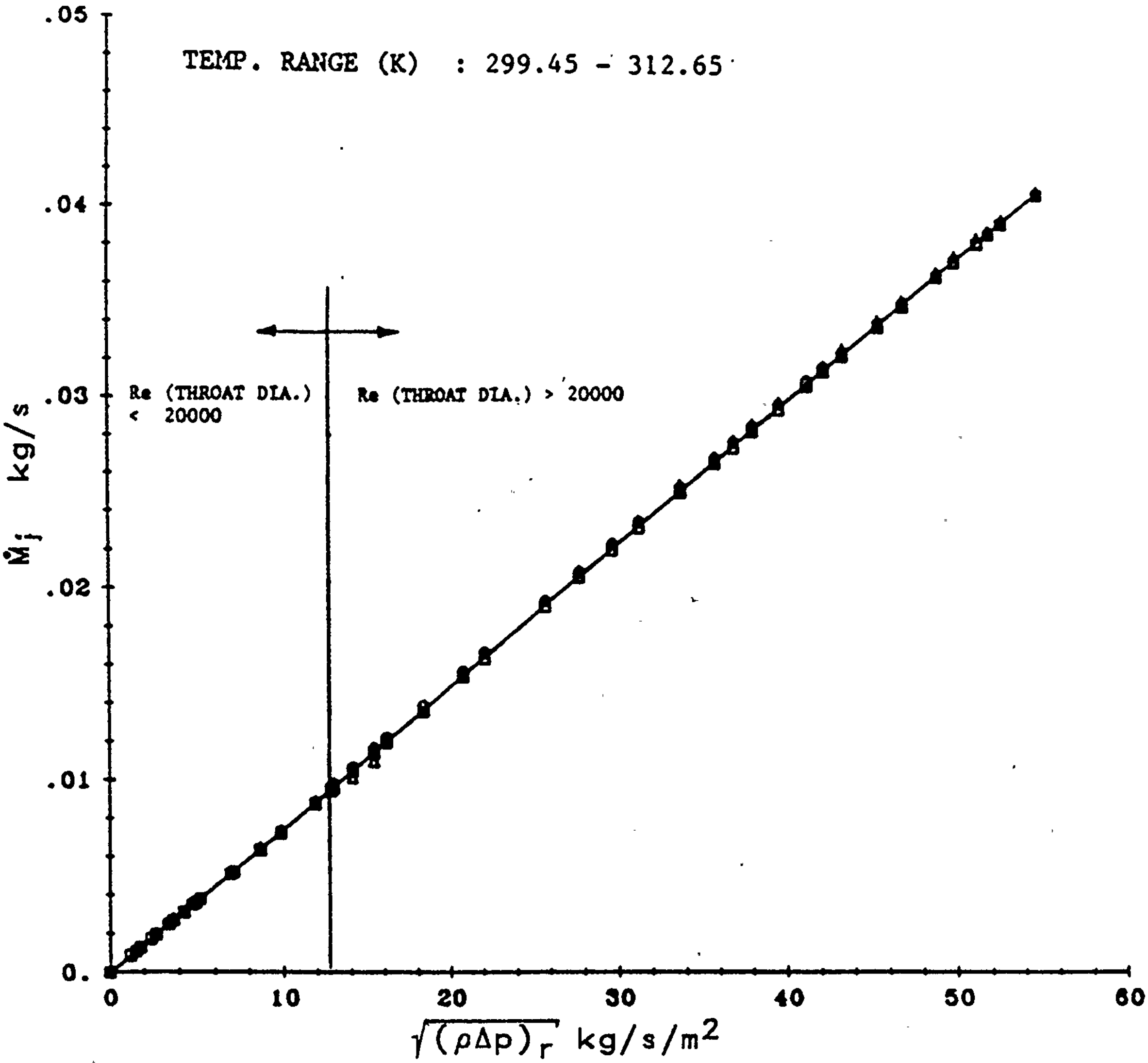

Fig. 4.2 The Jet Orifice Meter Calibration (from Ref. 1).

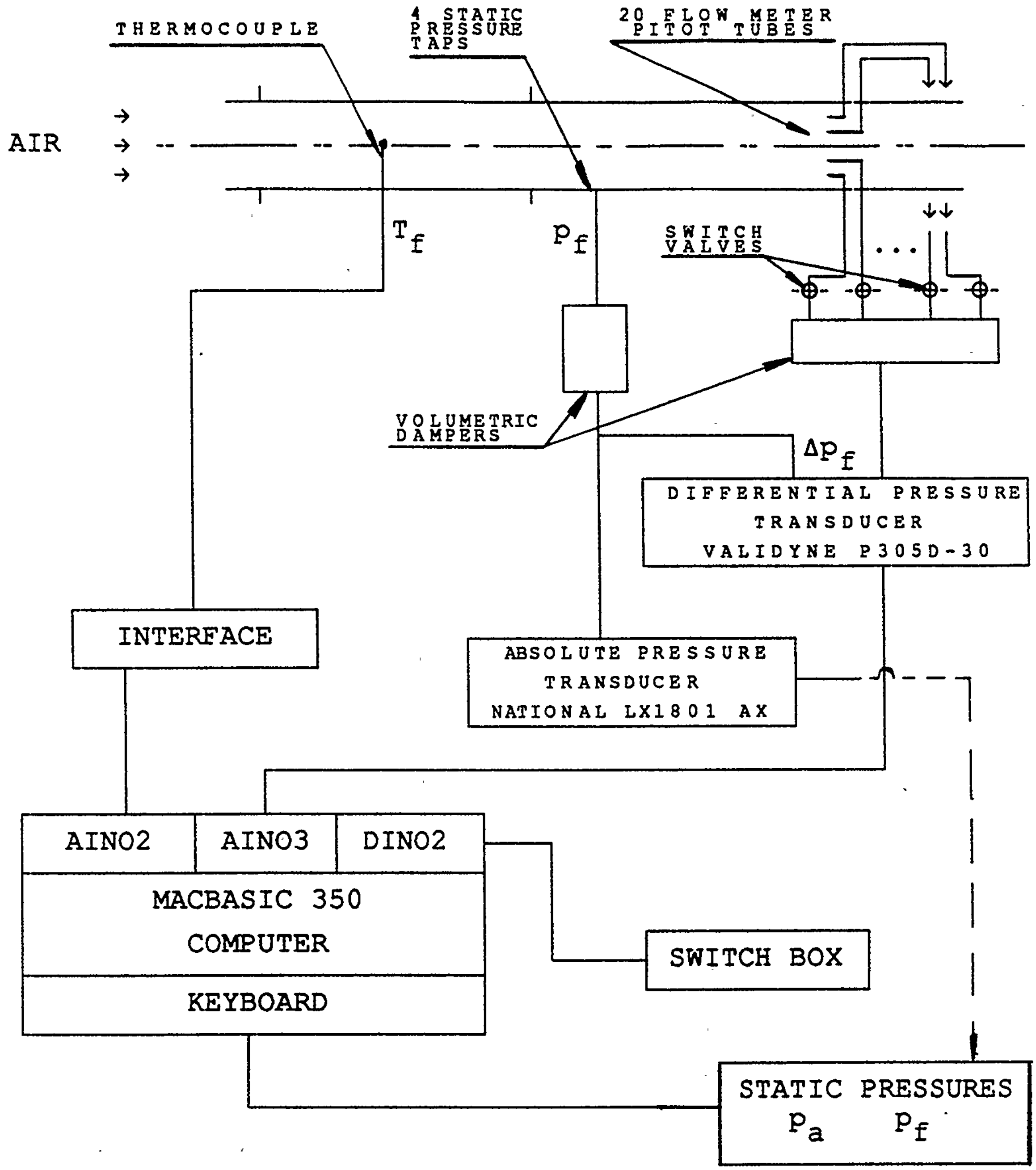

Fig. 4.3 Schematic Diagram of the Pitot-Tube Flow Meter Operational Set-up.

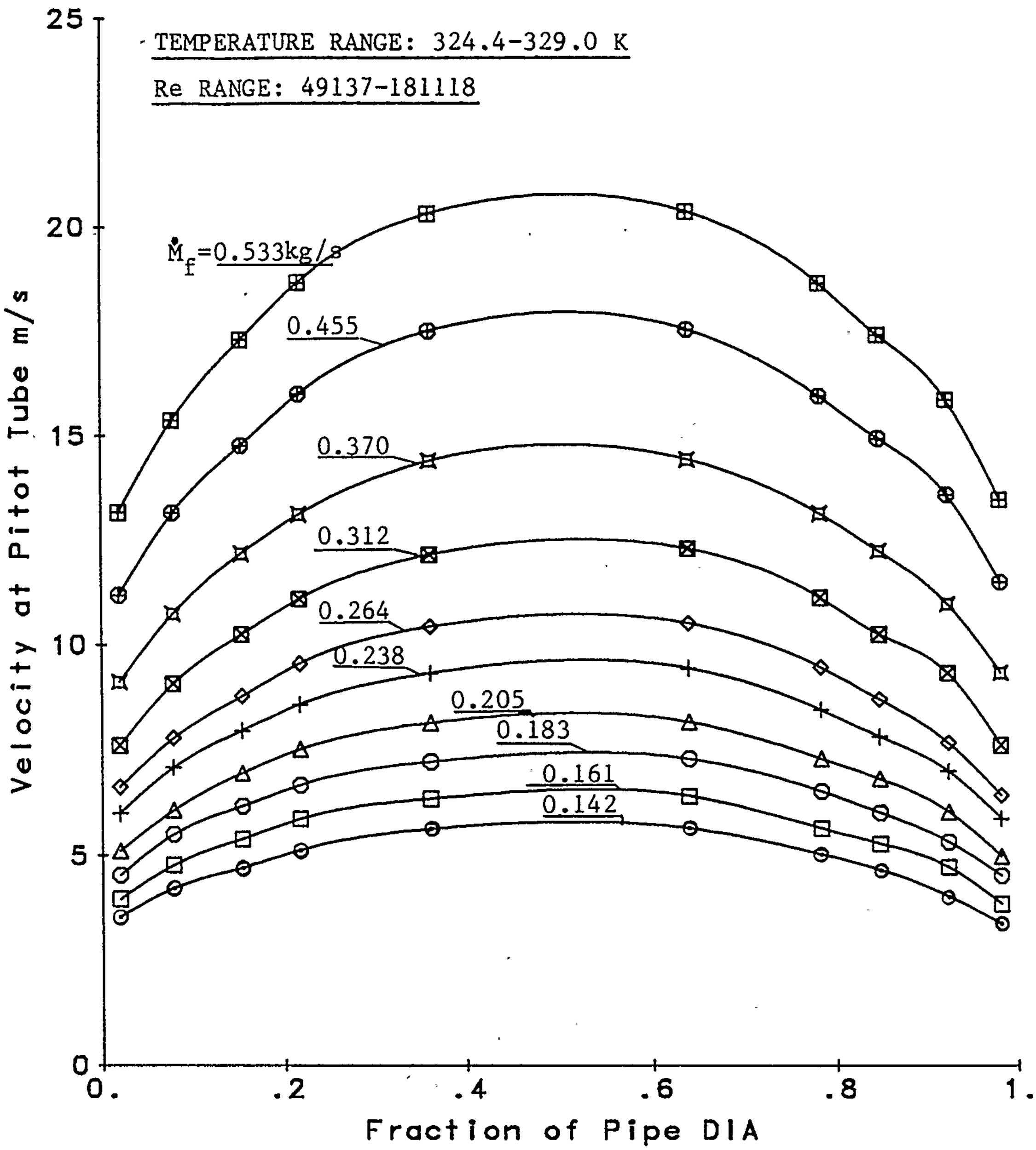

Fig. 4.4(a) Velocity Profiles in the Vertical Plane of the Pitot-Tube Flow Meter.

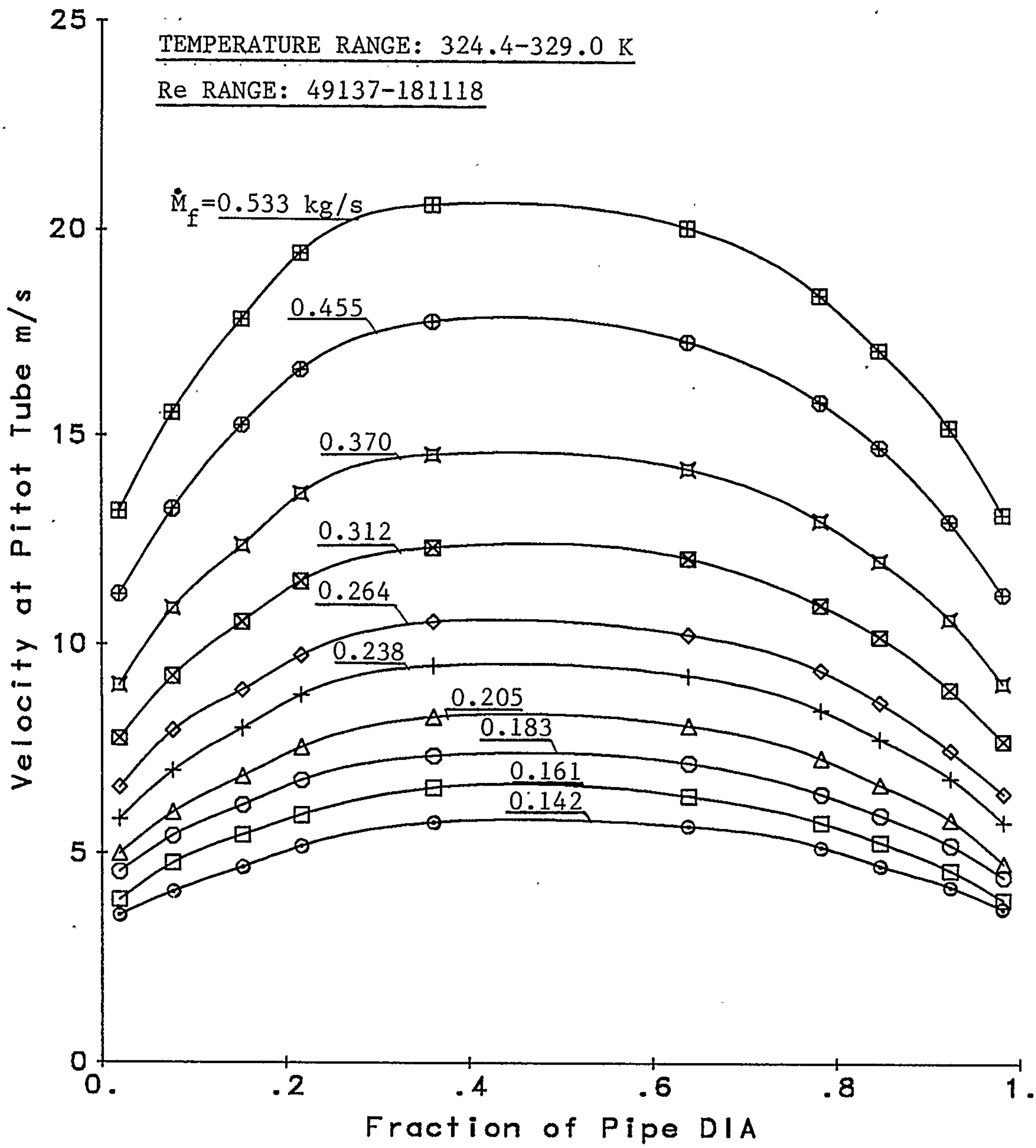

Fig. 4.4(b) Velocity Profiles in the Horizontal Plane of the Pitot-Tube Flow Meter.

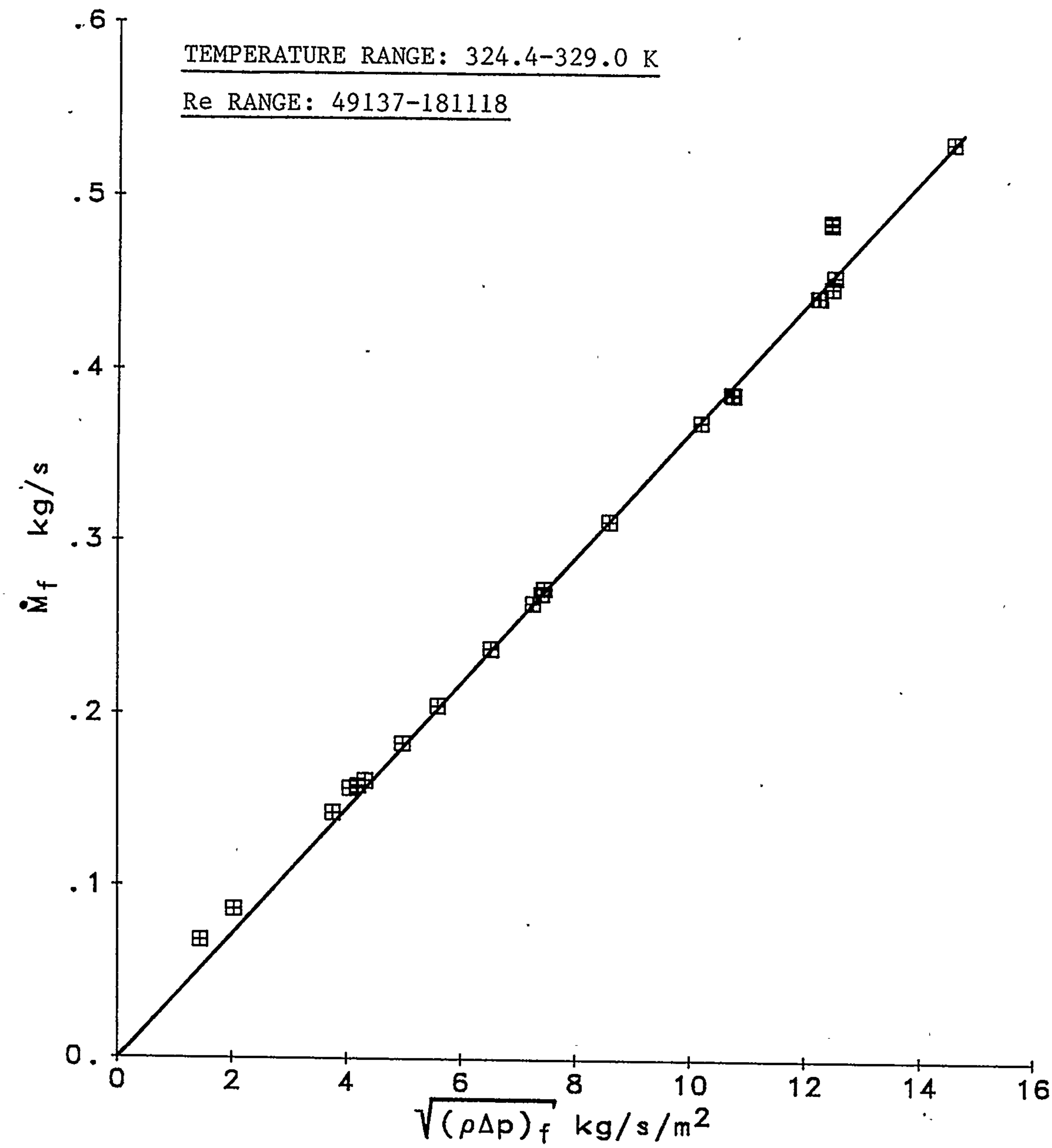

Fig. 4.5 Pitot-Tube Flow Meter Total Mass Flow Rate Versus Specific Mass Flow Rate Function at the Reference Pitot Tube.

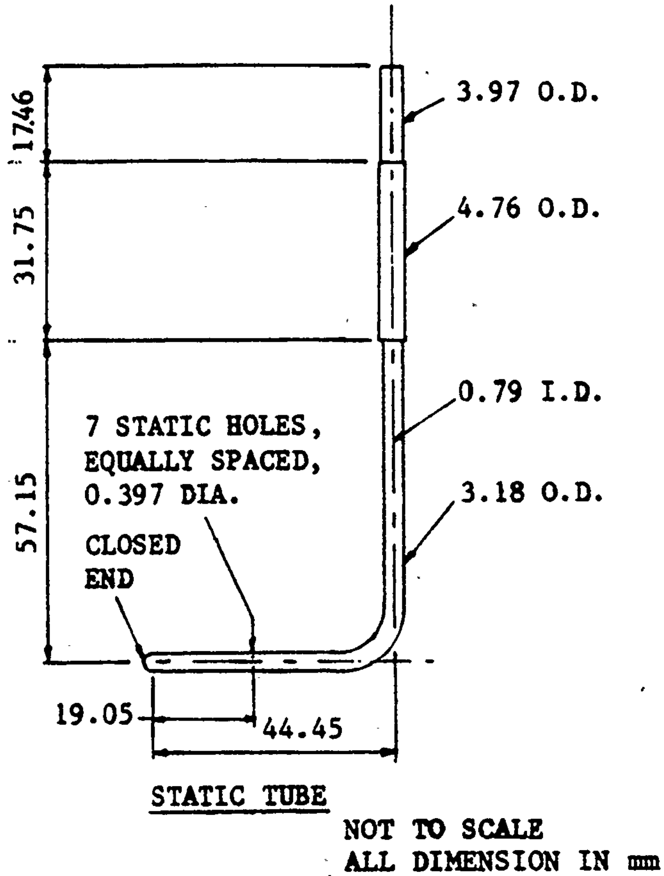

Fig. 4.6 Static Pressure Tube Used for Measurement of the Static Pressure in the Test section (from Ref. 1).

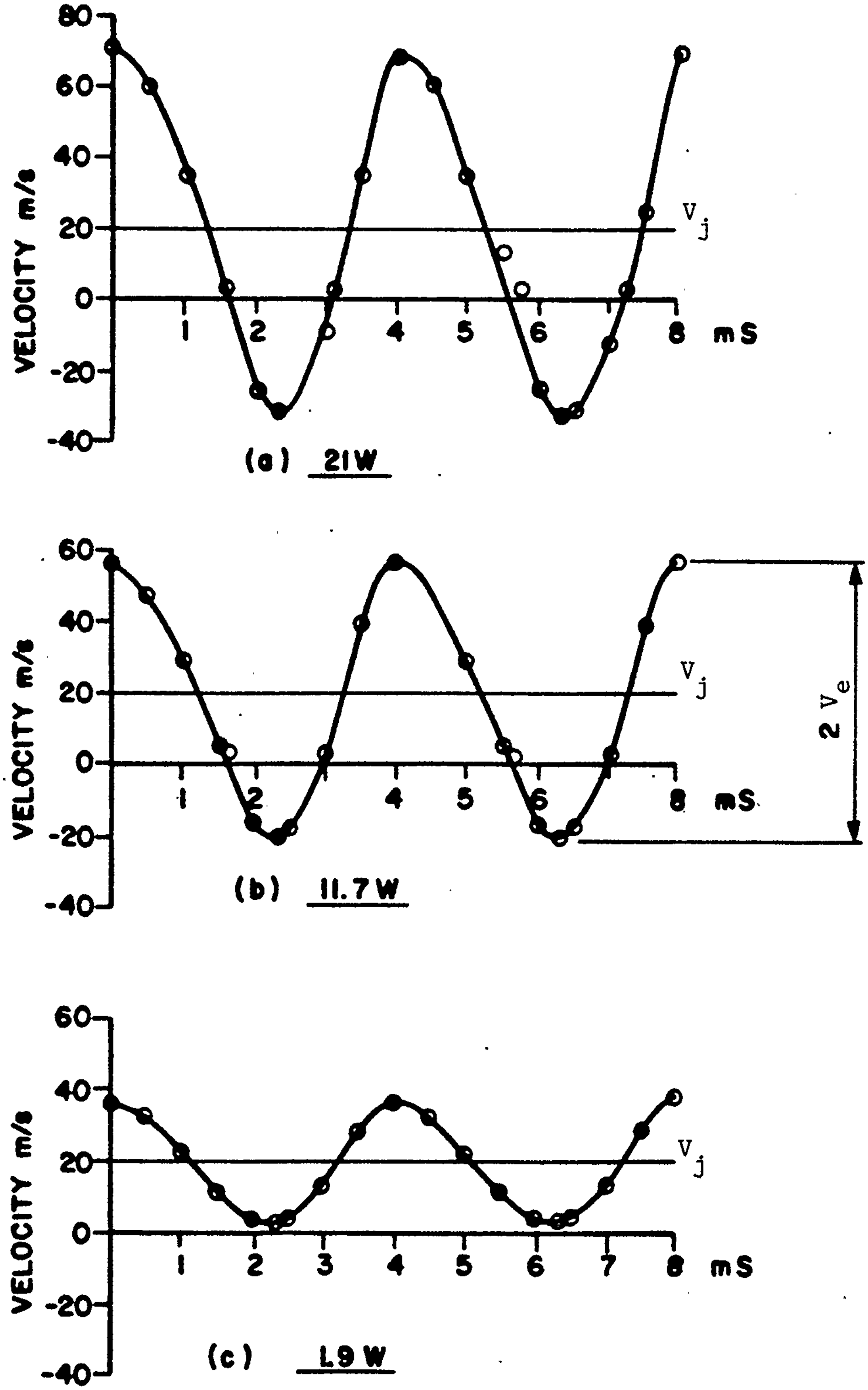

Fig. 4.7 Typical Velocity Wave Forms on the Centre-Line in the Nozzle Exit Plane, V_j=19m/s, 250Hz, 9.53mm Dia. Nozzle (from Ref.3).

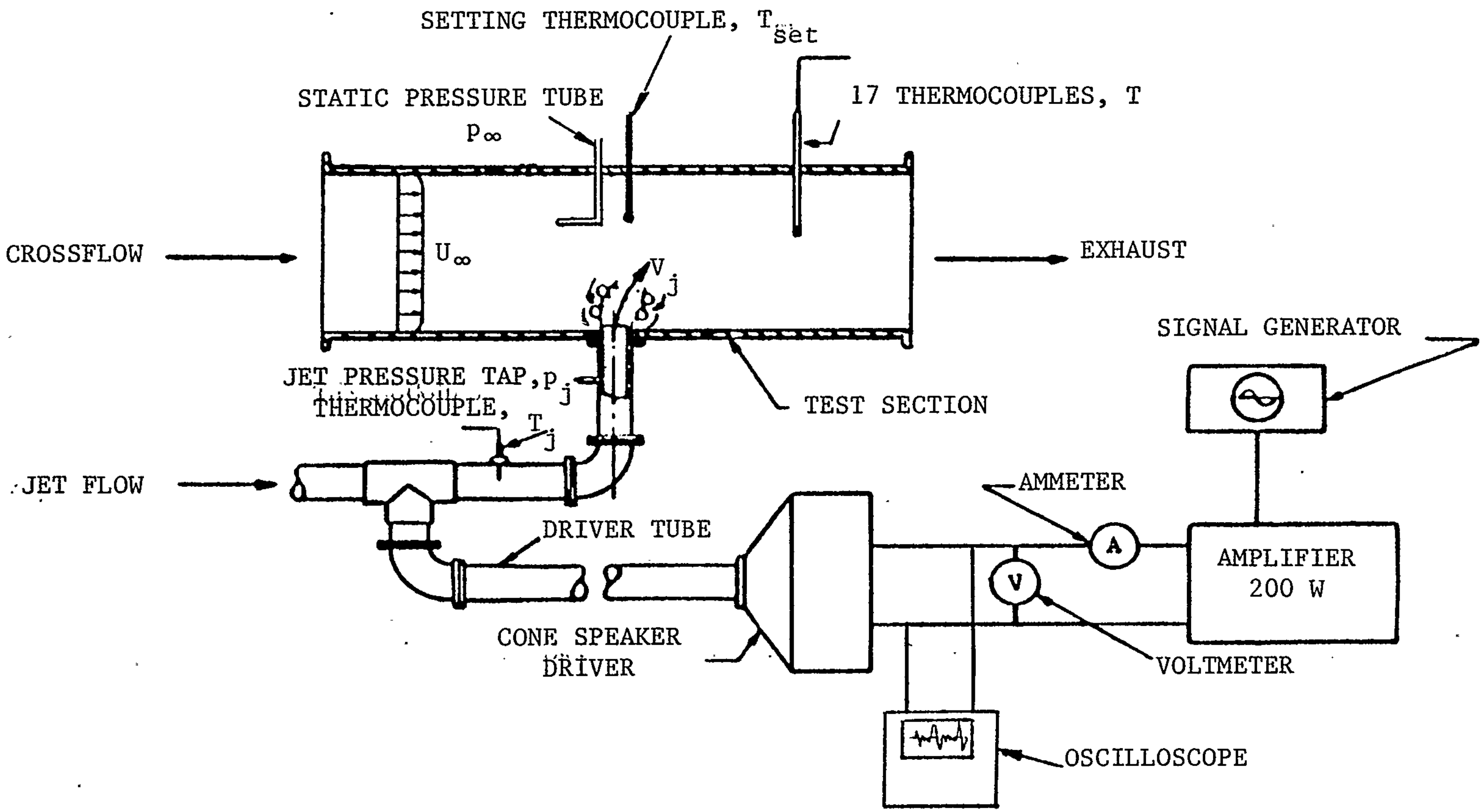

Fig. 4.8 Schema of Test Section and Jet Flow Assembly, Acoustic Excitation System and Associated Instrumentation (Modification of "Cold-Flow" Study Set-up; from Ref. 1).

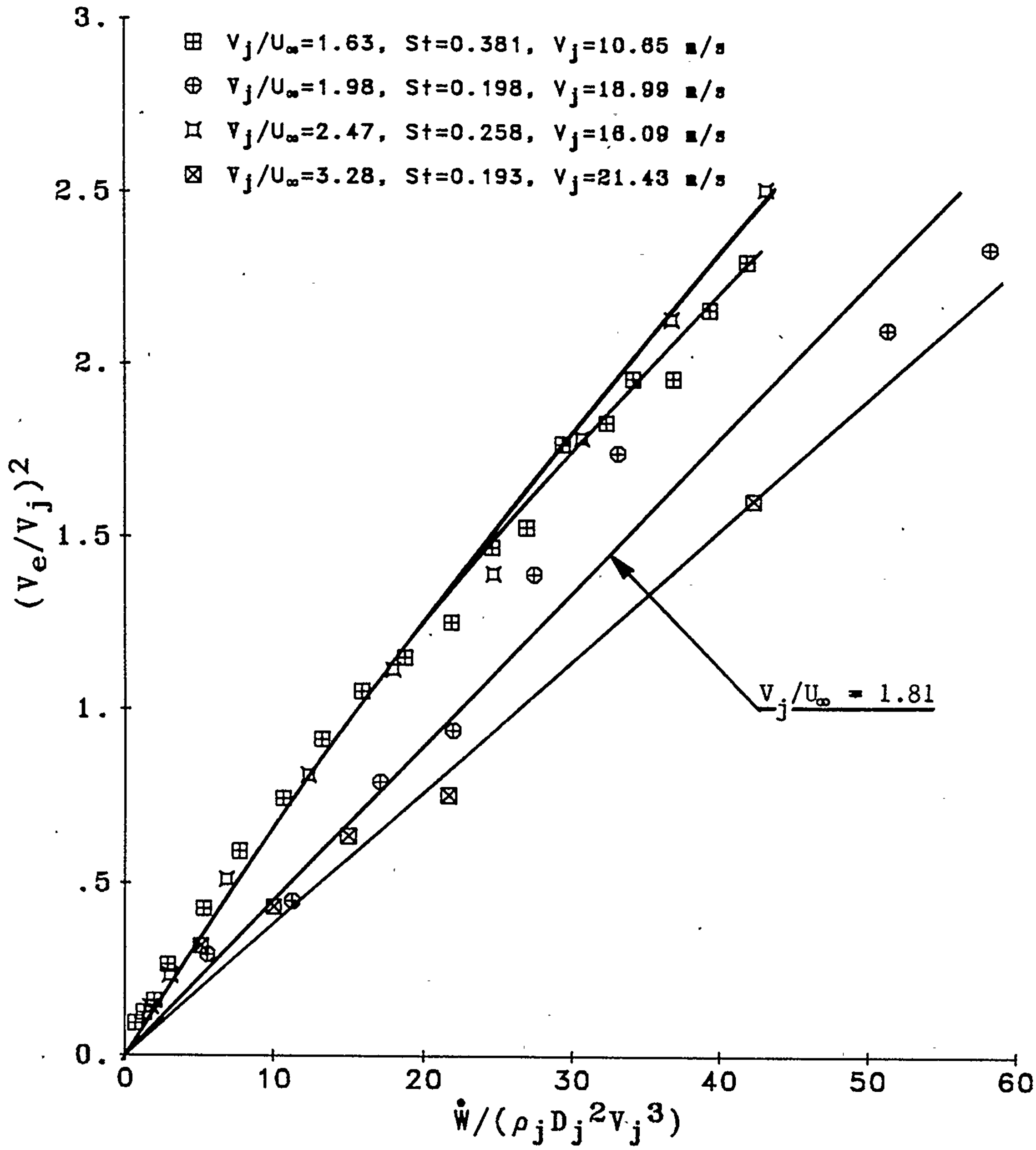

Fig. 4.9 The Relative Pulsation Strength Vs. Dimensionless Power Number, 19.93mm Dia. Θrifice, 208Hz (data from Chin, Refs. 1 and 2).

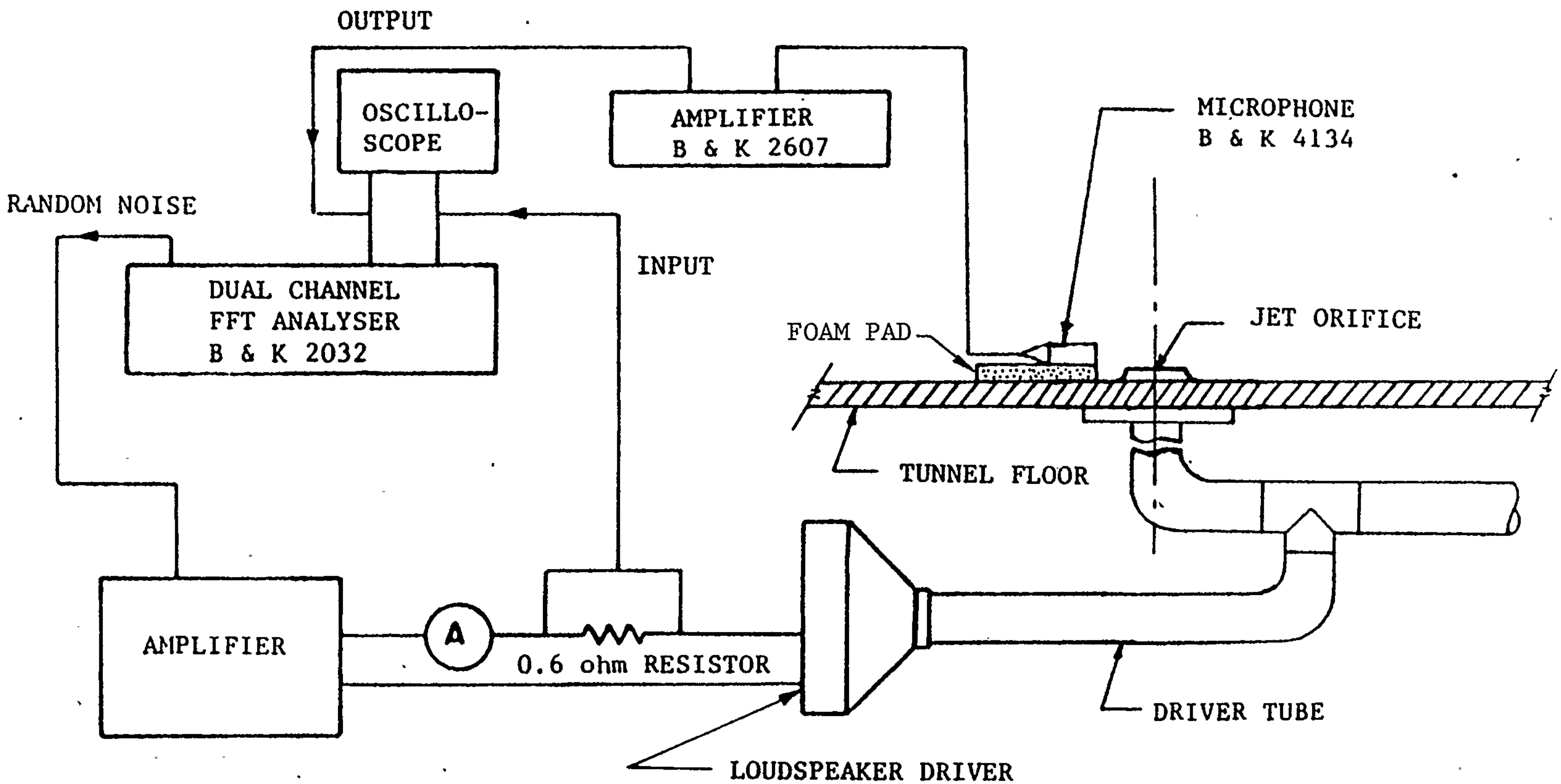

Fig. 4.10 Instrumentation Set-up for Frequency Response Measurement of the Driver Tube/Jet Tube--Loudspeaker Driver System (from Ref. 1).

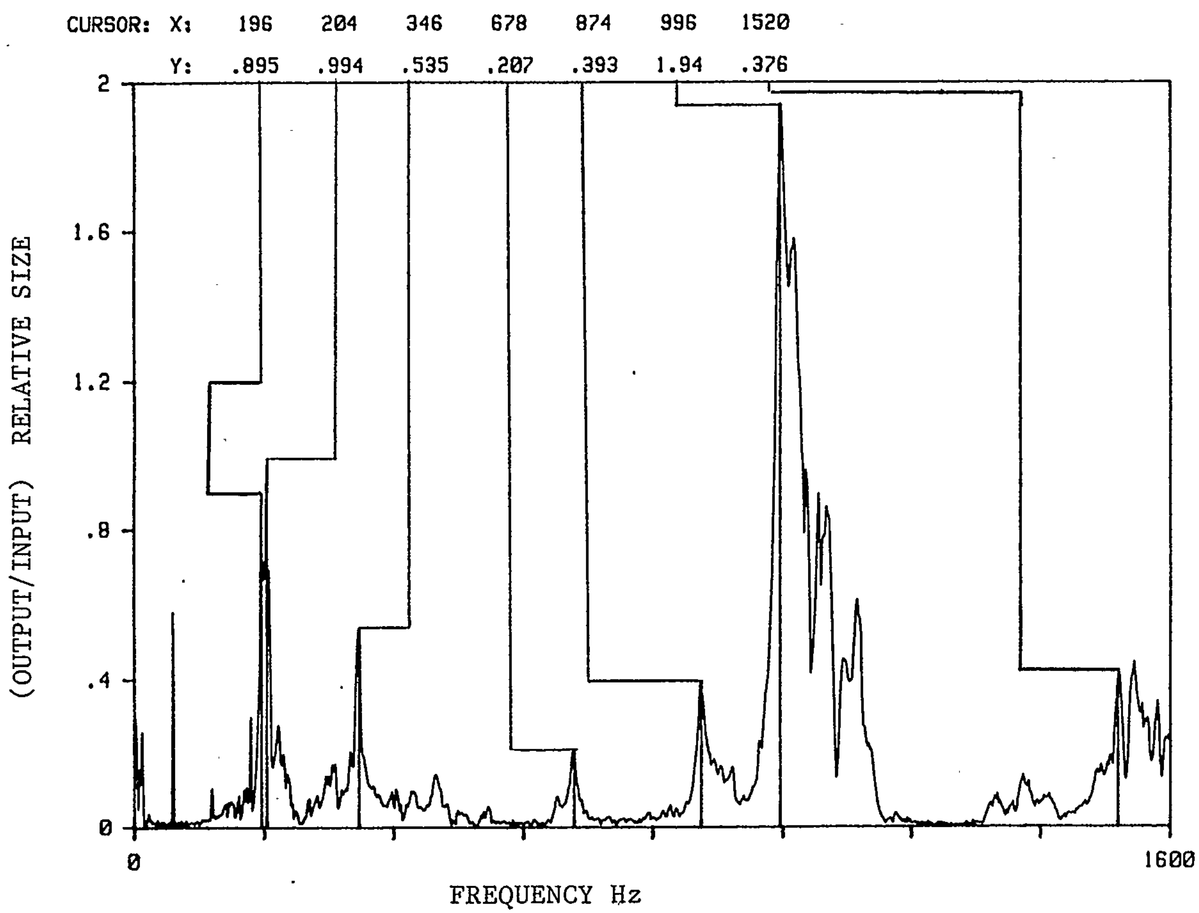

Fig. 4.11 Frequency Response of Drive Tube/Jet Tube-Loudspeaker Driver System.

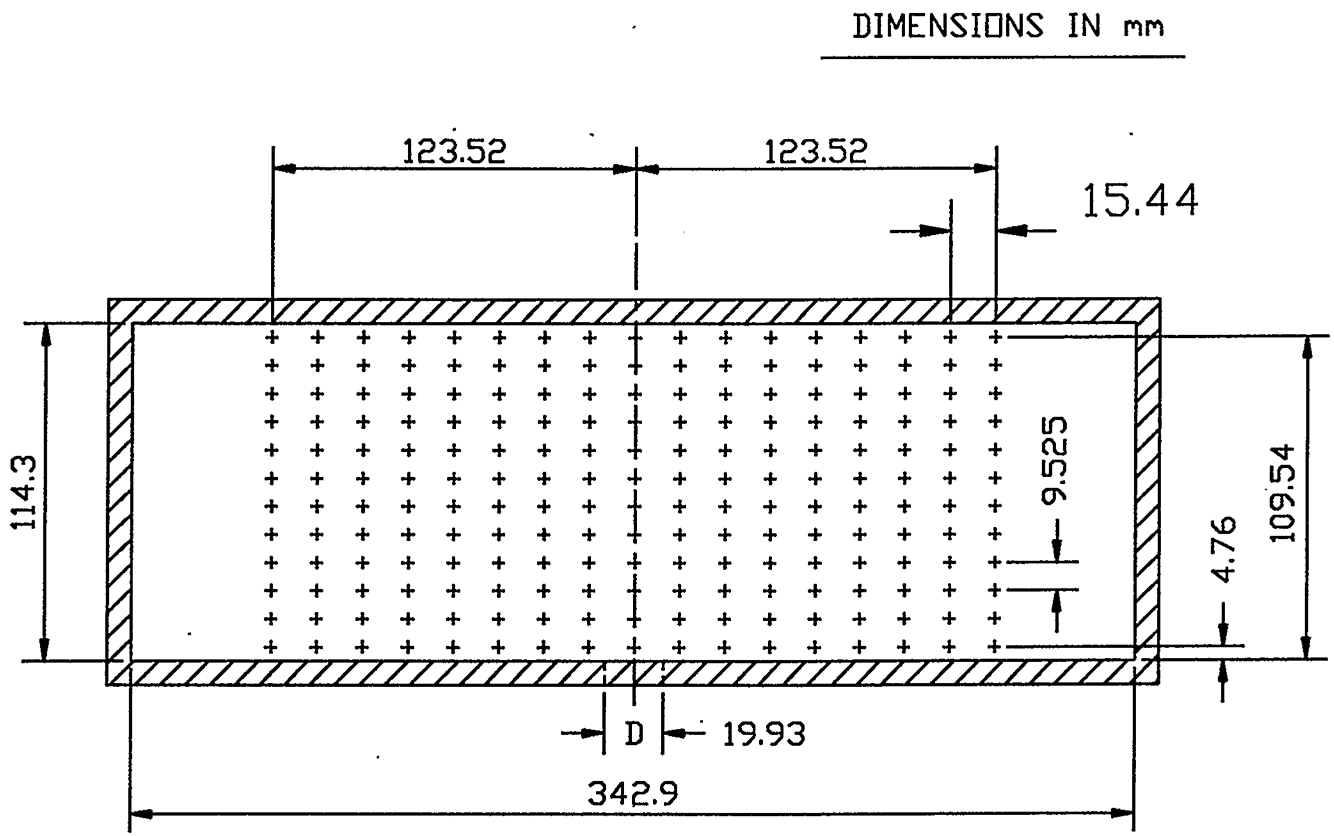

Fig. 4.12 Temperature Measurement Positions in Each Transverse Plane.

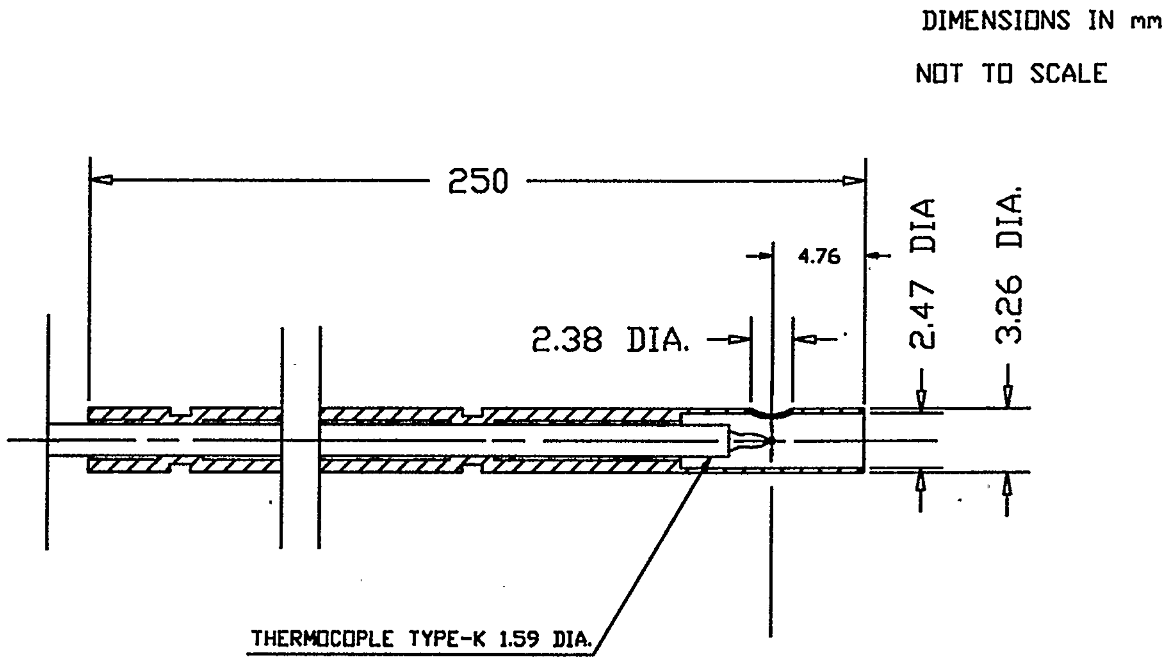

Fig. 4.13 Thermocouple Assembly for Stagnation Temperature Measurement.

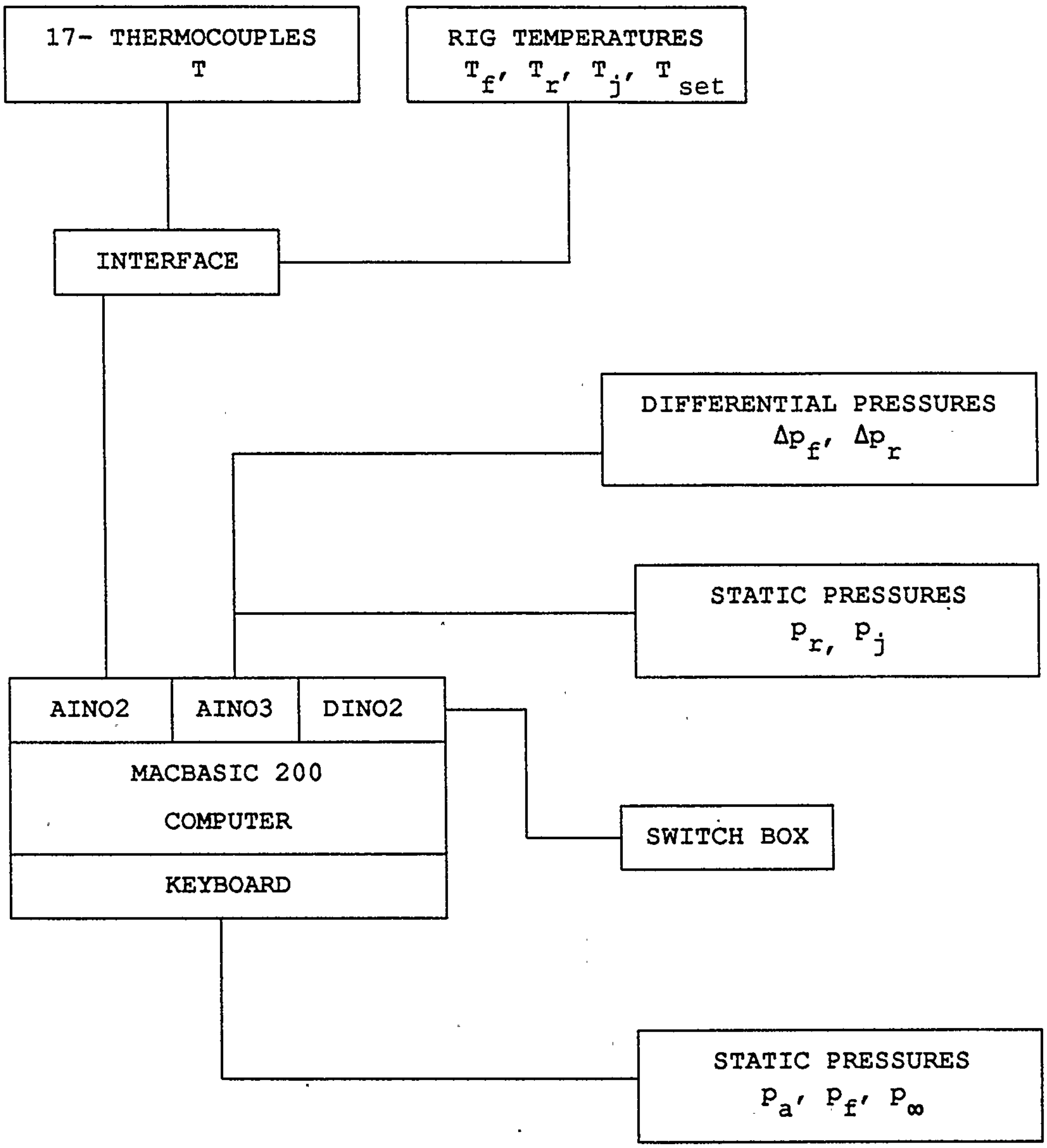

Fig. 4.14 Schematic Diagram of Measurement System.

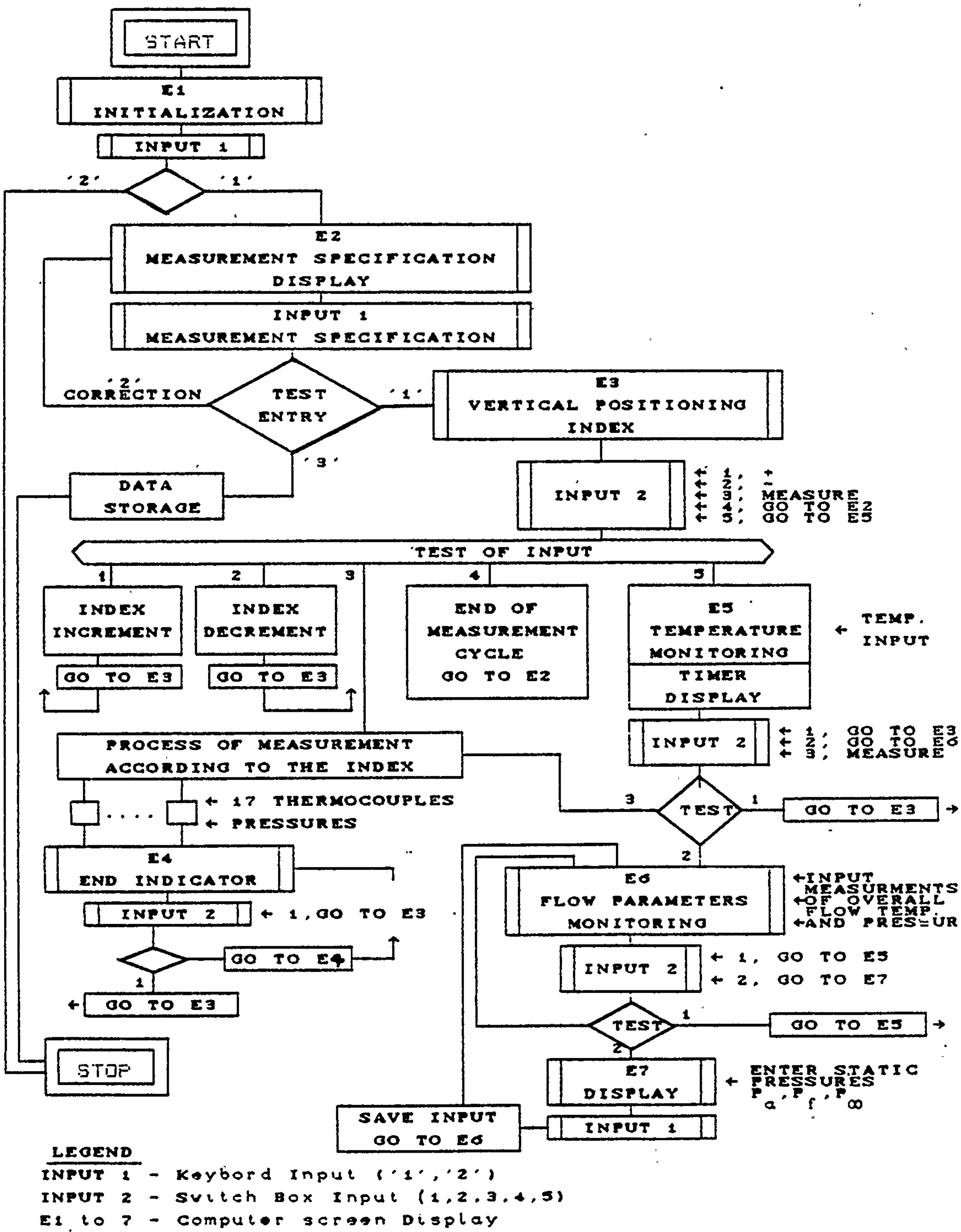

Fig. 4.15 Operational Schema of Data Acquisition System.

CHAPTER 5

EXPERIMENTAL RESULTS AND DISCUSSION

The results of the experiments are presented in the form of the dimensionless temperatures, Θ_m and Θ (dimensionless relative temperature or mixing parameter and dimensionless temperature difference ratio respectively), where:

- dimensionless relative temperature or mixing parameter

$$\Theta_m = \frac{T - T_m}{T_m - T_j} \qquad (5.1)$$

- dimensionless temperature difference ratio

$$\Theta = \frac{T_\infty - T}{\bar{T}_\infty - T_j} \qquad (5.2)$$

in which;

T - local mean temperature at a particular transverse plane,

T_m - average temperature at a particular transverse plane, (average of 204 local mean temperatures T)

T_j - average jet temperature,

T_{∞} - local mean temperature in reference transverse plane at X/D = -1.43,

$\bar{T}_{\infty}$ - average temperature of undisturbed crossflow in reference plane at X/D = -1.43 (average of 204 local mean temperatures T_{∞}).

The mixing parameter reflects the quality of the temperature profiles. A zero value of Θ_m implies an ideal flat temperature profile of magnitude T_m (theoretically achieved in a perfect mixing process).

The Θ profiles and contours show the jet temperature field. By definition Θ varies due to the difference between the temperature profile of the undisturbed flow and that of the flow disturbed by the jet. Therefore, Θ presents the jet temperature flow field independently of the quality of the reference (undisturbed) temperature profile. Maximum Θ corresponds to the coolest region of the flow, defining the jet centre-line for the centre-plane.

The actual study consists of two stages of investigation; (a) excitation level, and (b) Strouhal number influence, on jet mixing and penetration into the crossflow.

5.1 INVESTIGATION OF EXCITATION LEVEL INFLUENCE ON JET PENETRATION INTO THE CROSSFLOW

5.1.1 EXPERIMENTAL CONDITIONS AND PROCEDURE

In preliminary experiments, the consistency of the temperature field in the downstream planes without the jet was examined. This experiment consisted of checking the stability of the temperature profiles with time as well as with position along the test section. Fig. 5.1.1 displays the resulting temperature profiles in the form of Θ_m contours. The profiles show negligible differences, therefore for measurement convenience, the transverse plane at X/D=-1.43 was chosen as the reference one. Further experimental work proved that any variation of this undisturbed temperature field was mostly due to unsteadiness of the fuel delivery to the combustor. However, this problem was eliminated by the computer operated monitoring system allowing nearly instantaneous adjustments of the experimental parameters.

Experimental procedure at this stage of the experiment consisted of cycles of temperature profile measurements for different levels of jet excitation (acoustic driver powers). The cycle consisted of measurements at all transverse planes, i.e., X/D=-1.43, 1.43, 2.86, 5.72, 11.44 and 14.3. Although, the preliminary experiments showed excellent time steadiness of the reference transverse temperature profile at X/D=-1.43 the profile was continuously updated during the experiment to ensure reliability of the experimental results. As a result, the data showed that very steady repeatable conditions were maintained.

The "cold flow" study (Ref. 1 and 2) established the optimum jet flow response to be at a Strouhal number of 0.22 . Therefore, this value of the Strouhal number was taken as a reference for these experiments. Also, the other main flow variables were held in ranges close to that of the "cold flow" study, with the exception of the flow temperature. These variables are listed below (for comparison "cold flow" parameters are listed in brackets):

- average Strouhal number St=0.223 (0.22)
- acoustic driver power (excitation levels) $\dot{W}$ = 0.0, 15.0, 30.0, 45.0, 60.0, 75.0, 90.0 W (15.24, 31.0, 46.86, 60.2, 75.26, 90.9)
- jet to crossflow momentum flux ratio average value J=3.17 (3.89)
- jet to crossflow equivalent velocity ratio V_j/U_∞=1.81(1.97)
- Mach number of the crossflow Ma=0.03 (0.03),
- average temperature of the crossflow about 195.0^0C (48.0^0C),
- average temperature of the jet T_j=42.2^0C (42.0^0C).

The Mach number was selected at the low end of the operational range (0.03 to 0.07) of the reference combustor (Ref. 6) in order that the jet velocity used could be effectively pulsed by the driver power available. The maximum power applied to the loudspeaker was limited to 90 W (140 W possible) to avoid interference by the tunnel ceiling on the jet penetration.

5.1.2 TEST RESULTS "WITHOUT ACOUSTIC DRIVE"

The behaviour of jets in crossflow is already well documented in the technical literature (Chapter 2.1). The experimental test results of jet penetration into the crossflow "without acoustic drive" ($\dot{W}$=0.0 W) compared favourably with the literature and proved the reliability of the experimental set up.

Fig. 5.1.2 shows a comparison of experimental results with theoretical trajectory predictions for both "cold" (Ref. 1 and 2) and "hot" flow. From the nature of the experiment, there is a difference in defining the centre-line of the jet in these two cases of flow. In the "cold flow" case, the centre-line of a jet penetrating into a crossflow is defined by the maximum velocity of the jet flow; for the "hot flow" case, the centre-line relates to the minimum temperature of the jet flow. Despite the closeness of the jet to the crossflow momentum flux ratio, J, in both experiments, there is a noticeable discrepancy between the jet trajectories defined by velocity and temperature profiles. This difference was confirmed by Kamotani and Grebner Ref. 17 and Ramsey and Goldstein Ref. 38. Ramsey and Goldstein suggested that the air in the region of maximum velocity is in the upper outer zone of the jet which is sheared less than the fluid in the jet under-zone resulting in a distorted profile and displaced centre-line. It is also noticeable that the centre-line based on velocity profiles in the "cold flow" experiment is less than the theoretical predictions. Such behaviour can be explained as the effect of confined flow conditions, since all predictions are for an unconfined jet in "cold" crossflow, and moreover for a much higher momentum flux ratio in the range of J=5.0 to 60.0 . The only available prediction for single jet penetration into a confined crossflow, based on temperature profiles, was presented in the form of an equation for maximum jet penetration by Norster (Ref. 14). The experimental jet penetration at $X/D \geq 12.0$ closely approached that predicted by the Norster value for maximum penetration. In addition to the confined flow effect the discrepancy between predictions for the unconfined jet in "cold" and "hot" crossflow experimental results could be partially due to a negative buoyancy effect.

Referring to the Θ_m and Θ "no-drive" data of Figs. 5.1.3 and 5.1.4 the jet-wake zone is plainly visible, and in the transverse planes at X/D=1.43 and 2.86 the characteristic kidney-shaped jet cross-section appears. By X/D=11.44 the influence of the bound vortices has disappeared. In Fig. 5.1.3 the general nature of the crossflow temperature field is revealed with a cool layer at the tunnel ceiling being noticeable. As the mixing proceeded the temperature field outside of the cool layer, and over the jet-wake zone, became uniform to within ±13.5% of perfect mixing by X/D=14.30 . The data also shows,for the range covered, that the whole jet-wake region is bounded by the tunnel floor (Fig. 5.1.4). However, the Θ contour plots indicate that for X/D≥5.72 wake effects became weaker and a round cross-section jet zone was emerging. Also, the cross-sectional area of the jet wake zone increased as turbulent entrainment and mixing with the crossflow fluid proceeded. The jet had good symmetry about the centre-plane and the thermal axis of the jet coincided closely with the centre-plane. The general features of the jet-crossflow are consistent with the literature (Ref. 9 to 18), were repeatable, and therefore indicate that the behaviour was stable and normal.

5.1.3 TEST RESULTS "WITH ACOUSTIC DRIVE"

The results of the experiment are shown in two sets of contour graphs for increasing acoustic driver power. The first set presents contours for the mixing parameter Θ_m , and the second presents contours of the dimensionless temperature difference ratio Θ , for various cross-sections of the test section (Figs. 5.1.5 to 5.1.10 and Figs. 5.1.11 to 5.1.16 respectively). In addition, Figs. 5.1.17 to 5.1.22 and Figs. 5.1.23 to 5.1.28 present a direct comparison between "driven" and "no-driven" cases by means of the centre-plane profiles for Θ_m and Θ respectively.

The difference in the flow due to the acoustic excitation can be easily detected by simple visual comparison of the contour graphs. The changes produced by acoustic excitation are most pronounced in that the jet penetration as defined by the thermal jet trajectory, and the depth of the jet-wake region, were significantly increased. Generally, the temperature profiles are much flatter, with temperature minima significantly reduced, therefore demonstrating that the acoustic drive has strongly increased entrainment and mixing. The action of the jet under various "drive" conditions is clearly shown on the Θ contours and the Θ and Θ_m centre-plane vertical profiles. Even a relatively small acoustic driver power of 15 W caused significant changes in the flow temperature field. First of all, the initial kidney-like shape of the "no-driven" jet was modified to a more rounded one with increase of driver power. By distance X/D=2.86 the jet was almost round in cross-section, practically at all excitation levels. At X/D=1.43 there is still some residual flatness caused by incomplete transition from the "kidney-shape". By X/D=5.72 at 75W the mixing achieved is about the same as that for "no-drive" at X/D=11.44, also for "with-drive" the mixing zone occupies 92% of the tunnel flow height whereas for "no-drive" at X/D=11.44 it only occupies 71%. This indicates the mixing zone was increased and in a much shorter length.

The depth of the jet-wake region was significantly increased together with jet separation from the test chamber floor. At

X/D=1.43, for a driving power of 45W ,the jet is practically separated from the chamber floor. The penetration is so effective that the jet temperature field interferes with the ceiling boundary layer. This effect is illustrated by the flattening of the upper region of the Θ contours with increasing driving power. The interference of the ceiling upon the jet results in dramatic changes in the temperature profile pattern for powers greater than 60W for X/D≥5.72. At these conditions the remaining jet flow separated into two small zones travelling along the ceiling wall, perhaps the residual effects of the bound vortices? This results in a much thickened cool ceiling layer as shown by the Θ_m contours. Excluding the plots much distorted the ceiling acoustic drive has increased the depth of the combined jet-wake zone (little change in width), the temperature has significantly increased and is more uniform, demonstrating that entrainment and mixing were strongly increased. By X/D=14.30 the Θ_m contour plots for powers $\dot{W}\geq 30$ W indicate that a relatively flat temperature distribution (within ±5%, over the jet-wake zone width) has been achieved, except for the thickened cool ceiling layer. This indicates that the mixing was nearly complete, in contrast to the "no-drive" situation.

5.1.4 DISCUSSION

The centre-plane structure of the jet in the hot crossflow of Fig. 5.1.29, when compared with that for the cold flow study of (Ref. 1 and 2), shows about 34% less penetration at X/D=2.86 (see also Fig. 5.1.2). The difference is due to the previously mentioned discrepancy in velocity and temperature profiles, experimental variation of momentum flux ratio and possibly due to buoyancy effects (since for the hot crossflow $\rho_j/\rho_\infty=1.52$ versus 1.04 for the cold flow study).

The centre-plane thermal trajectories allow the increase in jet penetration with relative pulsation strength V_e/V_j to be determined (Fig. 5.1.30). Using the relative pulsation strength power number calibration the data are presented in Fig. 5.1.31 as a function of V_e/V_j, for various downstream locations. The increased jet penetration with acoustic drive is strong, and for X/D>5.72 and $V_e/V_j>0.93$ the tunnel ceiling suppresses the penetration (see also Θ contours, Figs. 5.1.13 to 5.1.16). At X/D=1.43 and 2.86 there is no tunnel ceiling interference. Some further gains in the penetration are expected to be achieved by increasing the excitation beyond $V_e/V_j=1.30$.

Plots of the maximum of the dimensionless temperature difference ratio Θmax versus downstream distance X/D (Fig. 5.1.32) and excitation level (Fig. 5.1.33) show changes in jet centre-line temperature and may show changes in the flatness of the temperature profiles. At the X/D=1.43 transverse plane there is about a 35% decrease in Θmax for V_e/V_j>0.54 compared to the "no-drive" case. The scatter of data points for power conditions higher than 60 W ($V_e/V_j \geq 1.05$) at downstream distances X/D≥11.43 shows strong ceiling interference drastically modifying the flow pattern (see also Figs. 5.1.14 to 5.1.16).

The overall mixing effectiveness in a particular transverse plane may be assessed by the standard deviation;

$$S_m = \left[\frac{\sum_{i=1}^{n} (T-T_m)^2}{n-1} \right]^{1/2} \qquad (5.3)$$

This parameter when normalized as $S_m/(T_m-T_j)$ may be termed as the relative mixing effectiveness. Fig. 5.1.34 plots the relative mixing effectiveness versus X/D. The calculations were only performed for a width between 125 mm and 217 mm, and for a height from 4.8 mm to 81 mm, in order to eliminate masking by the temperature field outside this acoustically active zone, essentially a signal to noise problem. When mixing is perfect $T=T_m$, and the relative mixing effectiveness becomes zero. Therefore, as mixing proceeds with X/D this parameter tends to zero, as shown by Fig. 5.1.34 and also tends to zero as V_e/V_j is increased (Fig. 5.1.35). However, because the temperature distribution in the reference plane, just upstream of the jet orifice, is not ideally flat the relative mixing effectiveness reduces as mixing proceeds to an asymptotic value determined by the upstream temperature distribution. This asymptotic value or "noise" for the reference plane is shown in Fig. 5.1.36. Also for powers greater than 30 W the jet penetrates into the cold ceiling layer when X/D approaches 11.44 and the above asymptotic value is reached. Thus, the "no-drive" mixed state at X/D=14.30 is achieved at X/D=4.3 for an acoustic excitation of V_e/V_j = 1.30 (90W), in other words the superior mixed state at X/D=14.30 (near the asymptotic value) has been attained at a much shorter distance by acoustic excitation. The length to achieve a given mixed state has therefore been shortened by 70%, in this case, and the mixing has been significantly increased by acoustic excitation, which is in agreement with Ref. (2). It will also be noticed from Fig. 5.1.35 that the improvement in mixing showed a saturation tendency taking place as V_e/V_j was increased, which again agrees with Ref. (2). Some further small improvement in mixing and reduction in length to reach a given mixed state may therefore occur for powers greater than 90W (V_e/V_j =1.30). Since mixing is directly related to entrainment, and Vermeulen, et al. (Ref. 5) found that the increase in entrainment mass flow rate saturated with acoustic drive, it is not surprising that the mixing also saturates and for the same reason. This is probably due to jet column disintegration or excitation of the toroidal vibration mode of the toroidal vortices shedding from the orifice. In addition, this statement can be confirmed by plots of the net variation of the relative mixing effectiveness, i.e. the differences between "no-drive" and "drive" cases of this parameter. Fig. 5.1.37 and 5.2.38 show the variation of this parameter versus downstream distance and pulsation strength, respectively. These plots confirm the saturation tendency particularly for excitations $V_e/V_j \geq 0.93$.

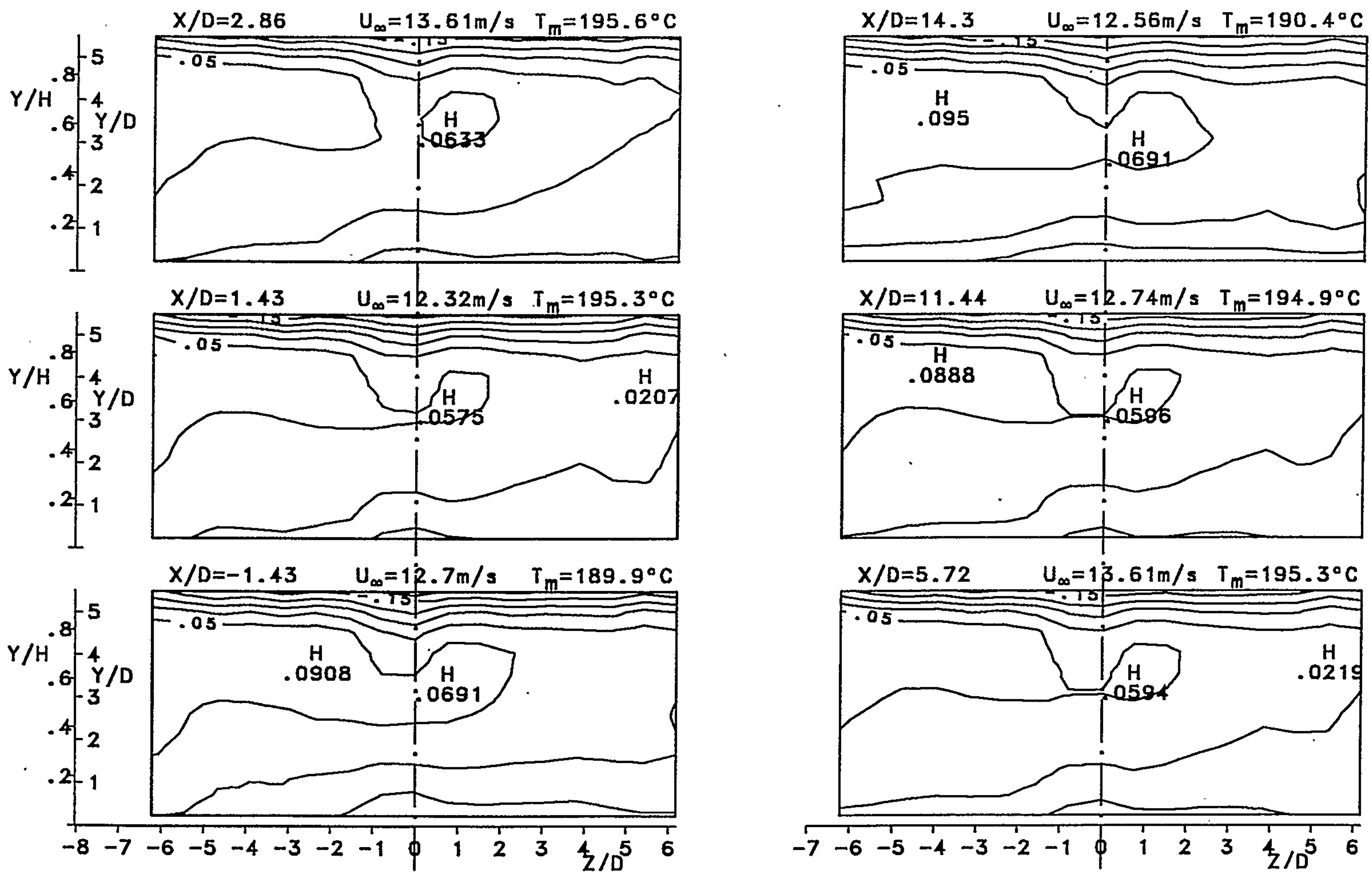

Fig. 5.1.1 Θ_m Mean Temperature Contour Maps for No Jet Flow, Contour Interval 0.05.

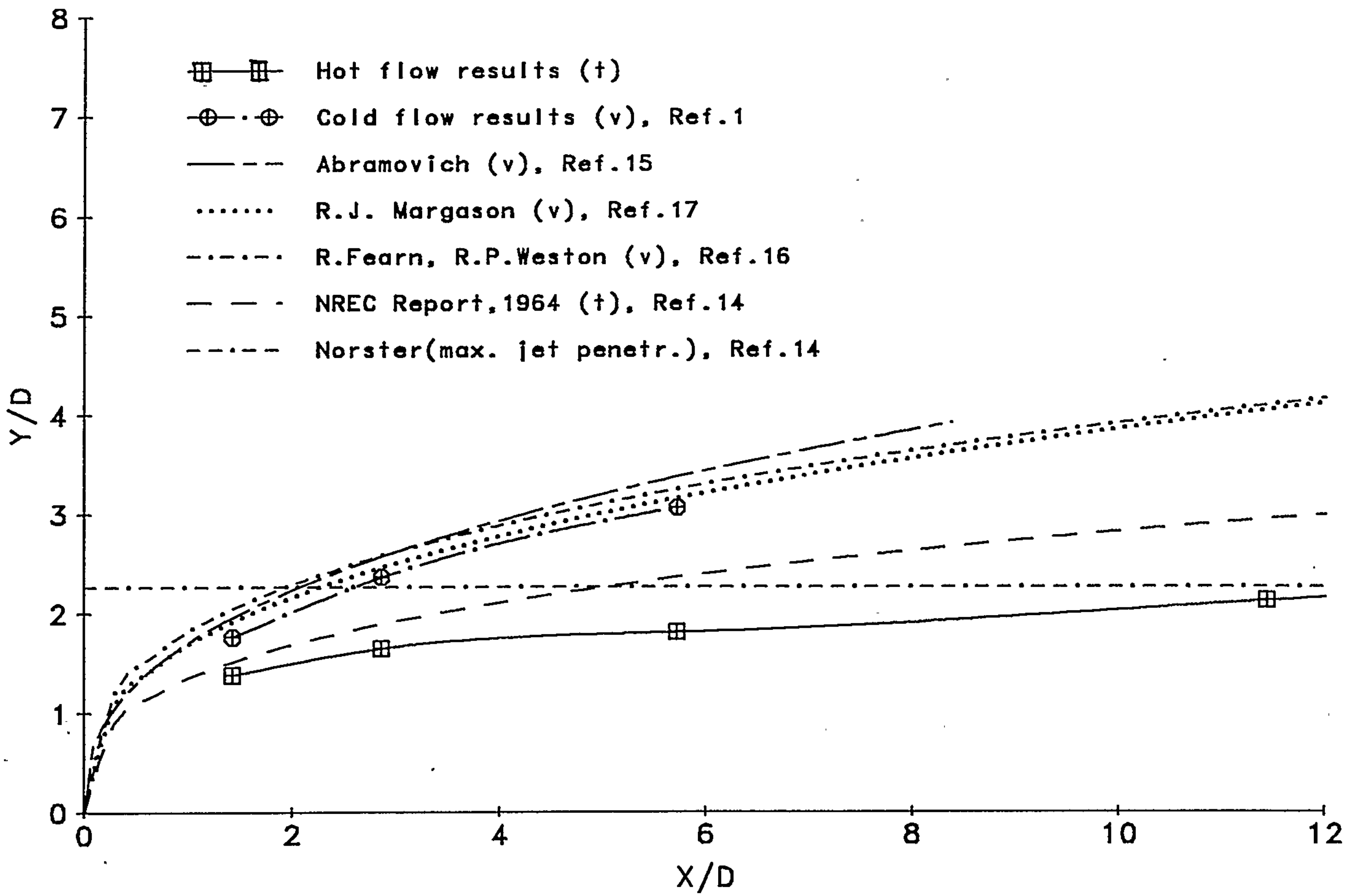

Fig. 5.1.2 Comparison of Jet Penetration Experimental Results with Theoretical Predictions.
(v) - velocity ; (t) - temperature based prediction.

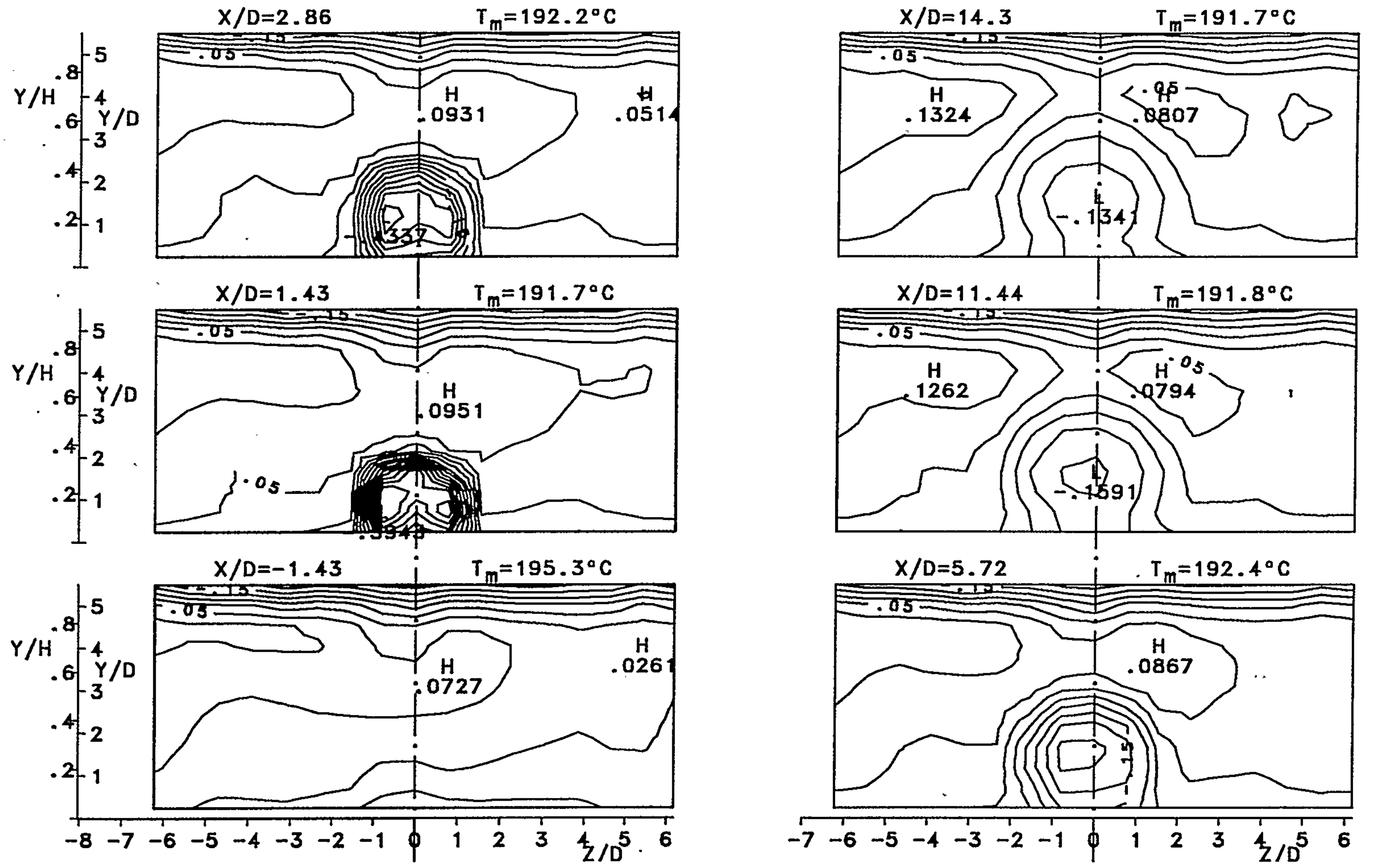

Fig.5.1.3 Θ_m Contour Maps for "no-drive" Case, Contour Interval 0.05.

St = 0.	ρ_∞ = .6552 kg/m^3	ρ_j = .9949 kg/m^3	T_j = 41.4 °C	D = 19.93 mm
$\dot{W}$ = 0. W	$\dot{M}_\infty$ = .3301 kg/s	$\dot{M}_j$ = .0057 kg/s	J = 3.108	f = 0 Hz
Ma = .0297	U_∞ = 12.85 m/s	V_j = 18.39 m/s	V_j/U_∞ = 1.432	
V_e/V_j = 0.	Re_∞ = 57005.	Re_j = 19037.	$\dot{M}_j/\dot{M}_\infty$ = .0173	

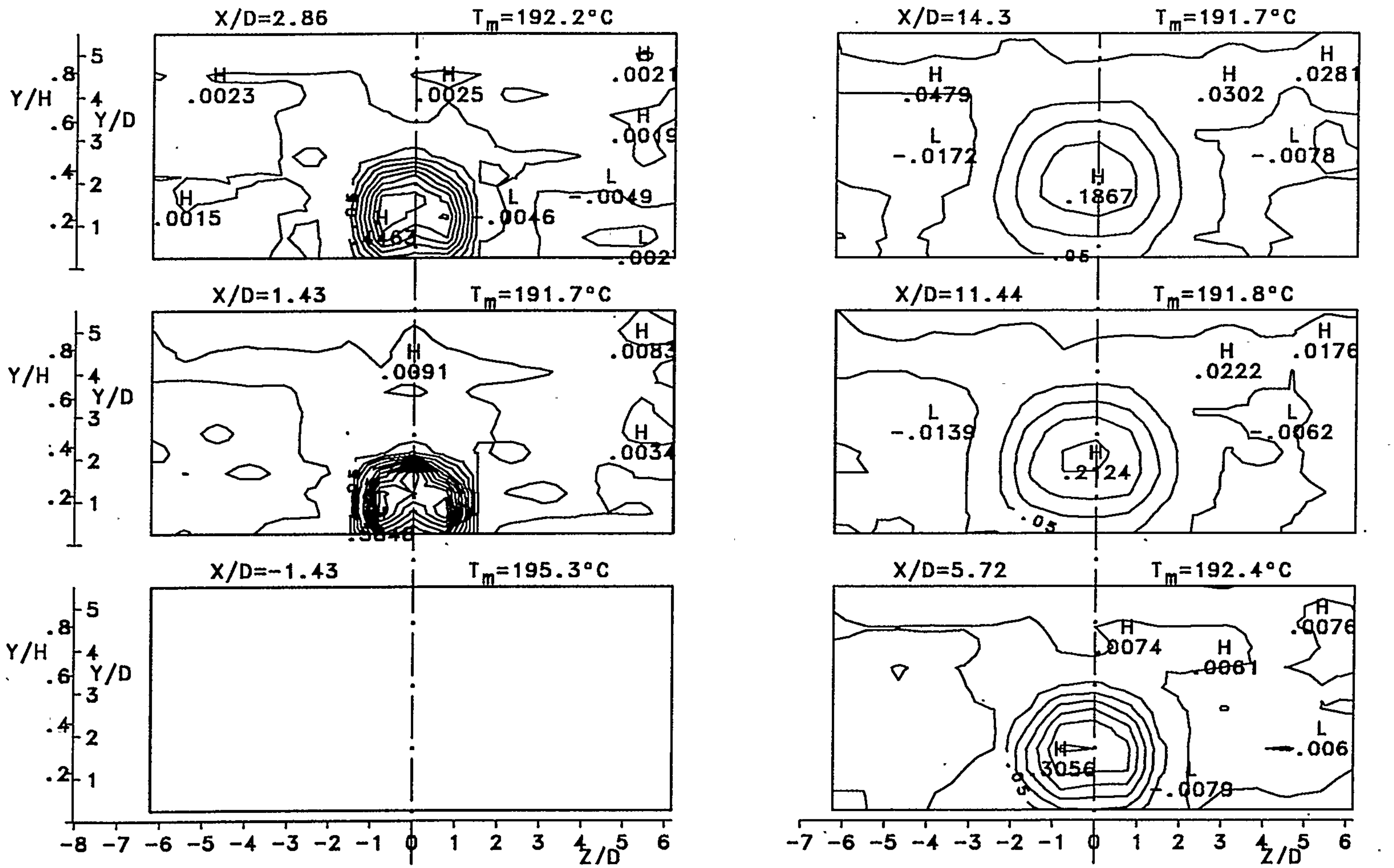

Fig.5.1.4 Θ Contour Maps for "no-drive" Case, Contour Interval 0.05.

$St = 0.$	$\rho_\infty = .6552$ kg/m^3	$\rho_I = .9949$ kg/m^3	$T_I = 41.4$ °C	$D = 19.93$ mm
$\dot{W} = 0.$ W	$\dot{M}_\infty = .3301$ kg/s	$\dot{M}_I = .0057$ kg/s	$J = 3.108$	$f = 0$ Hz
$Ma = .0297$	$U_\infty = 12.85$ m/s	$V_I = 18.39$ m/s	$V_I/U_\infty = 1.432$	
$V_e/V_I = 0.$	$Re_\infty = 57005.$	$Re_I = 19037.$	$\dot{M}_I/\dot{M}_\infty = .0173$	

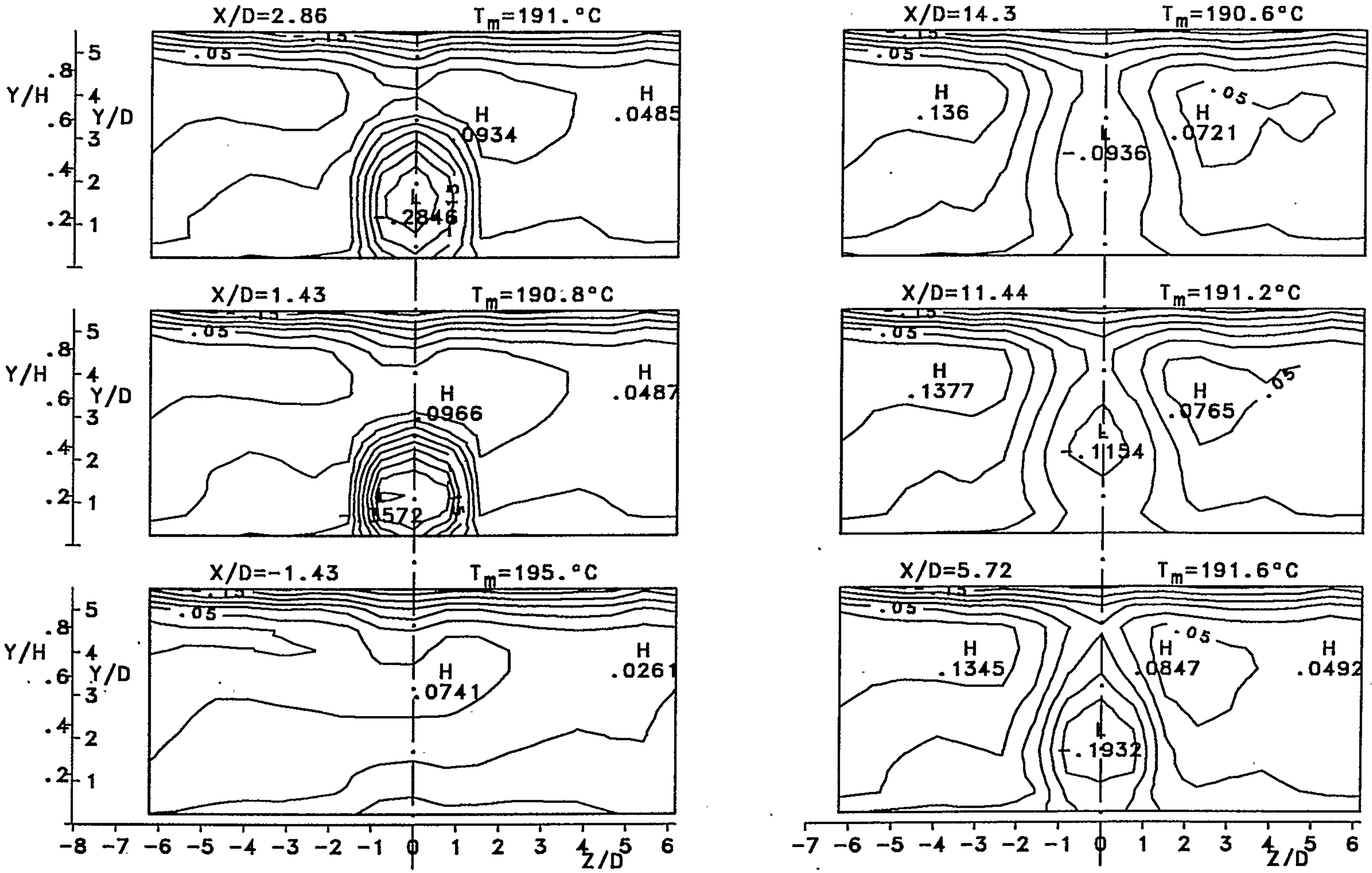

Fig.5.1.5 Θ_m Contour Maps for 15.W Power "drive" Case, Contour Interval 0.05.

St = .224	ρ_∞ = .6951 kg/m^3	ρ_j = .9799 kg/m^3	T_j = 42.2 °C	D = 19.93 mm
$\dot{W}$ = 15. W	$\dot{M}_\infty$ = .3238 kg/s	$\dot{M}_j$ = .0055 kg/s	J = 3.177	f = 204 Hz
Ma = .028	U_∞ = 12.09 m/s	V_j = 18.15 m/s	V_j/U_∞ = 1.526	
V_e/V_j = .5383	Re_∞ = 56889.	Re_j = 18506.	$\dot{M}_j/\dot{M}_\infty$ = .0171	

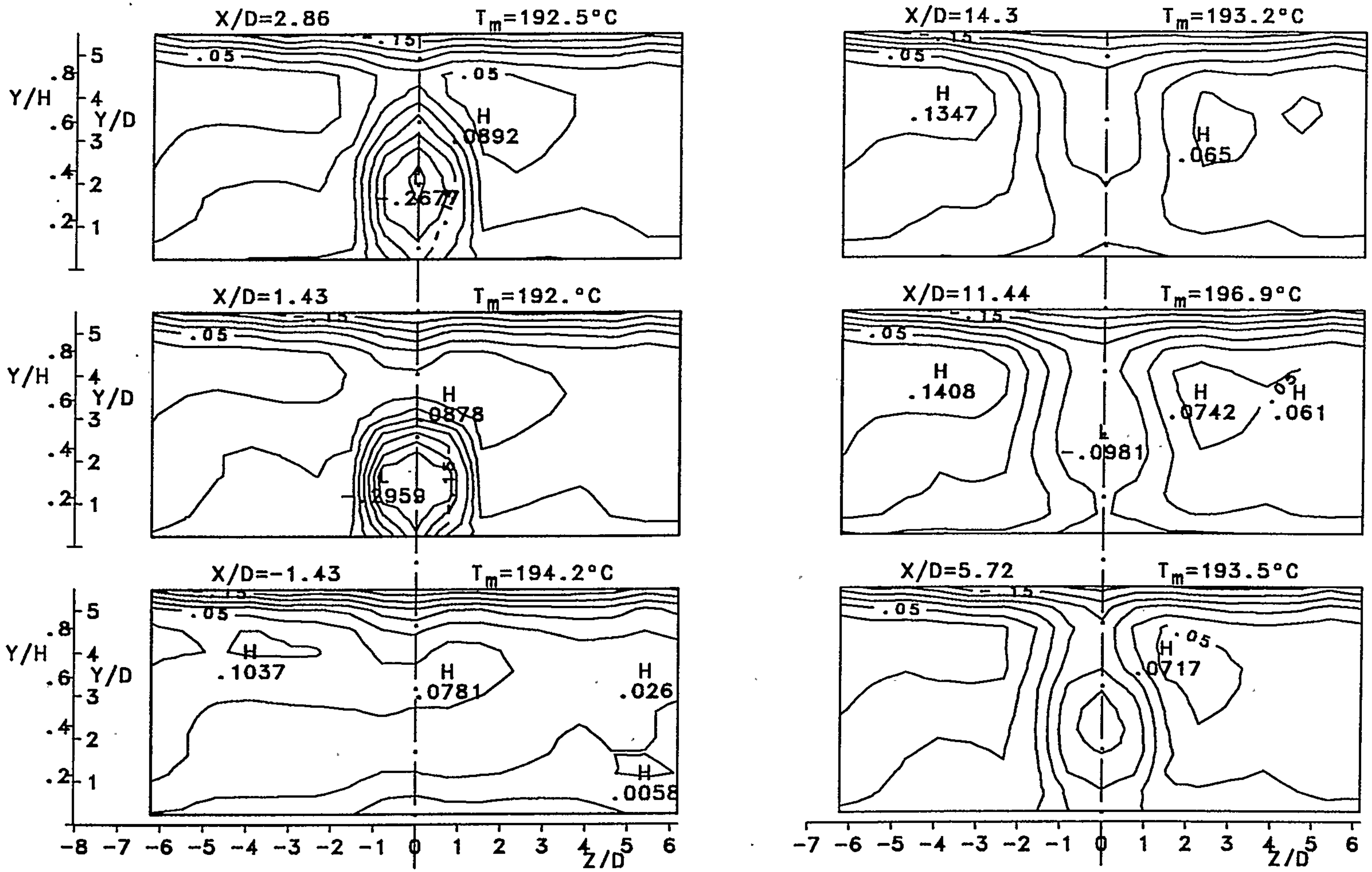

Fig.5.1.6 Θ_m Contour Maps for 30.W Power "drive" Case, Contour Interval 0.05.

St = .2295	ρ_∞ = .7396 kg/m^3	ρ_I = .9911 kg/m^3	T_I = 42.5 °C	D = 19.93 mm
$\dot{W}$ = 30. W	$\dot{M}_\infty$ = .3345 kg/s	$\dot{M}_I$ = .0055 kg/s	J = 2.991	f = 204 Hz
Ma = .0275	U_∞ = 11.86 m/s	V_I = 17.71 m/s	V_I/U_∞ = 1.541	
V_e/V_I = .7853	Re_∞ = 59351.	Re_I = 18265.	$\dot{M}_I/\dot{M}_\infty$ = .0164	

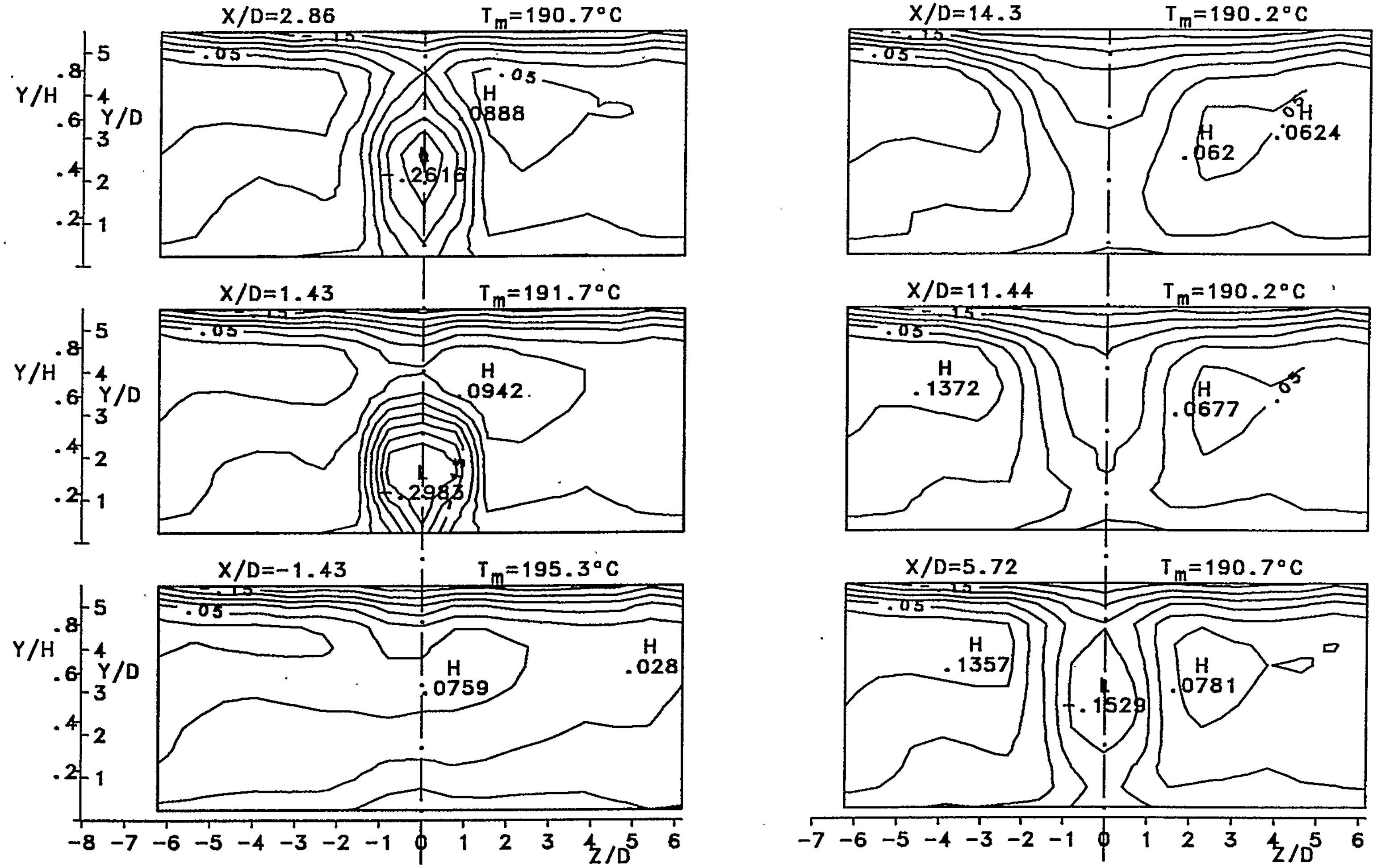

Fig.5.1.7 Θ_m Contour Maps for 45.W Power "drive" Case, Contour Interval 0.05.

St = .2228	ρ_∞ = .6951 kg/m^3	ρ_j = .9799 kg/m^3	T_j = 42.5 °C	D = 19.93 mm
$\tilde{W}$ = 45. W	$\dot{M}_\infty$ = .3284 kg/s	$\dot{M}_j$ = .0056 kg/s	J = 3.141	f = 204 Hz
Ma = .0283	U_∞ = 12.22 m/s	V_j = 18.25 m/s	V_j/U_∞ = 1.516	
V_e/V_j = .9253	Re_∞ = 57507.	Re_j = 18601.	$\dot{M}_j/\dot{M}_\infty$ = .017	

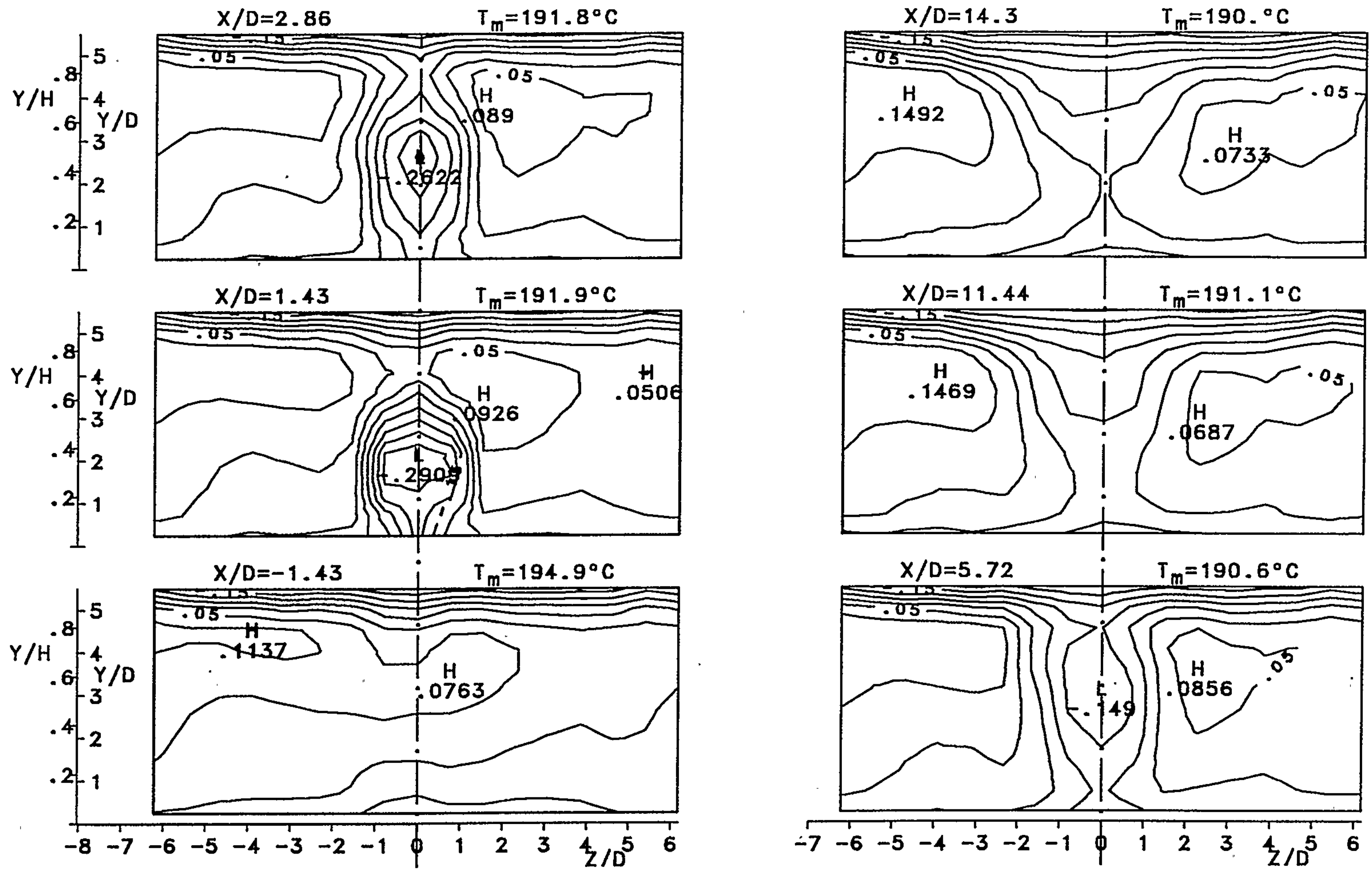

Fig.5.1.8 Θ_m Contour Maps for 60.W Power "drive" Case, Contour Interval 0.05.

St = .2213	ρ_∞ = .7776 kg/m^3	ρ_j = .9858 kg/m^3	T_j = 42.1 °C	D = 19.93 mm
$\dot{W}$ = 60. W	$\dot{M}_\infty$ = .3262 kg/s	$\dot{M}_j$ = .0056 kg/s	J = 3.531	f = 204 Hz
Ma = .0255	U_∞ = 11.01 m/s	V_j = 18.37 m/s	V_j/U_∞ = 1.718	
V_e/V_j= 1.055	Re_∞ = 57928.	Re_j = 18839.	$\dot{M}_j/\dot{M}_\infty$ = .0173	

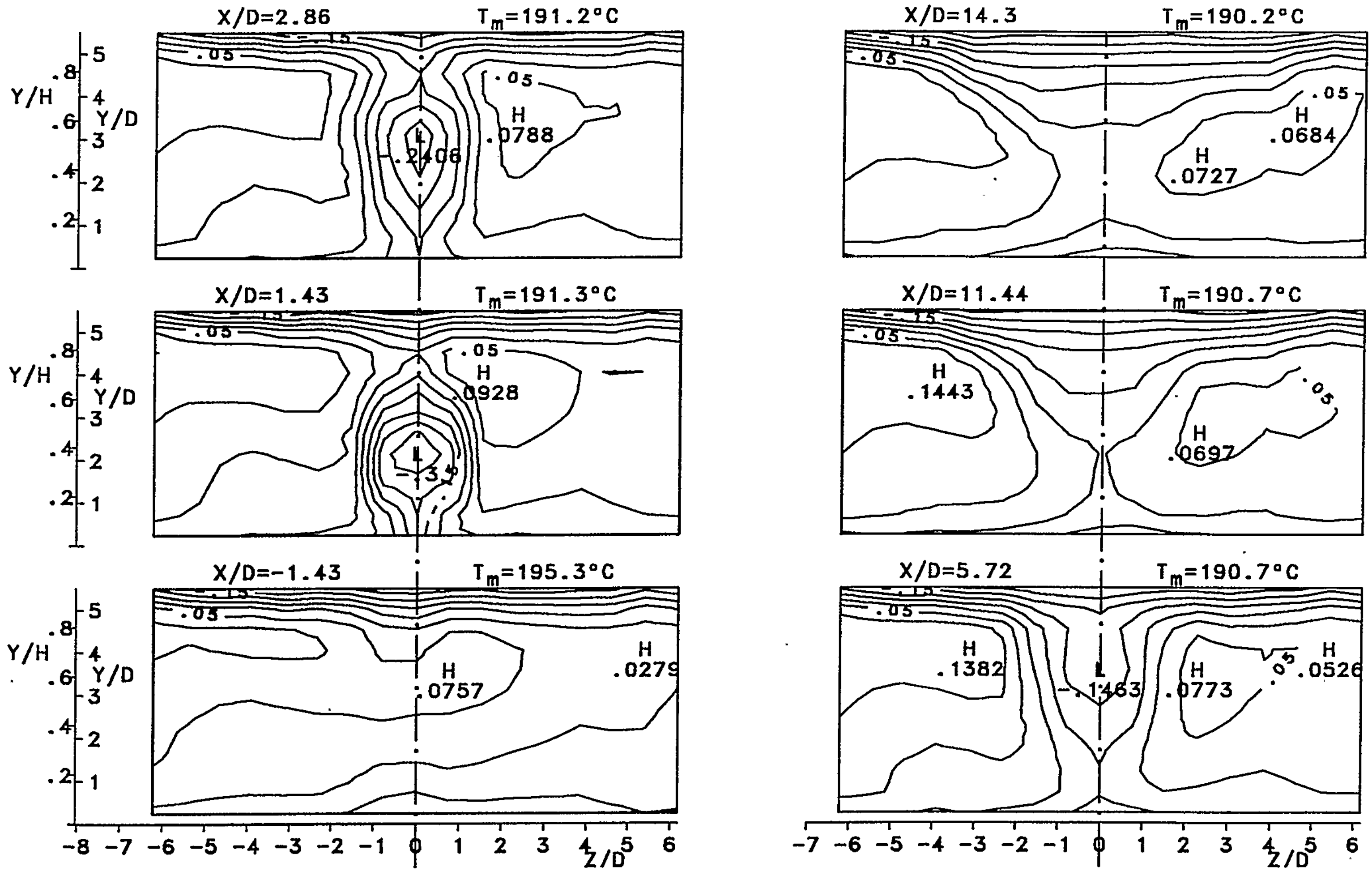

Fig.5.1.9 Θ_m Contour Maps for 75.W Power "drive" Case, Contour Interval 0.05.

$St = .2194$
$\dot{W} = 75.$ W
$Ma = .0297$
$V_e/V_j = 1.165$

$\rho_\infty = .651$ kg/m^3
$\dot{M}_\infty = .3274$ kg/s
$U_\infty = 12.84$ m/s
$Re_\infty = 56557.$

$\rho_j = .9838$ kg/m^3
$\dot{M}_j = .0057$ kg/s
$V_j = 18.53$ m/s
$Re_j = 18967.$

$T_j = 41.5$ °C
$J = 3.149$
$V_j/U_\infty = 1.446$
$\dot{M}_j/\dot{M}_\infty = .0174$

$D = 19.93$ mm
$f = 204$ Hz

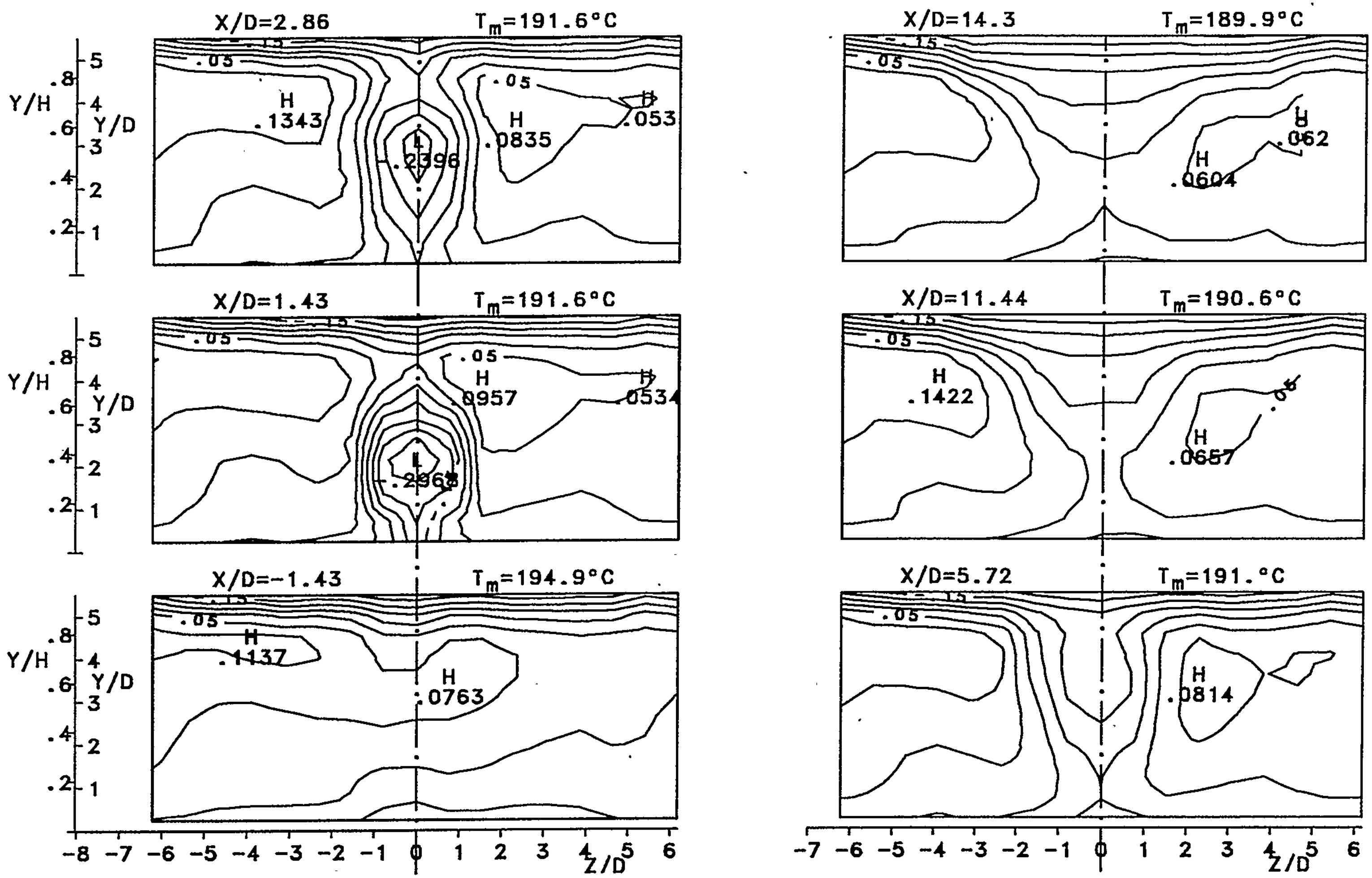

Fig.5.1.10 Θ_m Contour Maps for 90.W Power "drive" Case, Contour Interval 0.05.

St = .2223	ρ_∞ = .6869 kg/m^3	ρ_j = .9822 kg/m^3	T_j = 42.8 °C	D = 19.93 mm
$\hat{W}$ = 90. W	$\dot{M}_\infty$ = .3267 kg/s	$\dot{M}_j$ = .0056 kg/s	J = 3.171	f = 204 Hz
Ma = .0284	U_∞ = 12.28 m/s	V_j = 18.29 m/s	V_j/U_∞ = 1.509	
V_e/V_j = 1.302	Re_∞ = 57103.	Re_j = 18691.	$\dot{M}_j/\dot{M}_\infty$ = .0172	

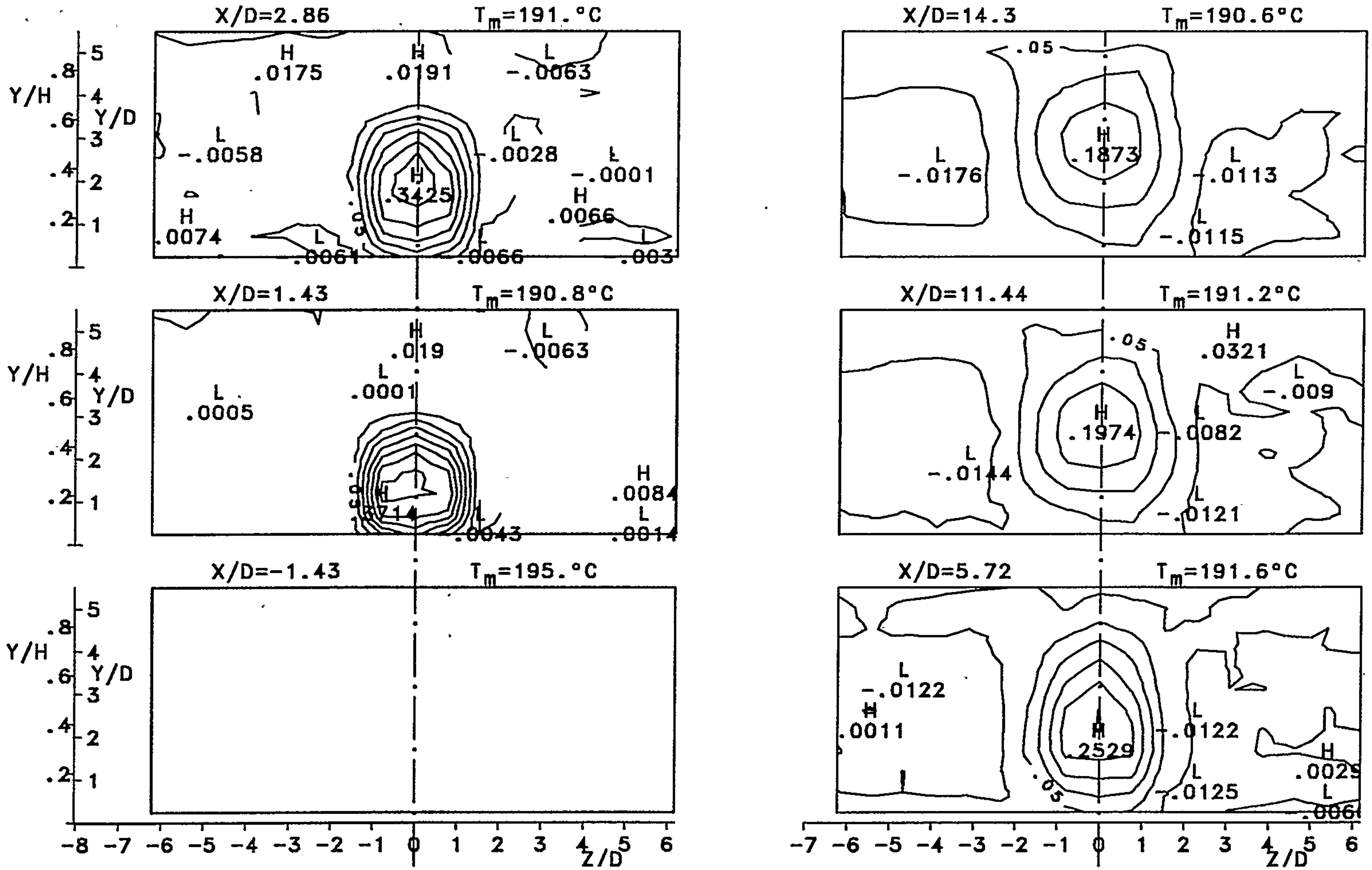

Fig.5.1.11 Θ Contour Maps for 15.W Power "drive" Case, Contour Interval 0.05.

St = .224	ρ_∞ = .6951 kg/m^3	ρ_j = .9799 kg/m^3	T_j = 42.2 °C	D = 19.93 mm
$\dot{W}$ = 15. W	$\dot{M}_\infty$ = .3238 kg/s	$\dot{M}_j$ = .0055 kg/s	J = 3.177	f = 204 Hz
Ma = .028	U_∞ = 12.09 m/s	V_j = 18.15 m/s	V_j/U_∞ = 1.526	
V_e/V_j = .5383	Re_∞ = 56889.	Re_j = 18506.	$\dot{M}_j/\dot{M}_\infty$ = .0171	

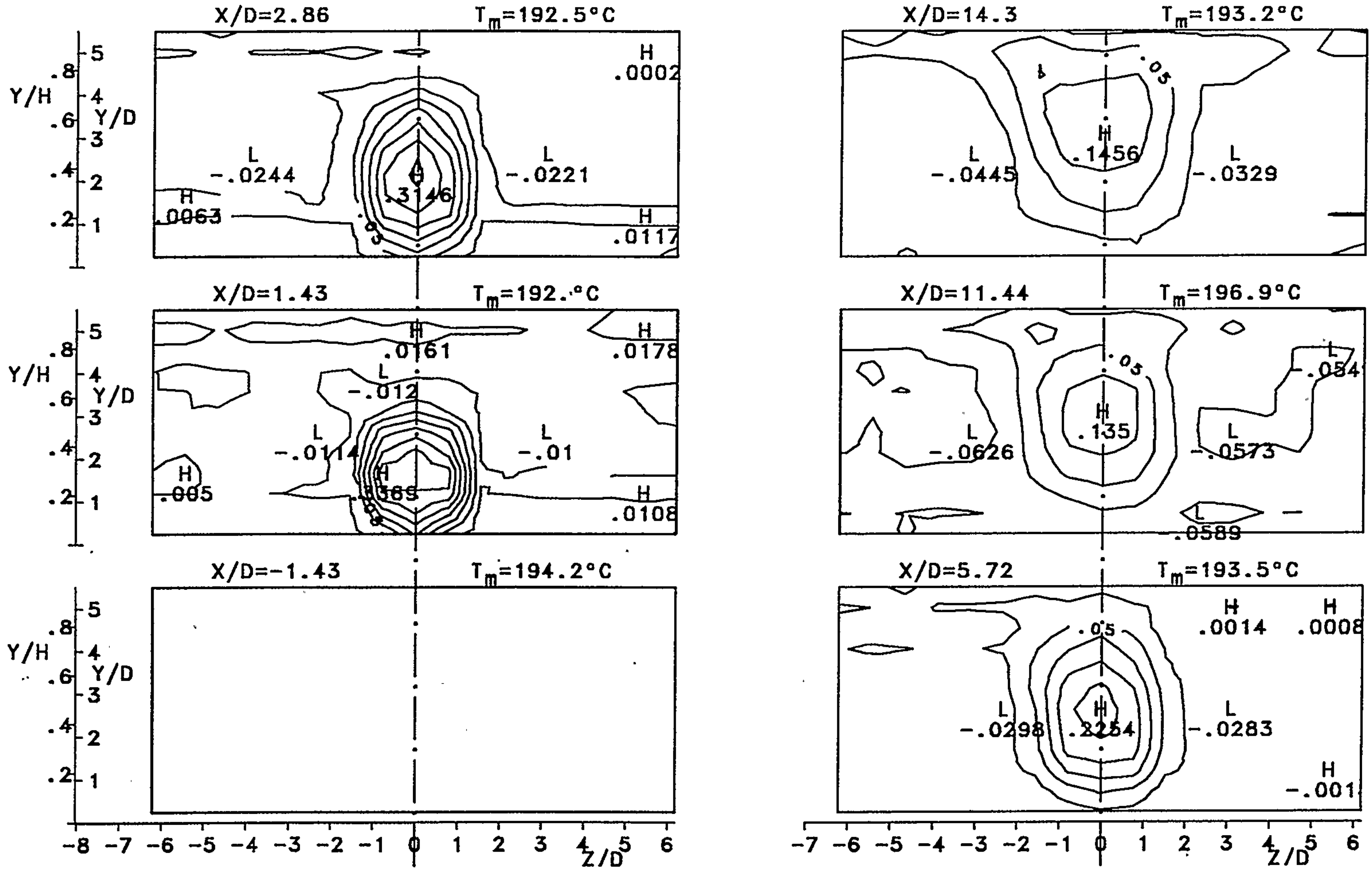

Fig.5.1.12 Θ Contour Maps for 30.W Power "drive" Case, Contour Interval 0.05.

St = .2295	ρ_∞ = .7396 kg/m^3	ρ_j = .9911 kg/m^3	T_j = 42.5 °C	D = 19.93 mm
$\hat{W}$ = 30. W	$\dot{M}_\infty$ = .3345 kg/s	$\dot{M}_j$ = .0055 kg/s	J = 2.991	f = 204 Hz
Ma = .0275	U_∞ = 11.86 m/s	V_j = 17.71 m/s	V_j/U_∞ = 1.541	
V_e/V_j = .7853	Re_∞ = 59351.	Re_j = 18265.	$\dot{M}_j/\dot{M}_\infty$ = .0164	

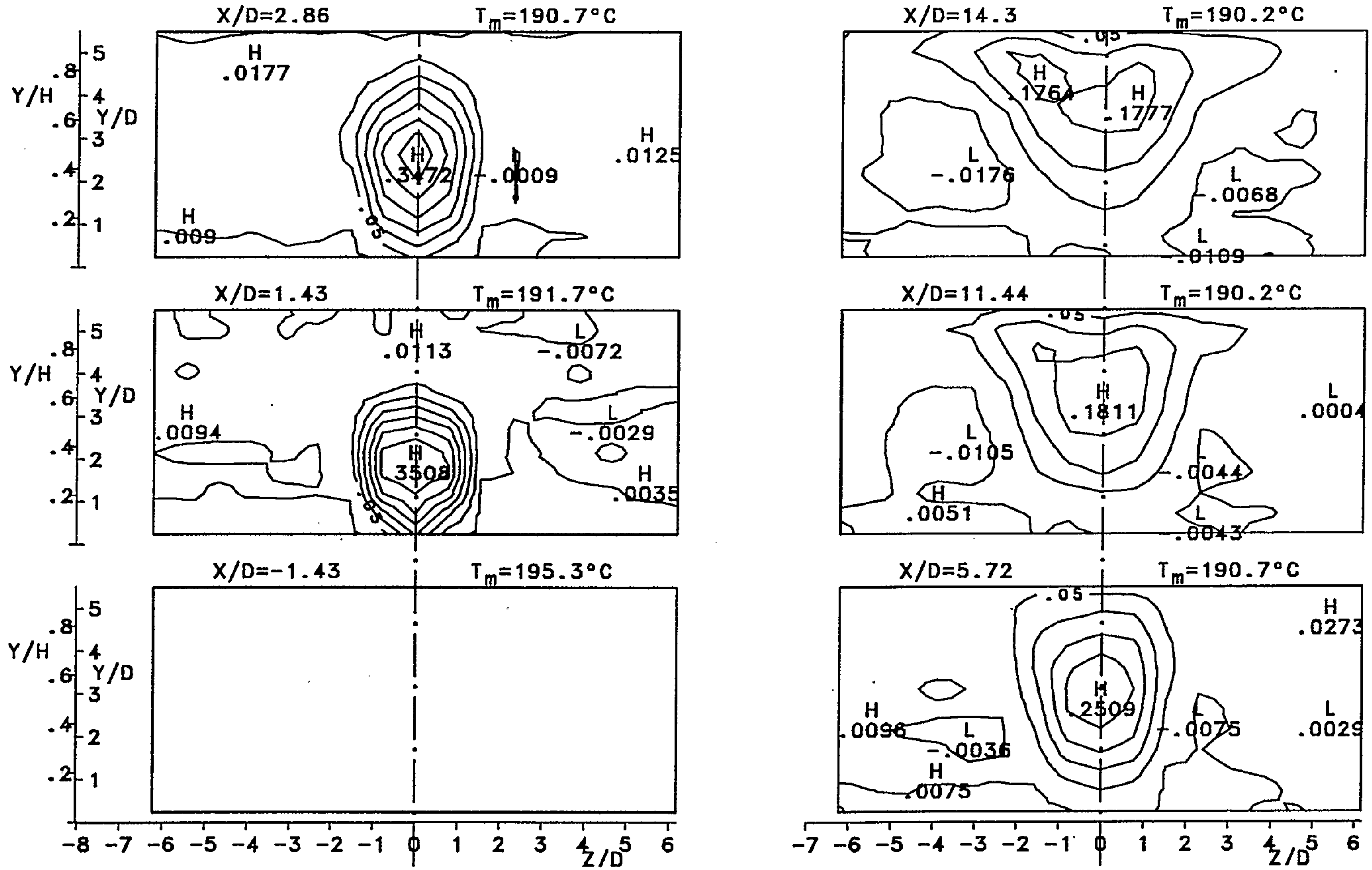

Fig.5.1.13 Θ Contour Maps for 45.W Power "drive" Case, Contour Interval 0.05.

St = .2228	ρ_∞ = .6951 kg/m^3	ρ_j = .9799 kg/m^3	T_j = 42.5 °C	D = 19.93 mm
$\dot{W}$ = 45. W	$\dot{M}_\infty$ = .3284 kg/s	$\dot{M}_j$ = .0056 kg/s	J = 3.141	f = 204 Hz
Ma = .0283	U_∞ = 12.22 m/s	V_j = 18.25 m/s	V_j/U_∞ = 1.516	
V_e/V_j = .9253	Re_∞ = 57507.	Re_j = 18601.	$\dot{M}_j/\dot{M}_\infty$ = .017	

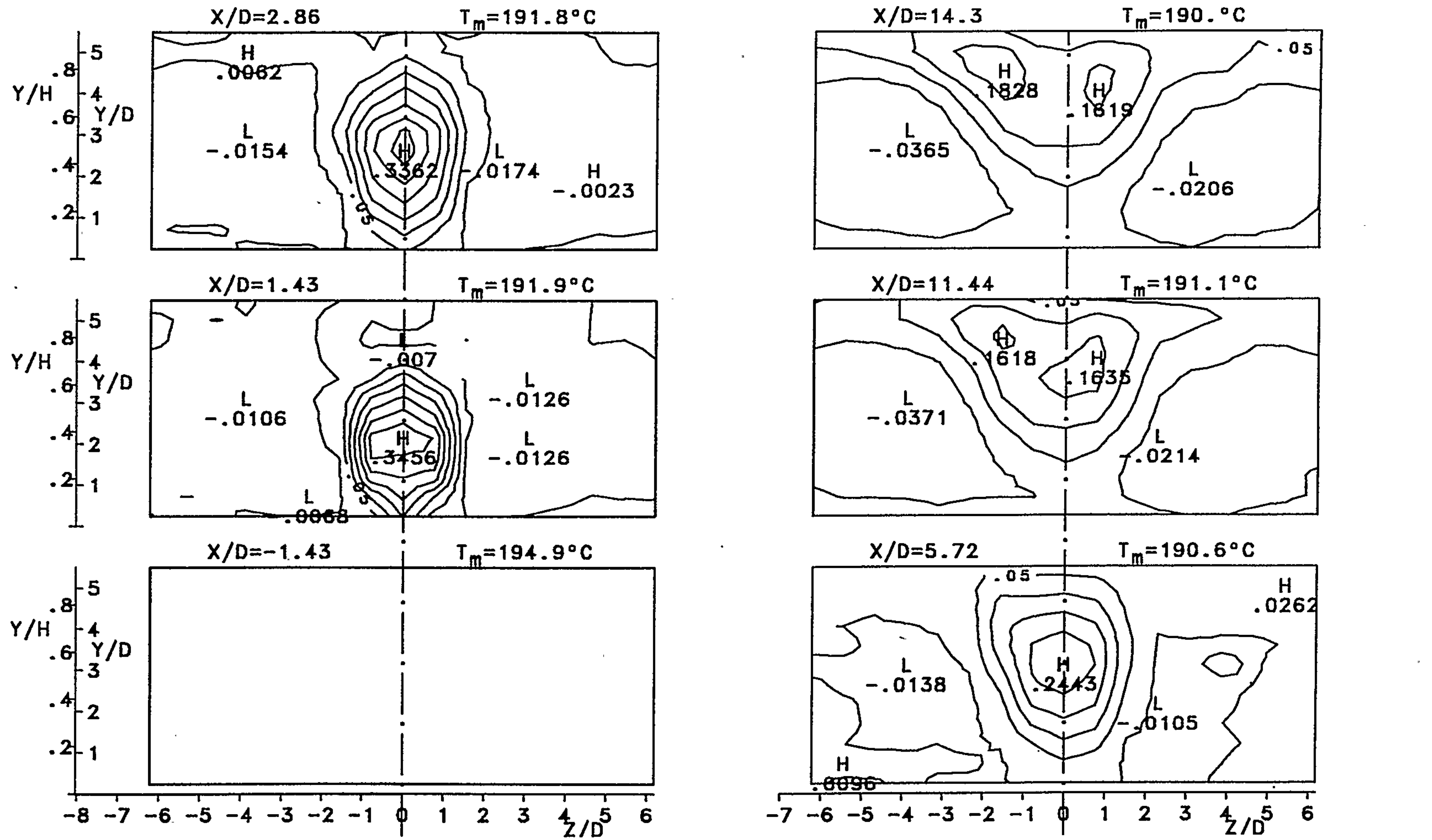

Fig.5.1.14 Θ Contour Maps for 60.W Power "drive" Case, Contour Interval 0.05.

St = .2213	ρ_∞ = .7776 kg/m^3	ρ_j = .9858 kg/m^3	T_j = 42.1 °C	D = 19.93 mm
$\dot{W}$ = 60. W	$\dot{M}_\infty$ = .3262 kg/s	$\dot{M}_j$ = .0056 kg/s	J = 3.531	f = 204 Hz
Ma = .0255	U_∞ = 11.01 m/s	V_j = 18.37 m/s	V_j/U_∞ = 1.718	
V_e/V_j = 1.055	Re_∞ = 57928.	Re_j = 18839.	$\dot{M}_j/\dot{M}_\infty$ = .0173	

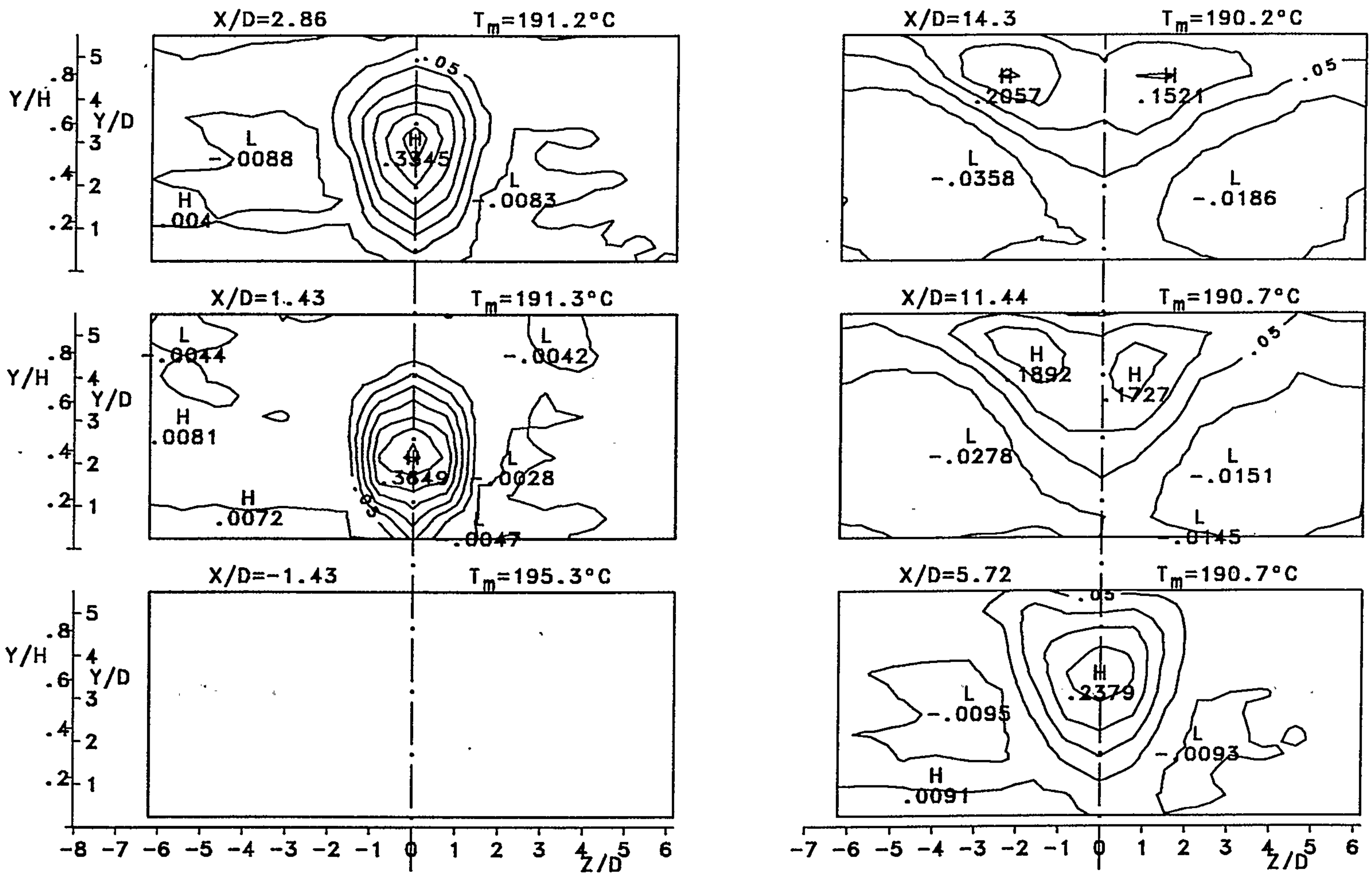

Fig.5.1.15 Θ Contour Maps for 75.W Power "drive" Case, Contour Interval 0.05.

St = .2194
$\dot{W}$ = 75. W
Ma = .0297
V_e/V_j = 1.165

ρ_∞ = .651 kg/m^3
$\dot{M}_\infty$ = .3274 kg/s
U_∞ = 12.84 m/s
Re_∞ = 56557.

ρ_j = .9838 kg/m^3
$\dot{M}_j$ = .0057 kg/s
V_j = 18.53 m/s
Re_j = 18967.

T_j = 41.5 °C
J = 3.149
V_j/U_∞ = 1.446
$\dot{M}_j/\dot{M}_\infty$ = .0174

D = 19.93 mm
f = 204 Hz

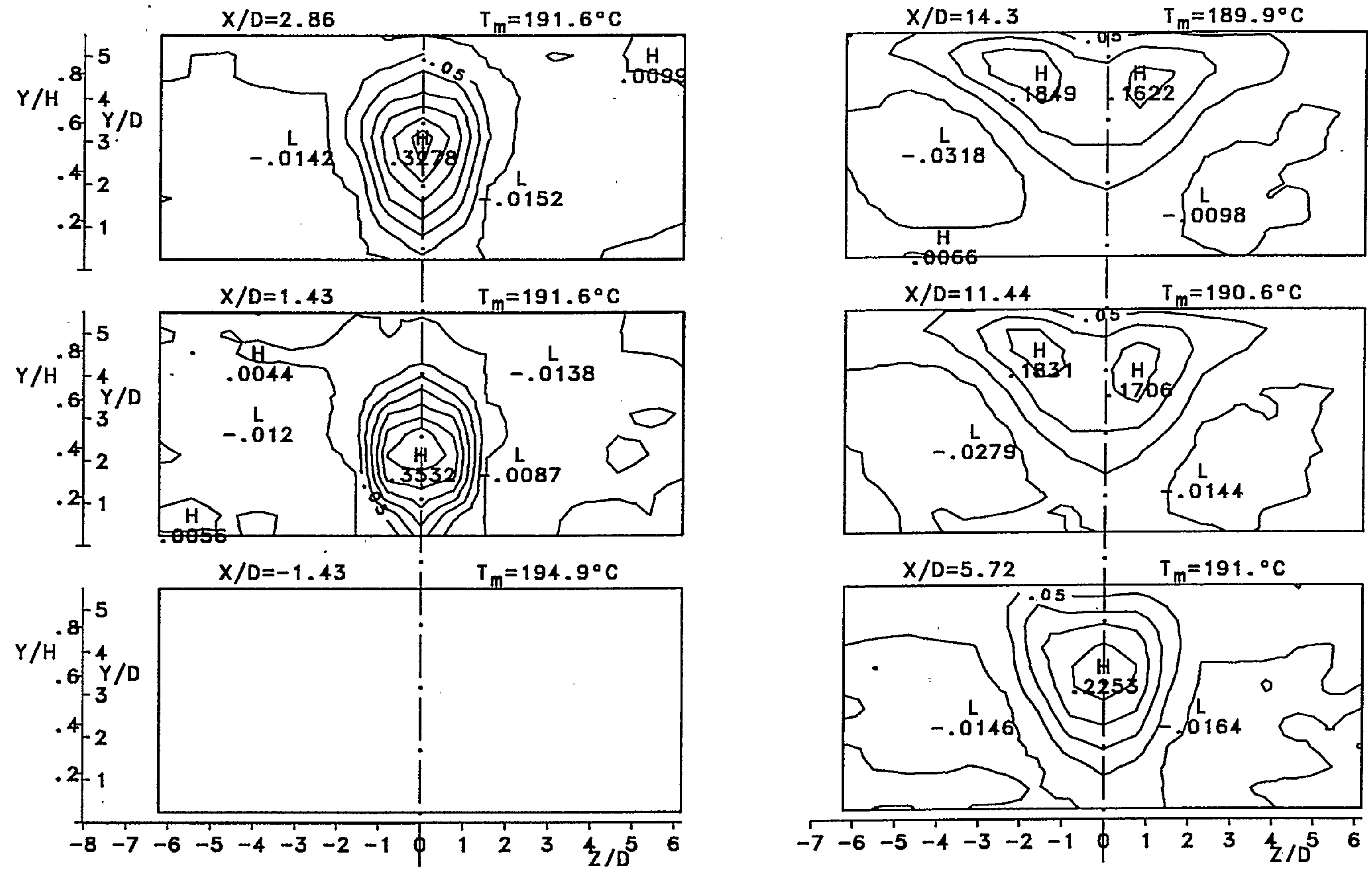

Fig.5.1.16 Θ Contour Maps for 90.W Power "drive" Case, Contour Interval 0.05.

St = .2223	ρ_∞ = .6869 kg/m^3	ρ_j = .9822 kg/m^3	T_j = 42.8 °C	D = 19.93 mm
$\dot{W}$ = 90. W	$\dot{M}_\infty$ = .3267 kg/s	$\dot{M}_j$ = .0056 kg/s	J = 3.171	f = 204 Hz
Ma = .0284	U_∞ = 12.28 m/s	V_j = 18.29 m/s	V_j/U_∞ = 1.509	
V_e/V_j = 1.302	Re_∞ = 57103.	Re_j = 18691.	$\dot{M}_j/\dot{M}_\infty$ = .0172	

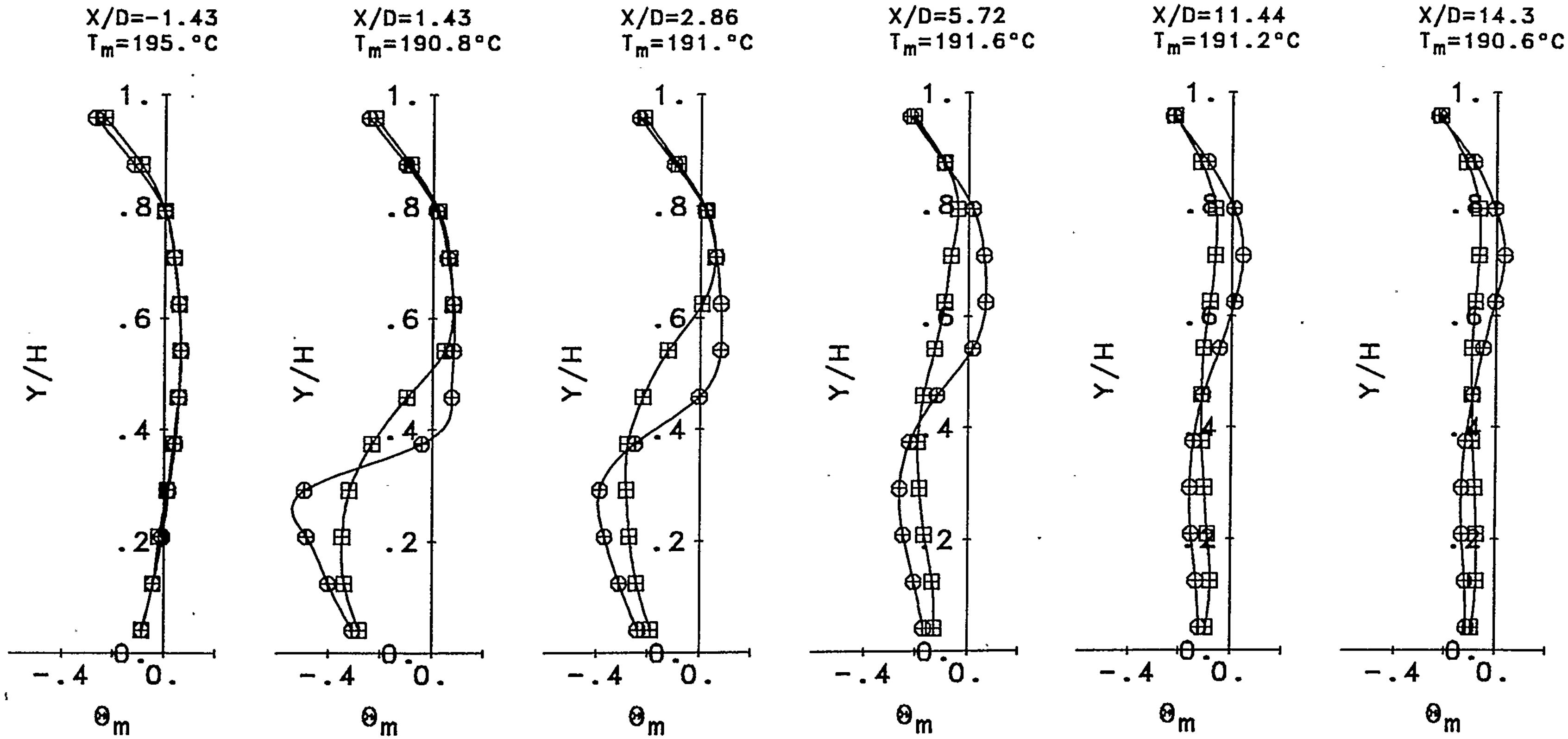

Fig.5.1.17 Centre-Plane Θ_m Mean Temperature Vertical Profiles; —⊕ "no-drive", —⊞ 15.W Power "drive" Case.

St = .224	ρ_∞ = .6951 kg/m^3	ρ_j = .9799 kg/m^3	T_j = 42.2 °C	D = 19.93 mm
$\dot{W}$ = 15. W	$\dot{M}_\infty$ = .3238 kg/s	$\dot{M}_j$ = .0055 kg/s	J = 3.177	f = 204 Hz
Ma = .028	U_∞ = 12.09 m/s	V_j = 18.15 m/s	V_j/U_∞ = 1.526	
V_e/V_j = .5383	Re_∞ = 56889.	Re_j = 18506.	$\dot{M}_j/\dot{M}_\infty$ = .0171	

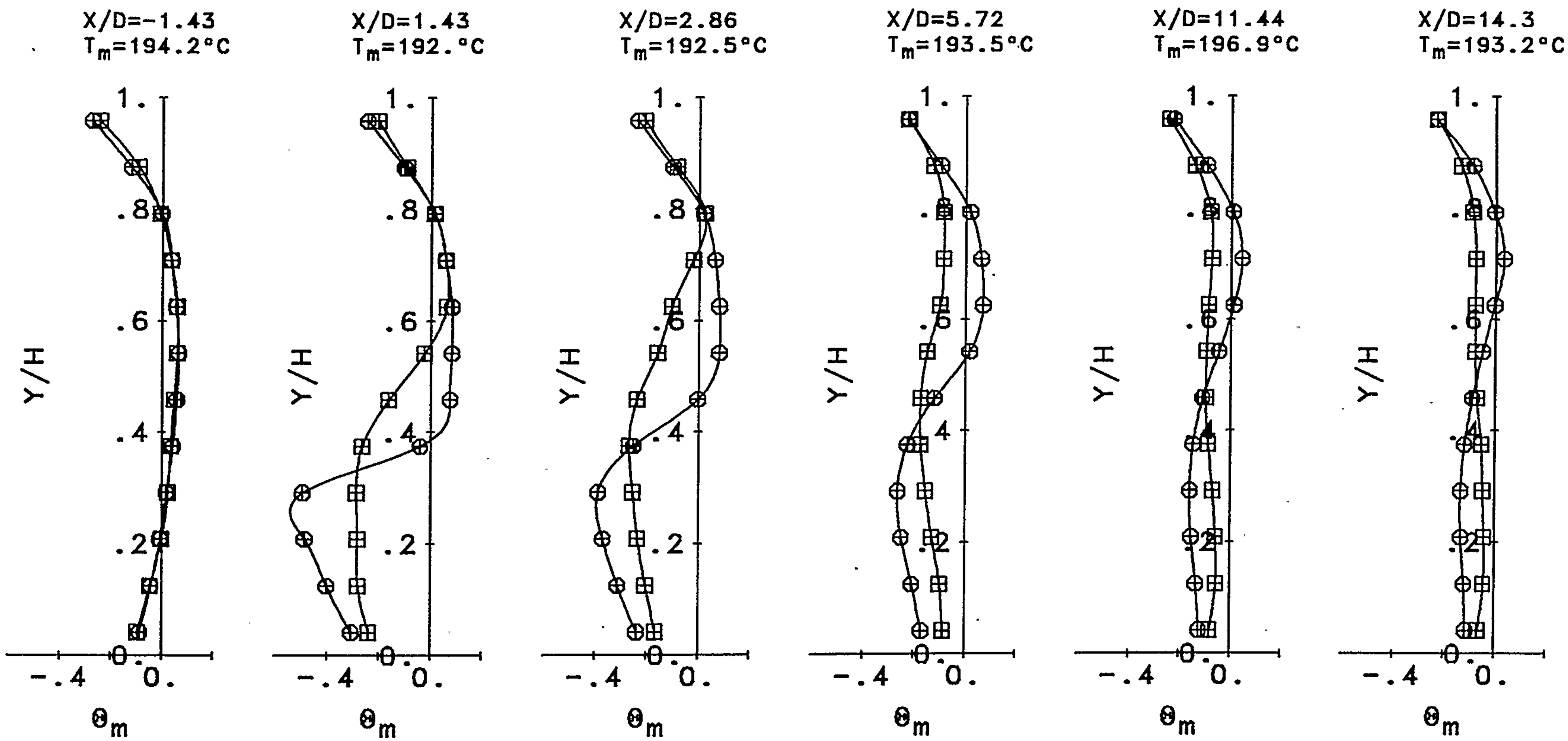

Fig.5.1.18 Centre-Plane Θ_m Mean Temperature Vertical Profiles;
—⊕ "no-drive", —⊞ 30.W Power "drive" Case.

St = .2295	ρ_∞ = .7396 kg/m^3	ρ_I = .9911 kg/m^3	T_I = 42.5 °C	D = 19.93 mm
$\dot{W}$ = 30. W	$\dot{M}_\infty$ = .3345 kg/s	$\dot{M}_I$ = .0055 kg/s	J = 2.991	f = 204 Hz
Ma = .0275	U_∞ = 11.86 m/s	V_I = 17.71 m/s	V_I/U_∞ = 1.541	
V_e/V_I = .7853	Re_∞ = 59351.	Re_I = 18265.	$\dot{M}_I/\dot{M}_\infty$ = .0164	

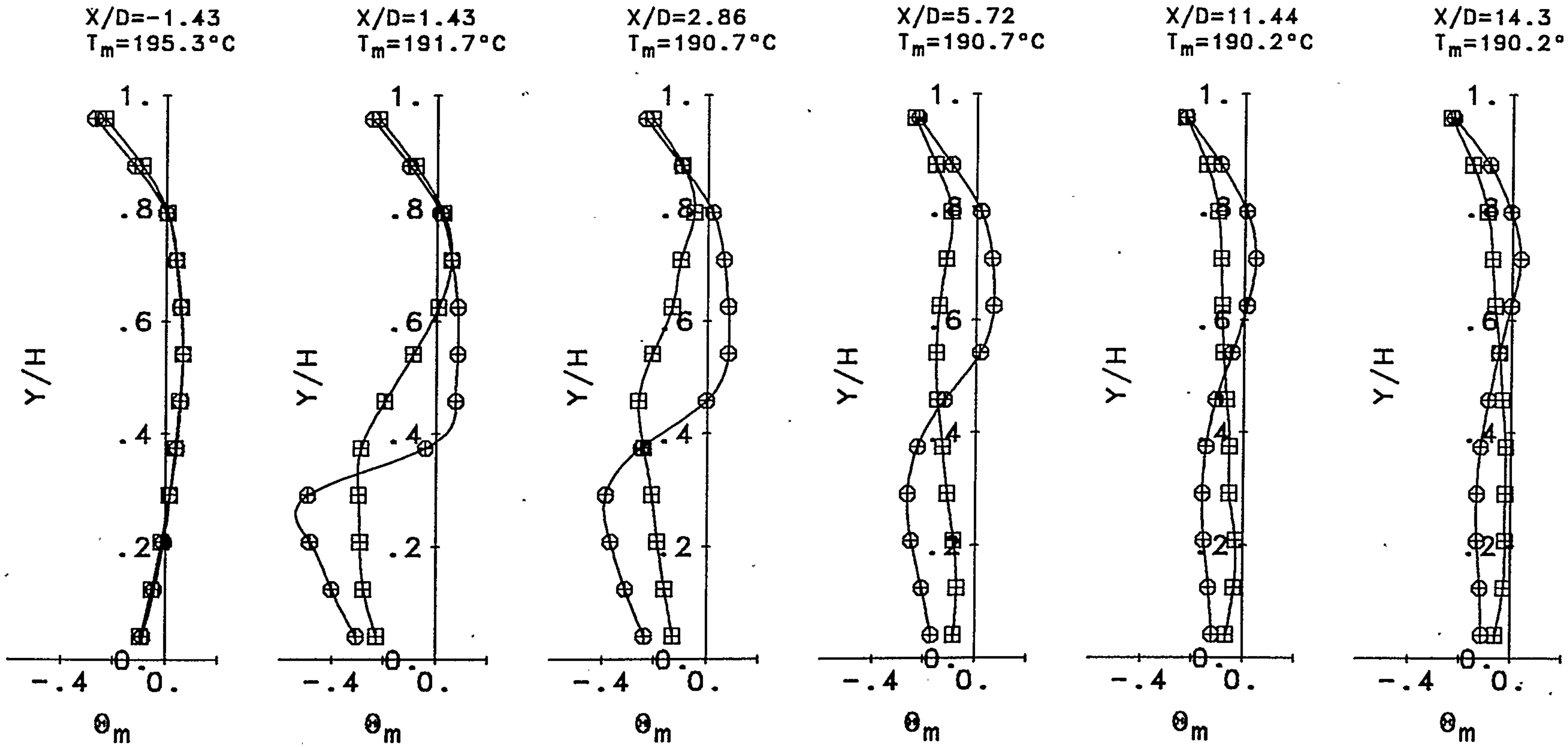

Fig.5.1.19 Centre-Plane Θ_m Mean Temperature Vertical Profiles; —⊕ "no-drive", —⊞ 45.W Power "drive" Case.

St = .2228	ρ_∞ = .6951 kg/m^3	ρ_j = .9799 kg/m^3	T_j = 42.5 °C	D = 19.93 mm
$\dot{W}$ = 45. W	$\dot{M}_\infty$ = .3284 kg/s	$\dot{M}_j$ = .0056 kg/s	J = 3.141	f = 204 Hz
Ma = .0283	U_∞ = 12.22 m/s	V_j = 18.25 m/s	V_j/U_∞ = 1.516	
V_e/V_j= .9253	Re_∞ = 57507.	Re_j = 18601.	$\dot{M}_j/\dot{M}_\infty$ = .017	

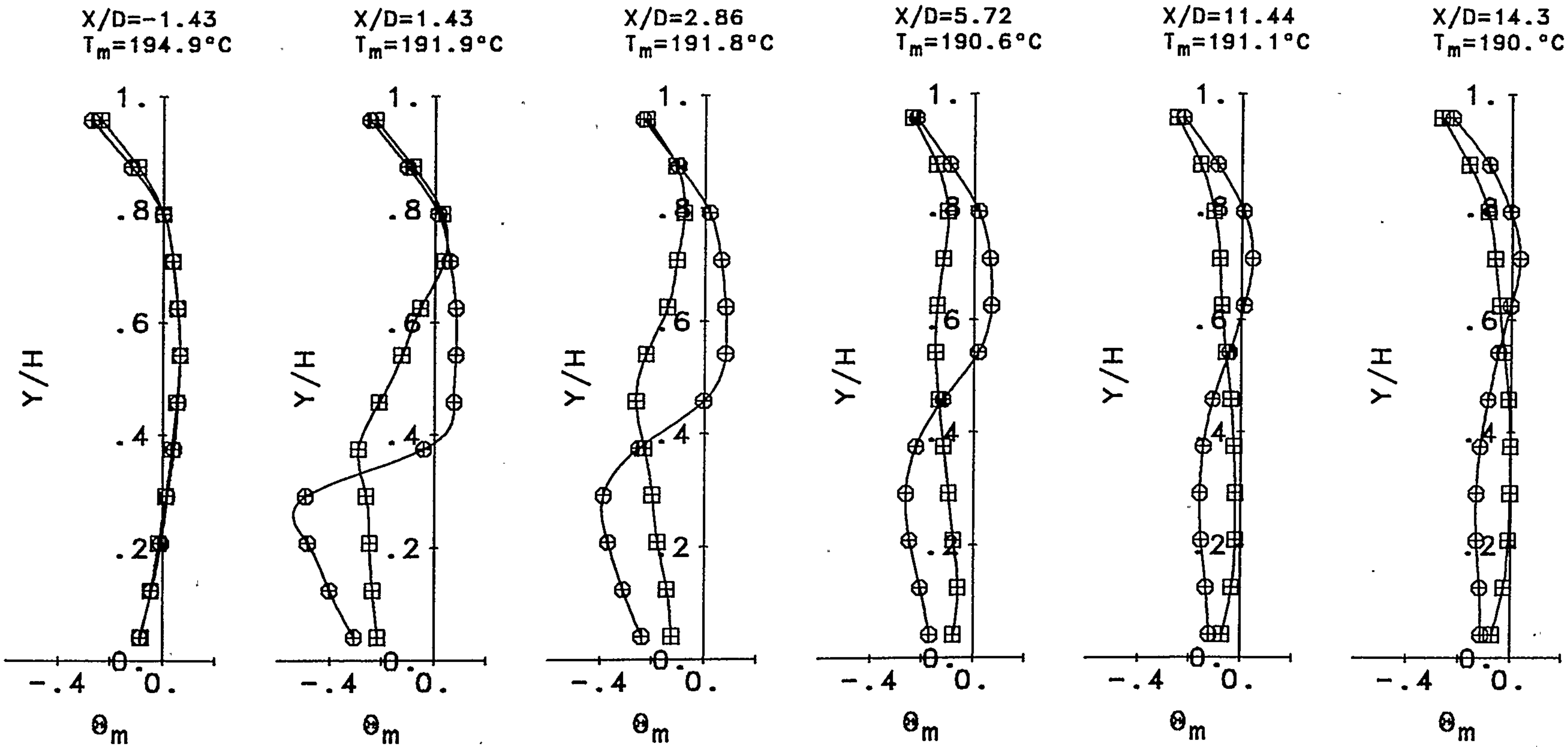

Fig.5.1.20 Centre-Plane Θ_m Mean Temperature Vertical Profiles;
—⊕ "no-drive", —⊞ 60.W Power "drive" Case.

St = .2213
$\dot{W}$ = 60. W
Ma = .0255
V_e/V_j = 1:055

ρ_∞ = .7776 kg/m^3
$\dot{M}_\infty$ = .3262 kg/s
U_∞ = 11.01 m/s
Re_∞ = 57928.

ρ_j = .9858 kg/m^3
$\dot{M}_j$ = .0056 kg/s
V_j = 18.37 m/s
Re_j = 18839.

T_j = 42.1 °C
J = 3.531
V_j/U_∞ = 1.718
$\dot{M}_j/\dot{M}_\infty$ = .0173

D = 19.93 mm
f = 204 Hz

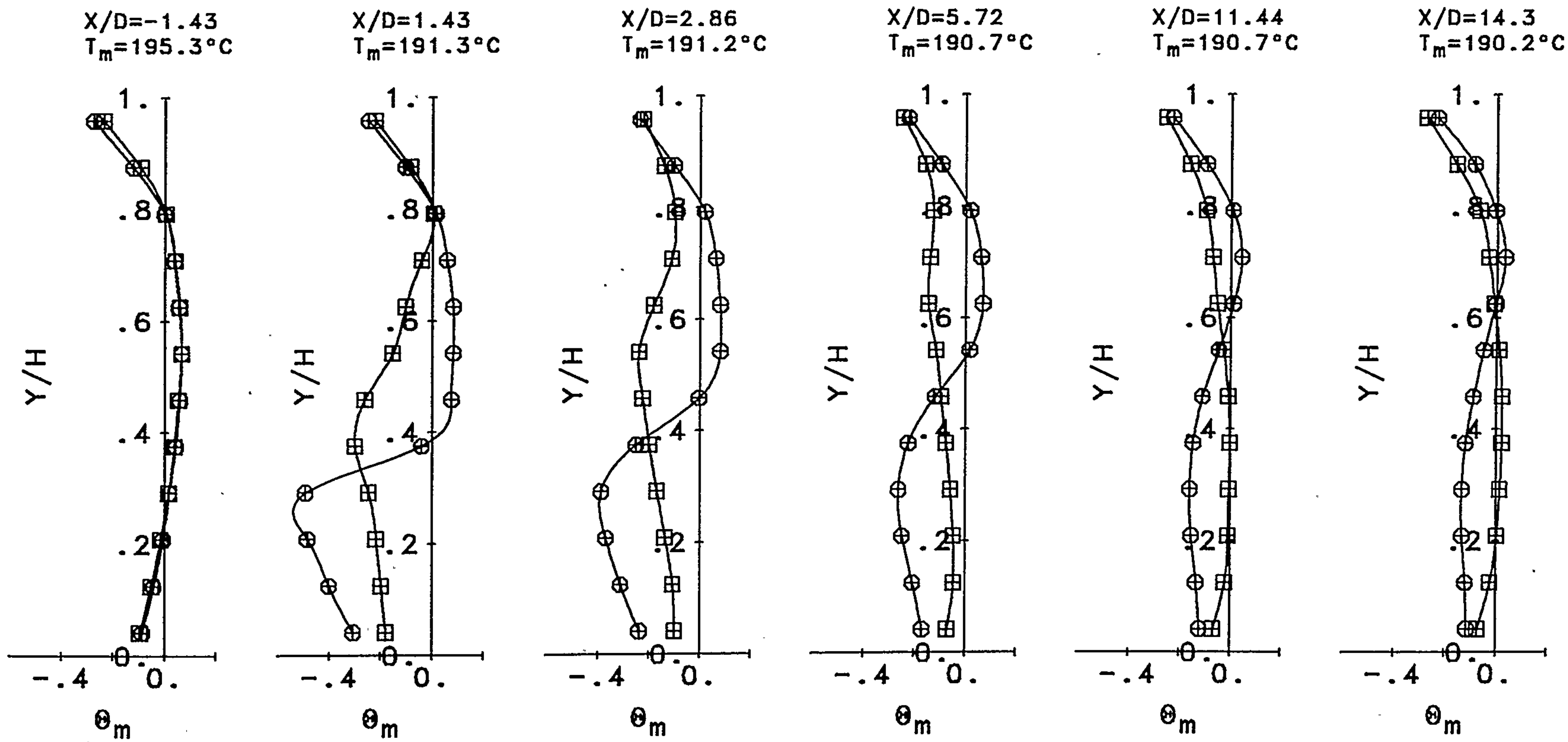

Fig.5.1.21 Centre-Plane Θ_m Mean Temperature Vertical Profiles;
—⊕ "no-drive", —⊞ 75.W Power "drive" Case.

St = .2194	ρ_∞ = .651 kg/m^3	ρ_j = .9838 kg/m^3	T_j = 41.5 °C	D = 19.93 mm
$\dot{W}$ = 75. W	$\dot{M}_\infty$ = .3274 kg/s	$\dot{M}_j$ = .0057 kg/s	J = 3.149	f = 204 Hz
Ma = .0297	U_∞ = 12.84 m/s	V_j = 18.53 m/s	V_j/U_∞ = 1.446	
V_e/V_j = 1.165	Re_∞ = 56557.	Re_j = 18967.	$\dot{M}_j/\dot{M}_\infty$ = .0174	

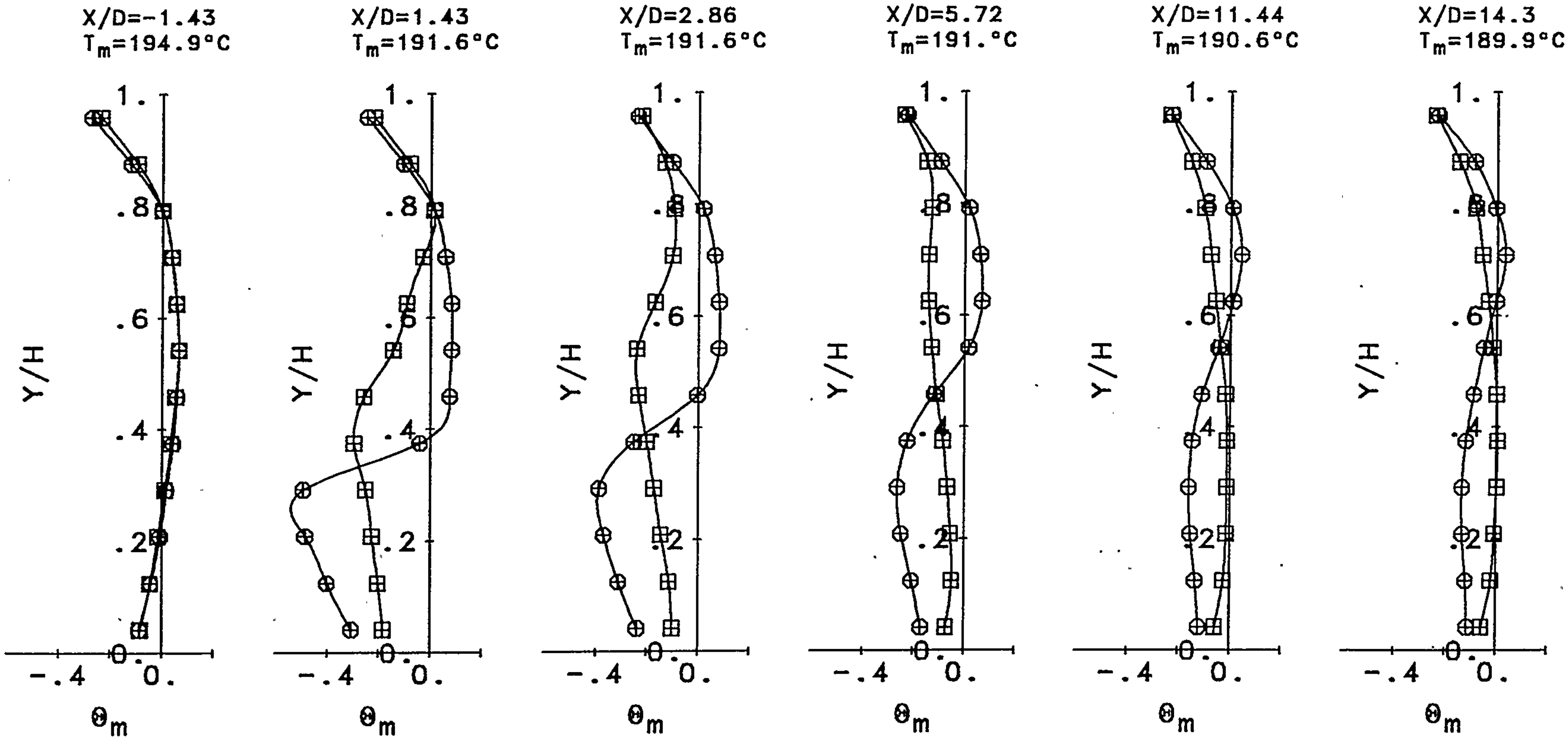

Fig.5.1.22 Centre-Plane Θ_m Mean Temperature Vertical Profiles;
—⊕ "no-drive", —⊞ 90.W Power "drive" Case.

St = .2223
$\dot{W}$ = 90. W
Ma = .0284
V_e/V_J = 1.302

ρ_∞ = .6869 kg/m^3
$\dot{M}_\infty$ = .3267 kg/s
U_∞ = 12.28 m/s
Re_∞ = 57103.

ρ_J = .9822 kg/m^3
$\dot{M}_J$ = .0056 kg/s
V_J = 18.29 m/s
Re_J = 18691.

T_J = 42.8 °C
J = 3.171
V_J/U_∞ = 1.509
$\dot{M}_J/\dot{M}_\infty$ = .0172

D = 19.93 mm
f = 204 Hz

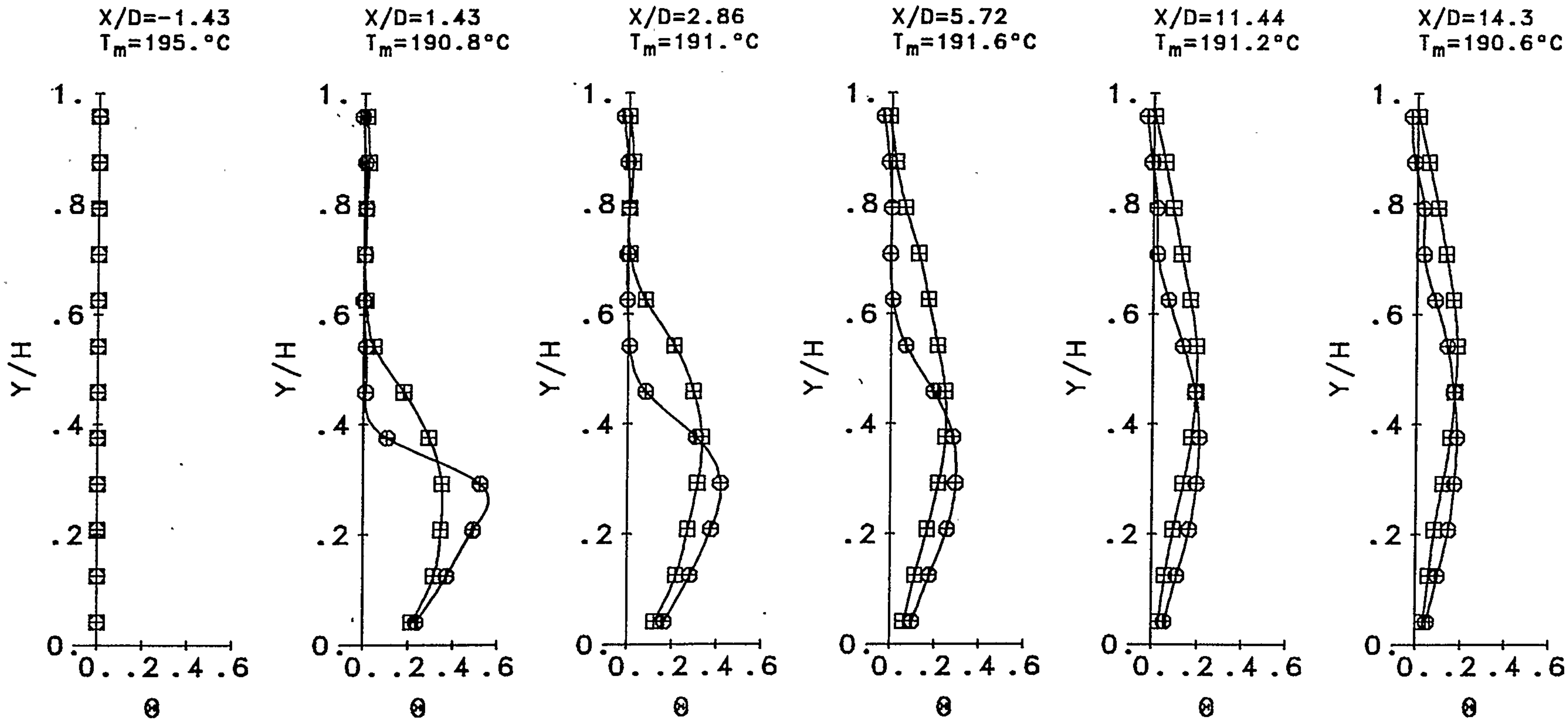

Fig.5.1.23 Centre-Plane Θ Vertical Profiles;
—⊕ "no-drive", —⊞ 15.W Power "drive" Case.

St = .224	ρ_∞ = .6951 kg/m^3	ρ_j = .9799 kg/m^3	T_j = 42.2 °C	D = 19.93 mm
$\dot{W}$ = 15. W	$\dot{M}_\infty$ = .3238 kg/s	$\dot{M}_j$ = .0055 kg/s	J = 3.177	f = 204 Hz
Ma = .028	U_∞ = 12.09 m/s	V_j = 18.15 m/s	V_j/U_∞ = 1.526	
V_e/V_j = .5383	Re_∞ = 56889.	Re_j = 18506.	$\dot{M}_j/\dot{M}_\infty$ = .0171	

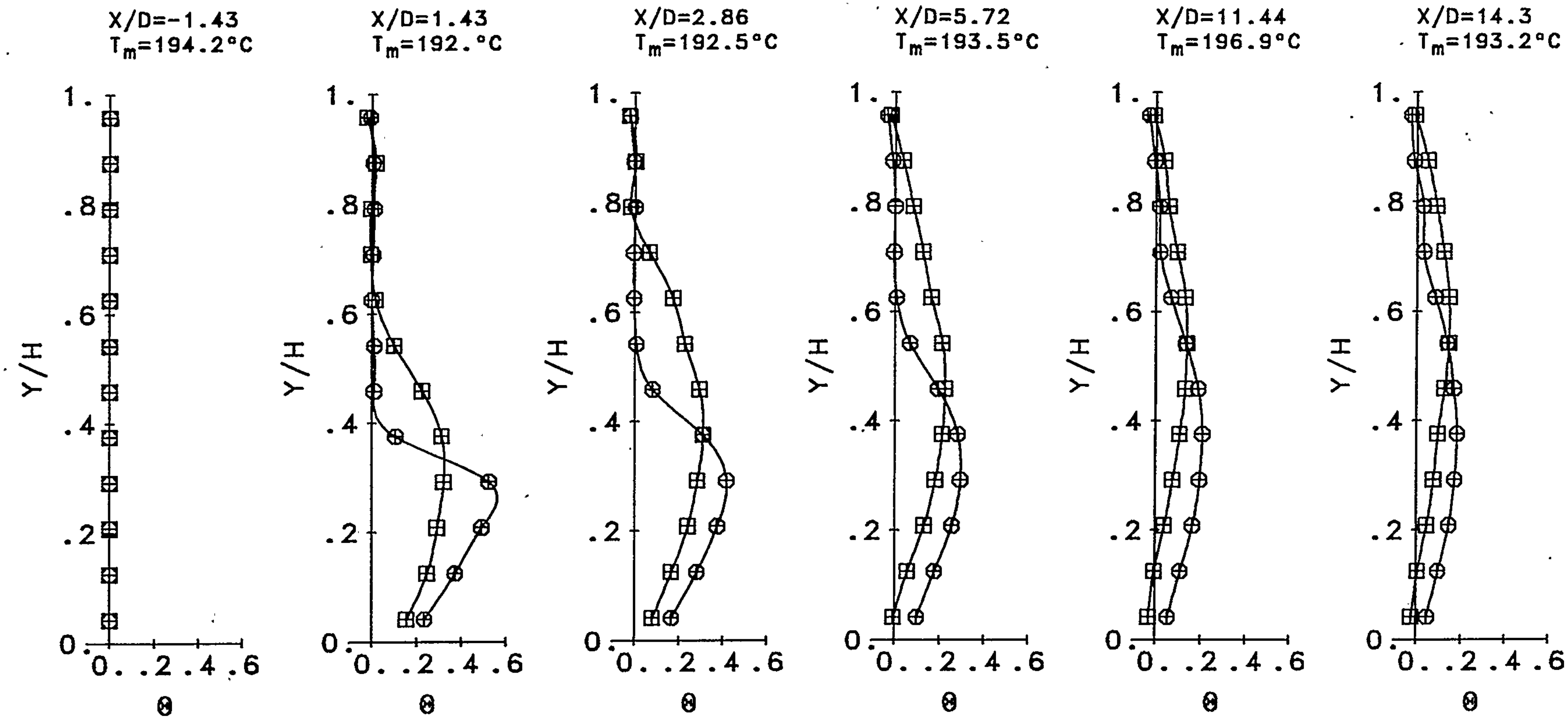

Fig.5.1.24 Centre-Plane Θ Vertical Profiles;
—⊕ "no-drive", —⊞ 30.W Power "drive" Case.

St = .2295	ρ_∞ = .7396 kg/m^3	ρ_I = .9911 kg/m^3	T_I = 42.5 °C	D = 19.93 mm
$\dot{W}$ = 30. W	$\dot{M}_\infty$ = .3345 kg/s	$\dot{M}_I$ = .0055 kg/s	J = 2.991	f = 204 Hz
Ma = .0275	U_∞ = 11.86 m/s	V_I = 17.71 m/s	V_I/U_∞ = 1.541	
V_e/V_I = .7853	Re_∞ = 59351.	Re_I = 18265.	$\dot{M}_I/\dot{M}_\infty$ = .0164	

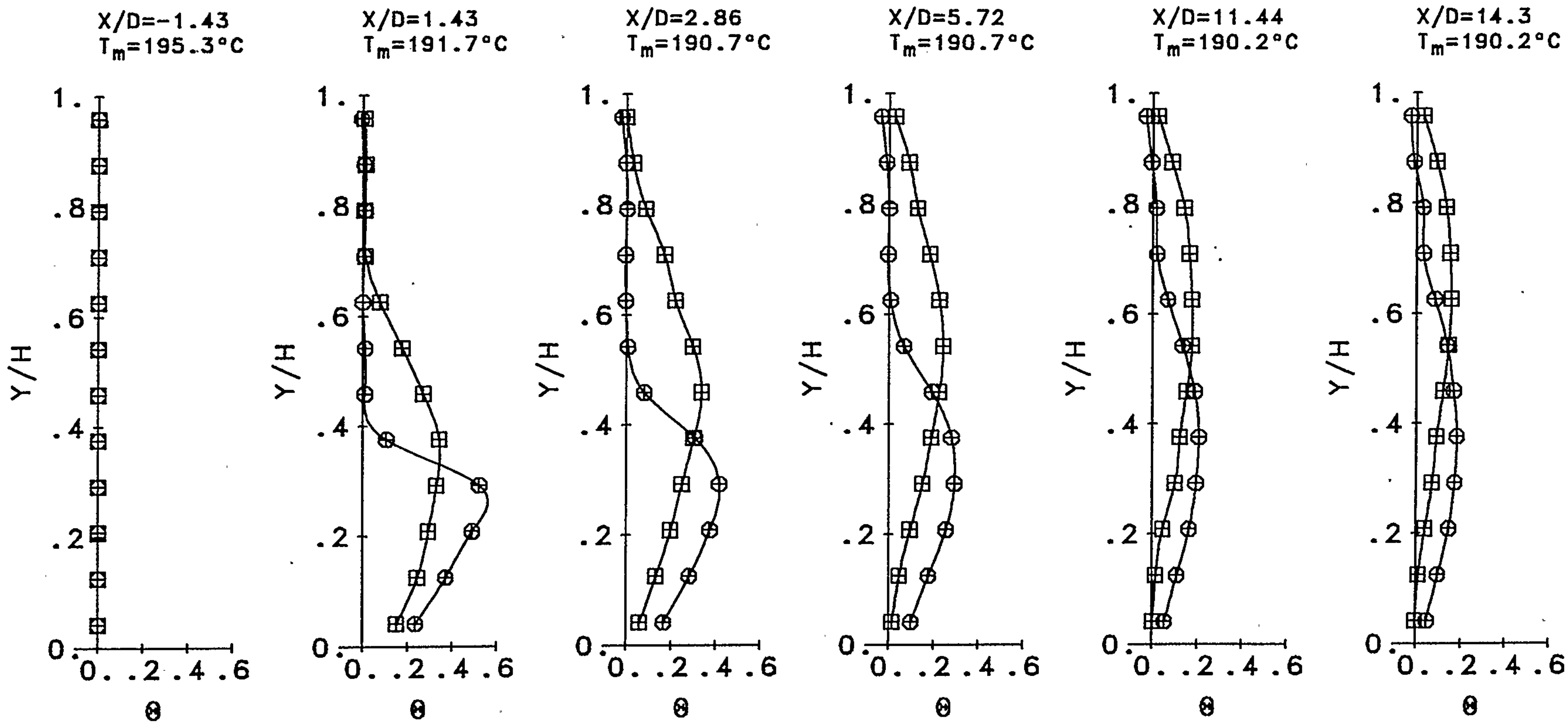

Fig.5.1.25 Centre-Plane θ Vertical Profiles;
—⊕ "no-drive", —⊞ 45.W Power "drive" Case.

St = .2228	ρ_∞ = .6951 kg/m^3	ρ_j = .9799 kg/m^3	T_j = 42.5 °C	D = 19.93 mm
$\dot{W}$ = 45. W	$\dot{M}_\infty$ = .3284 kg/s	$\dot{M}_j$ = .0056 kg/s	J = 3.141	f = 204 Hz
Ma = .0283	U_∞ = 12.22 m/s	V_j = 18.25 m/s	V_j/U_∞ = 1.516	
V_e/V_j = .9253	Re_∞ = 57507.	Re_j = 18601.	$\dot{M}_j/\dot{M}_\infty$ = .017	

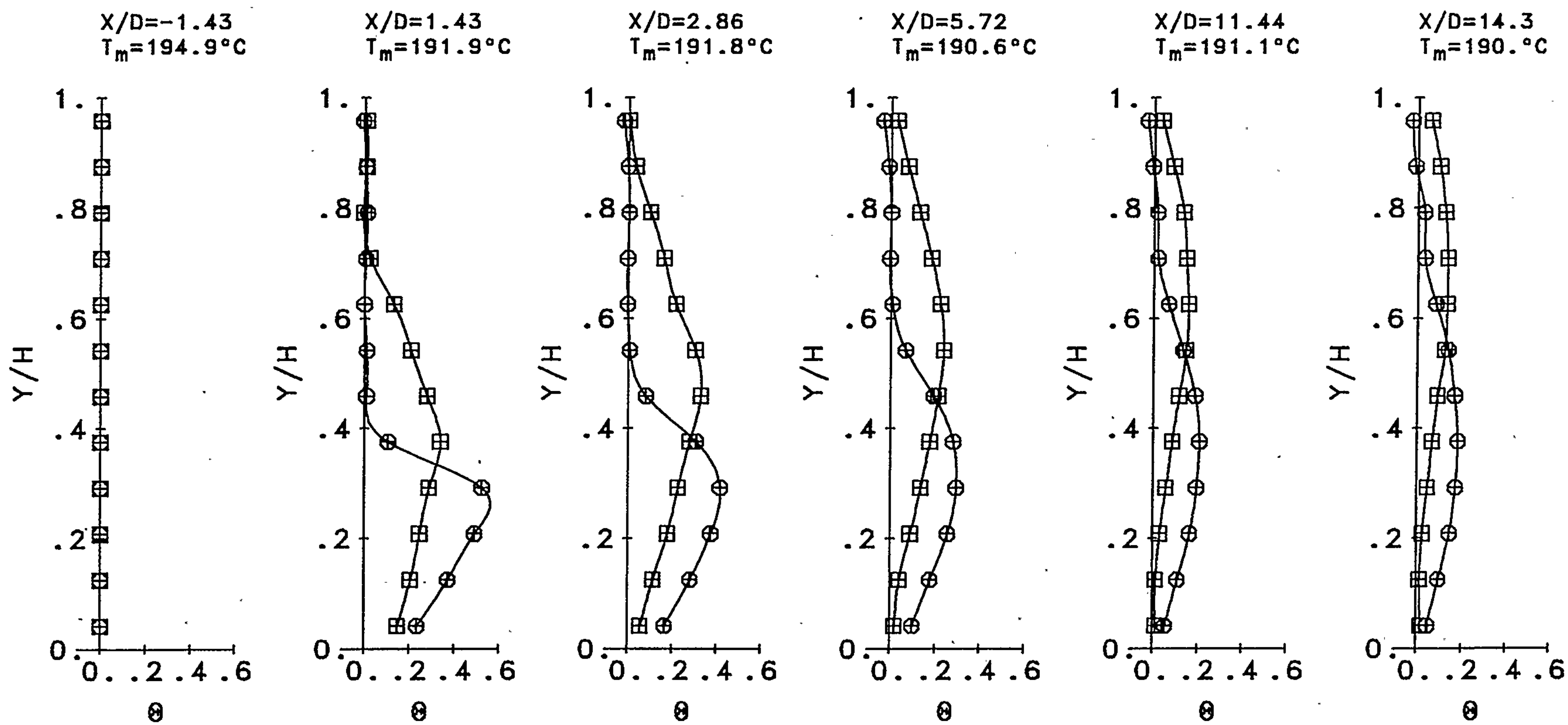

Fig.5.1.26 Centre-Plane θ Vertical Profiles;
—⊕ "no-drive", —⊞ 60.W Power "drive" Case.

St = .2213	ρ_∞ = .7776 kg/m^3	ρ_j = .9858 kg/m^3	T_j = 42.1 °C	D = 19.93 mm
$\dot{W}$ = 60. W	$\dot{M}_\infty$ = .3262 kg/s	$\dot{M}_j$ = .0056 kg/s	J = 3.531	f = 204 Hz
Ma = .0255	U_∞ = 11.01 m/s	V_j = 18.37 m/s	V_j/U_∞ = 1.718	
V_e/V_j = 1.055	Re_∞ = 57928.	Re_j = 18839.	$\dot{M}_j/\dot{M}_\infty$ = .0173	

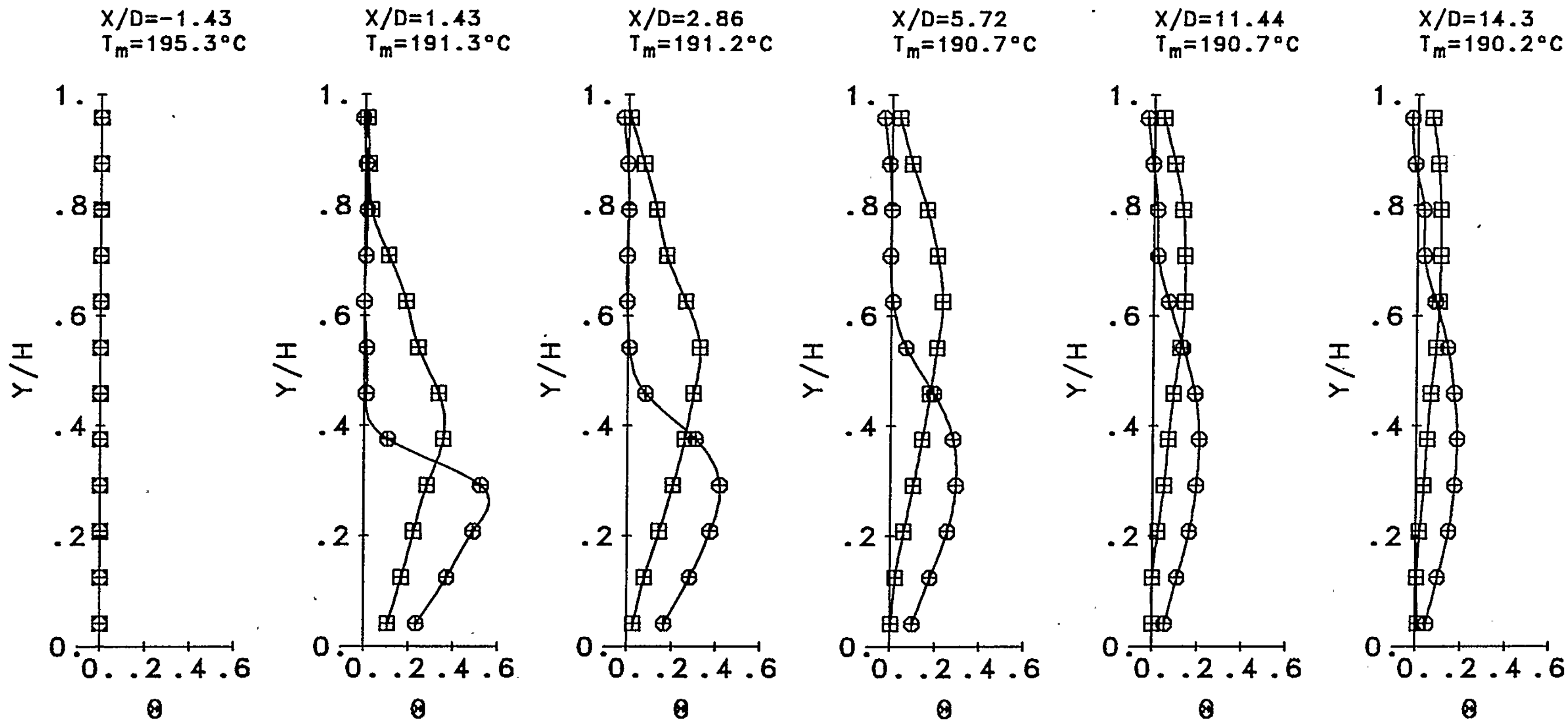

Fig.5.1.27 Centre-Plane θ Vertical Profiles;
—⊕ "no-drive", —⊞ 75.W Power "drive" Case.

St = .2194	ρ_∞ = .651 kg/m^3	ρ_j = .9838 kg/m^3	T_j = 41.5 °C	D = 19.93 mm
$\dot{W}$ = 75. W	$\dot{M}_\infty$ = .3274 kg/s	$\dot{M}_j$ = .0057 kg/s	J = 3.149	f = 204 Hz
Ma = .0297	U_∞ = 12.84 m/s	V_j = 18.53 m/s	V_j/U_∞ = 1.446	
V_e/V_j = 1.165	Re_∞ = 56557.	Re_j = 18967.	$\dot{M}_j/\dot{M}_\infty$ = .0174	

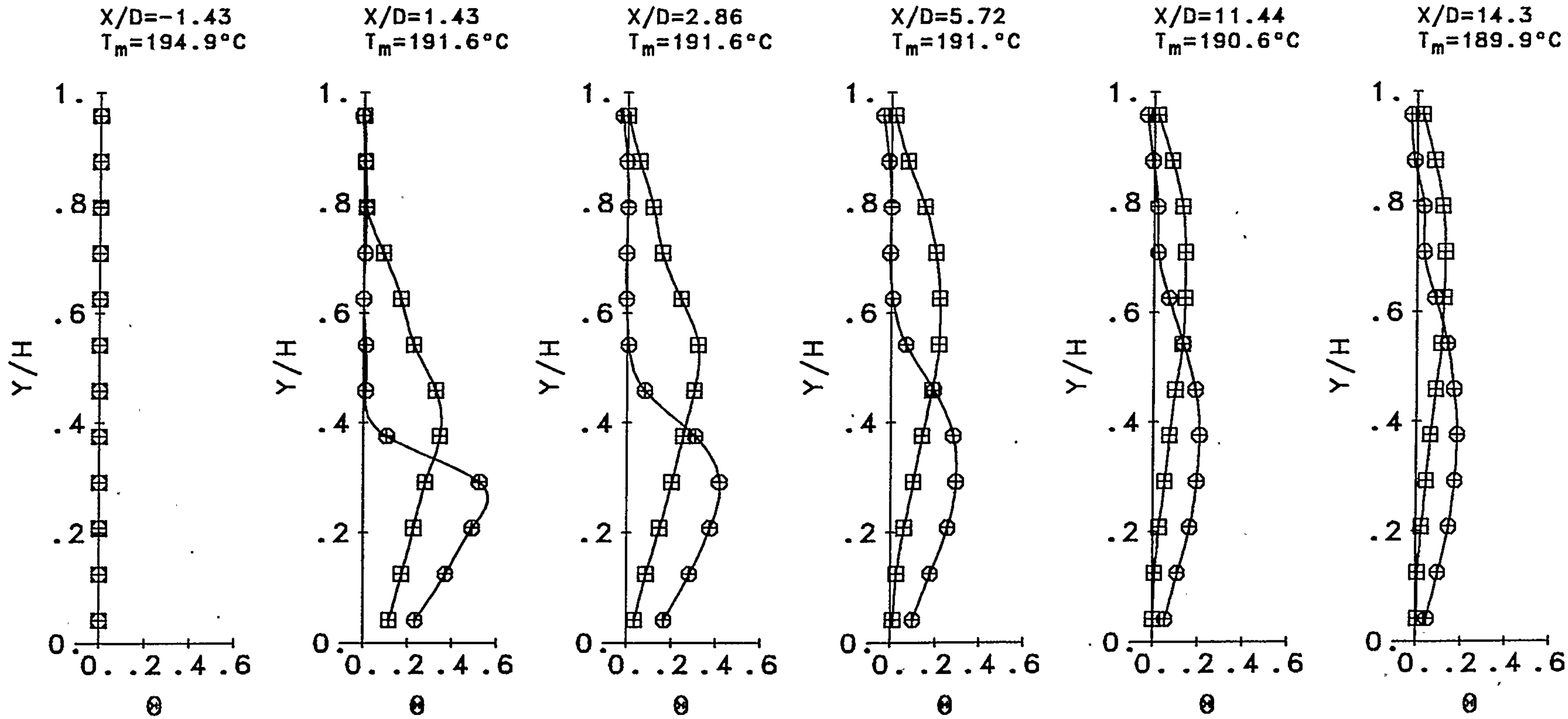

Fig.5.1.28 Centre-Plane θ Vertical Profiles;
—⊕ "no-drive", —⊞ 90.W Power "drive" Case.

St = .2223	ρ_∞ = .6869 kg/m^3	ρ_j = .9822 kg/m^3	T_j = 42.8 °C	D = 19.93 mm
$\dot{W}$ = 90. W	$\dot{M}_\infty$ = .3267 kg/s	$\dot{M}_j$ = .0056 kg/s	J = 3.171	f = 204 Hz
Ma = .0284	U_∞ = 12.28 m/s	V_j = 18.29 m/s	V_j/U_∞ = 1.509	
V_e/V_j = 1.302	Re_∞ = 57103.	Re_j = 18691.	$\dot{M}_j/\dot{M}_\infty$ = .0172	

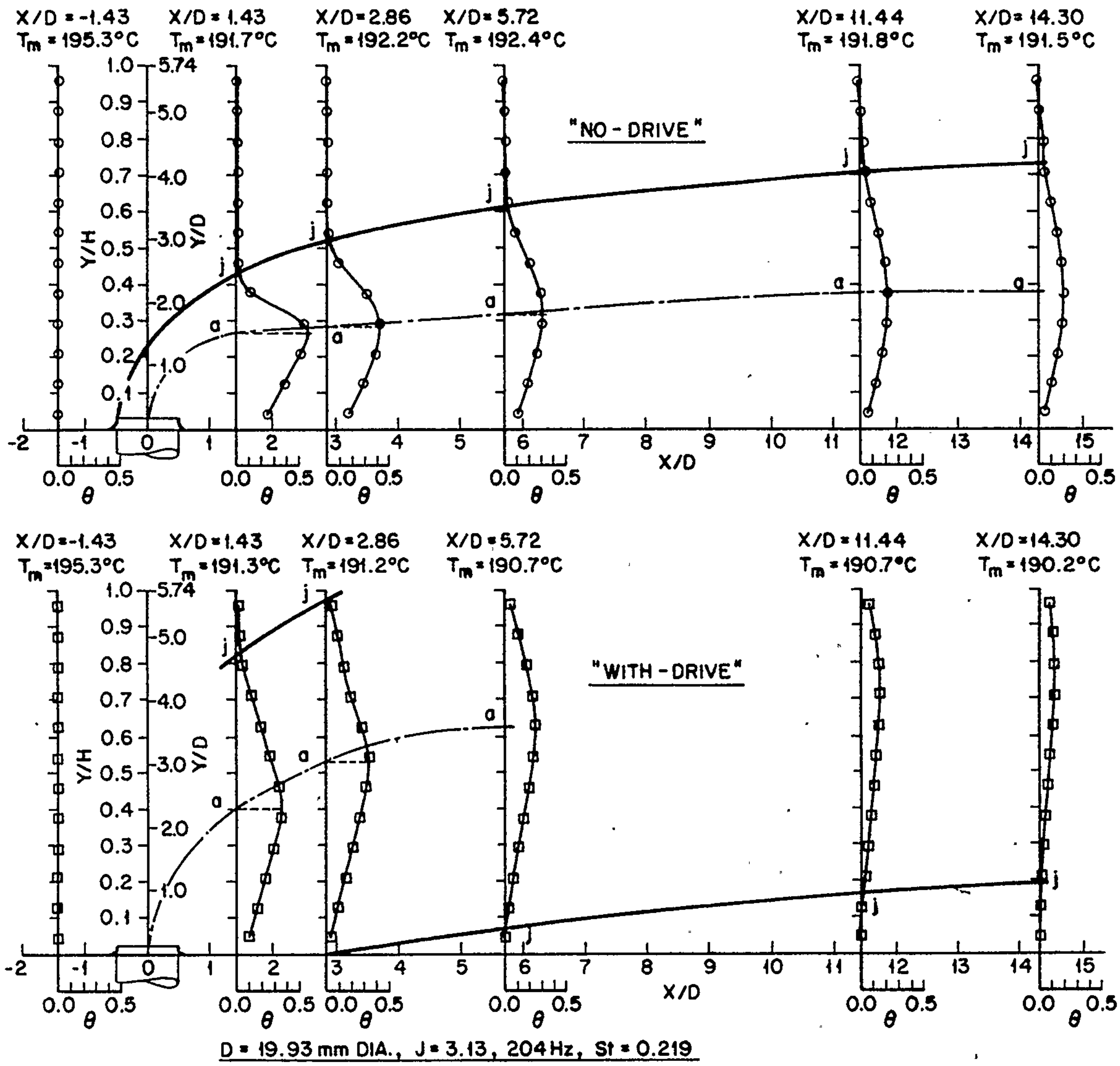

Fig. 5.1.29 Centre-Plane Jet-Crossflow Structure Corresponding to the θ Profiles of Figs. 5.1.4 and 5.1.15, Zero and 75W Powers, V_e/V_j=1.165.

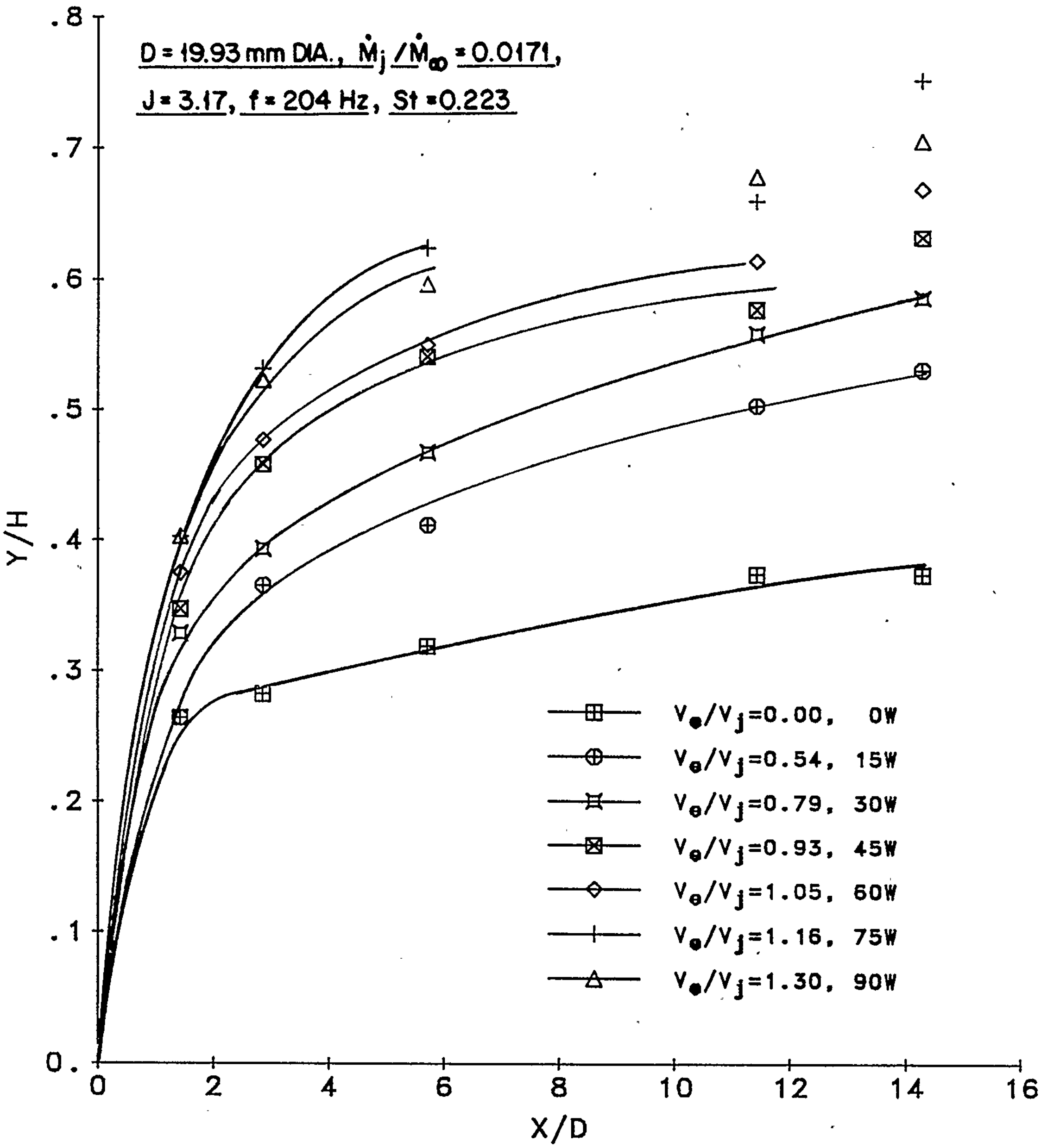

Fig. 5.1.30 Centre-Plane Jet Trajectories at Different Excitation Conditions, for 0-90W Powers. Average Conditions, V_j=18.2 m/s, V_j/U_∞=1.53, T_j=42.2°C, $\overline{T}_\infty$=195.0°C, ρ_j=0.985 kg/m^3, ρ_∞=0.700 kg/m^3, Re_j=18701, Re_∞=57639.

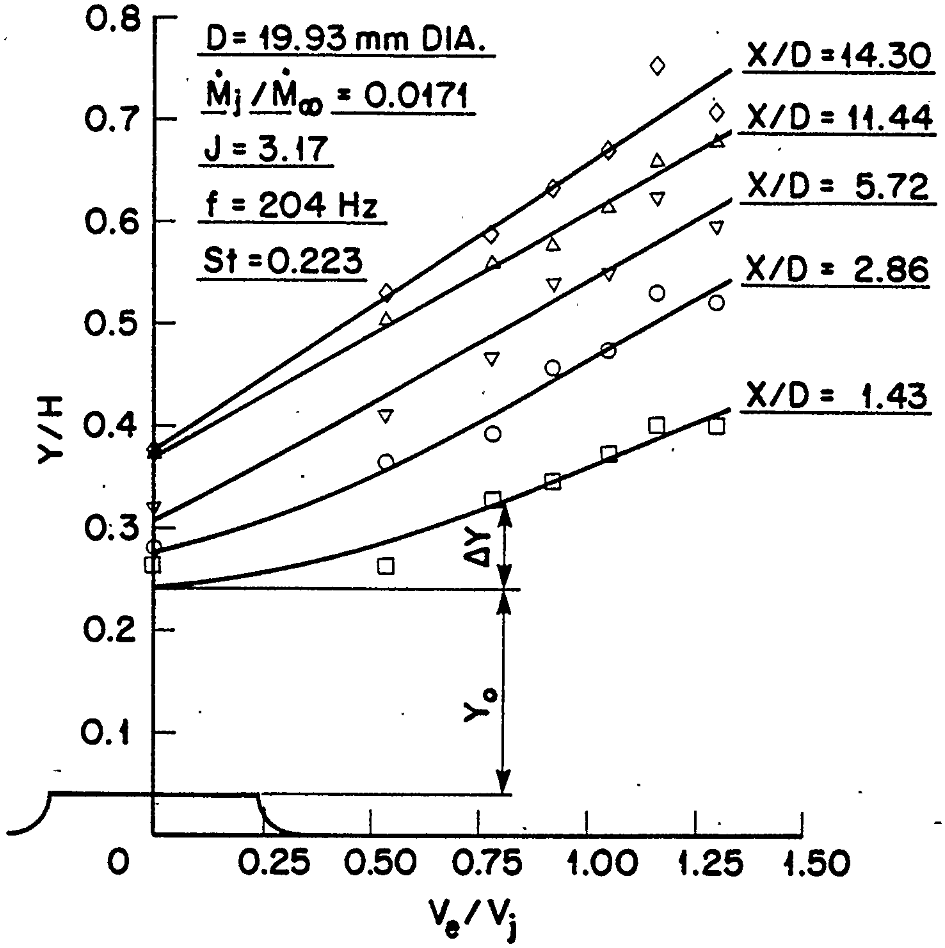

Fig. 5.1.31 Centre-Plane Jet Penetration Versus Relative Pulsation Strength, for 0-90W Powers. See Fig. 5.1.30 for Other Data.

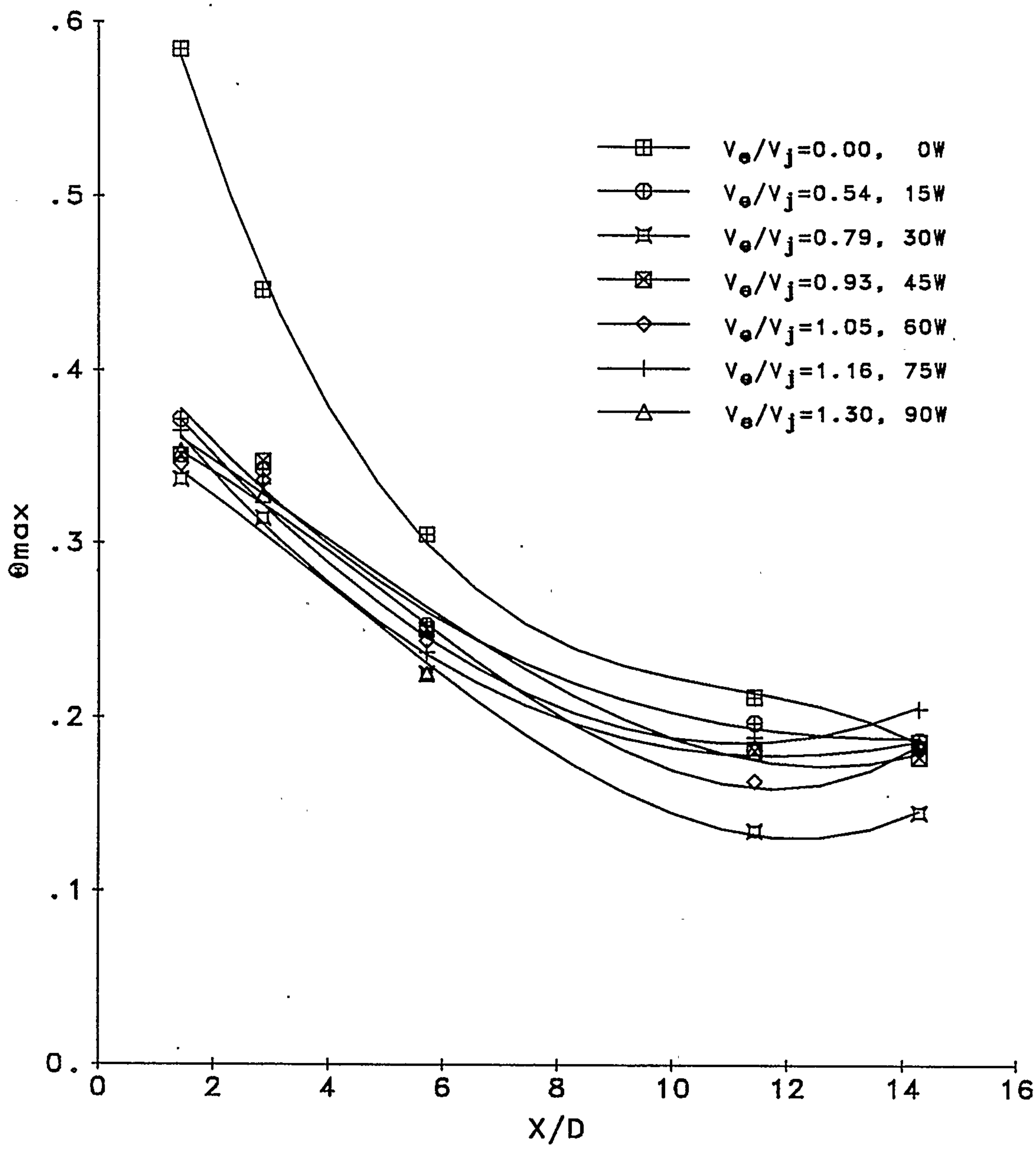

Fig.5.1.32 Θmax Parameter Versus Down-Stream Distance, See Fig. 5.1.30 for Other Data.

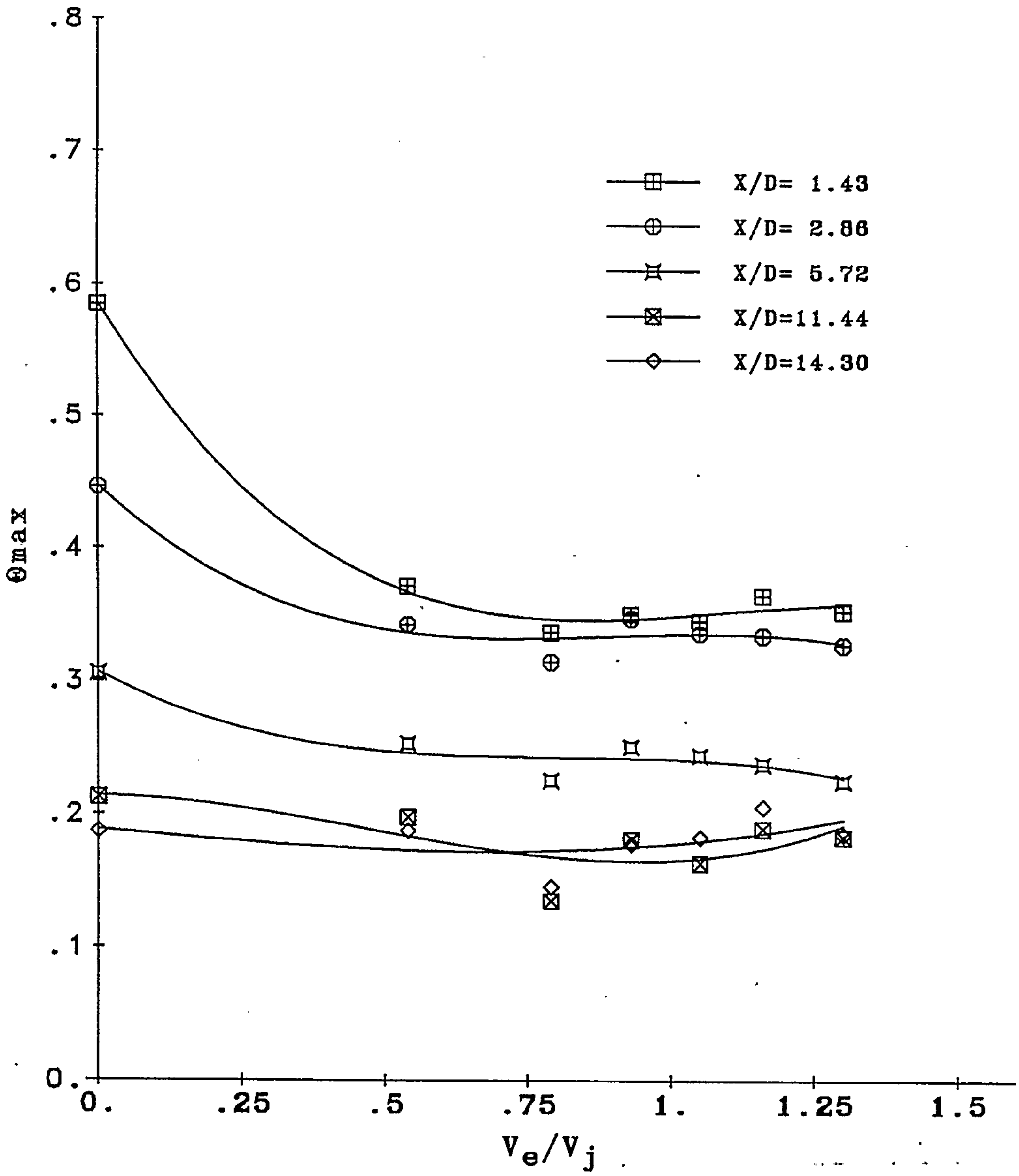

Fig. 5.1.33 The Influance of Pulsation Strength on Θmax,
See Fig. 5.1.30 for Other Data.

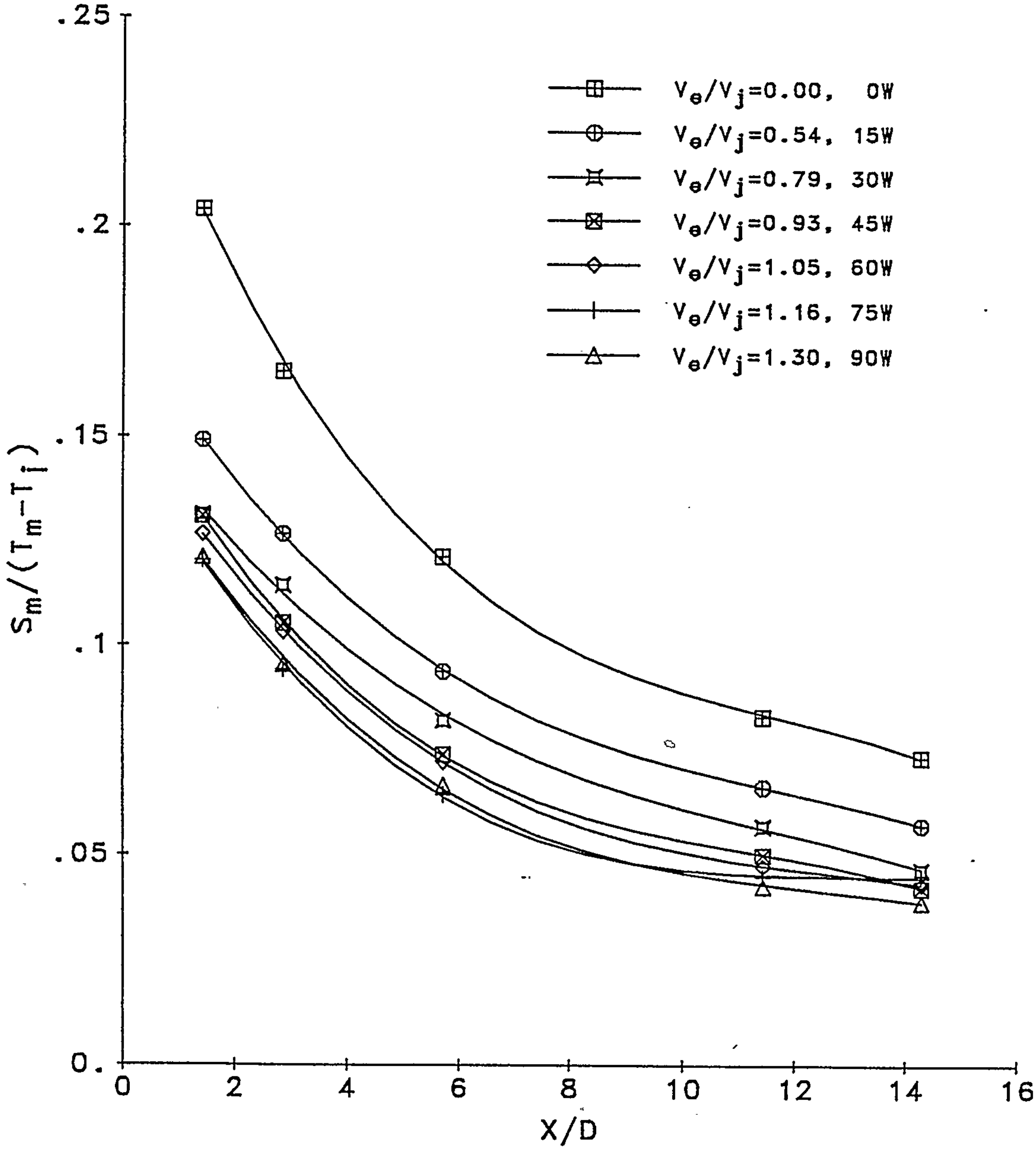

Fig. 5.1.34 Relative Mixing Effectiveness Versus Down-Stream Distance, See Fig. 5.1.30 for Other Data.

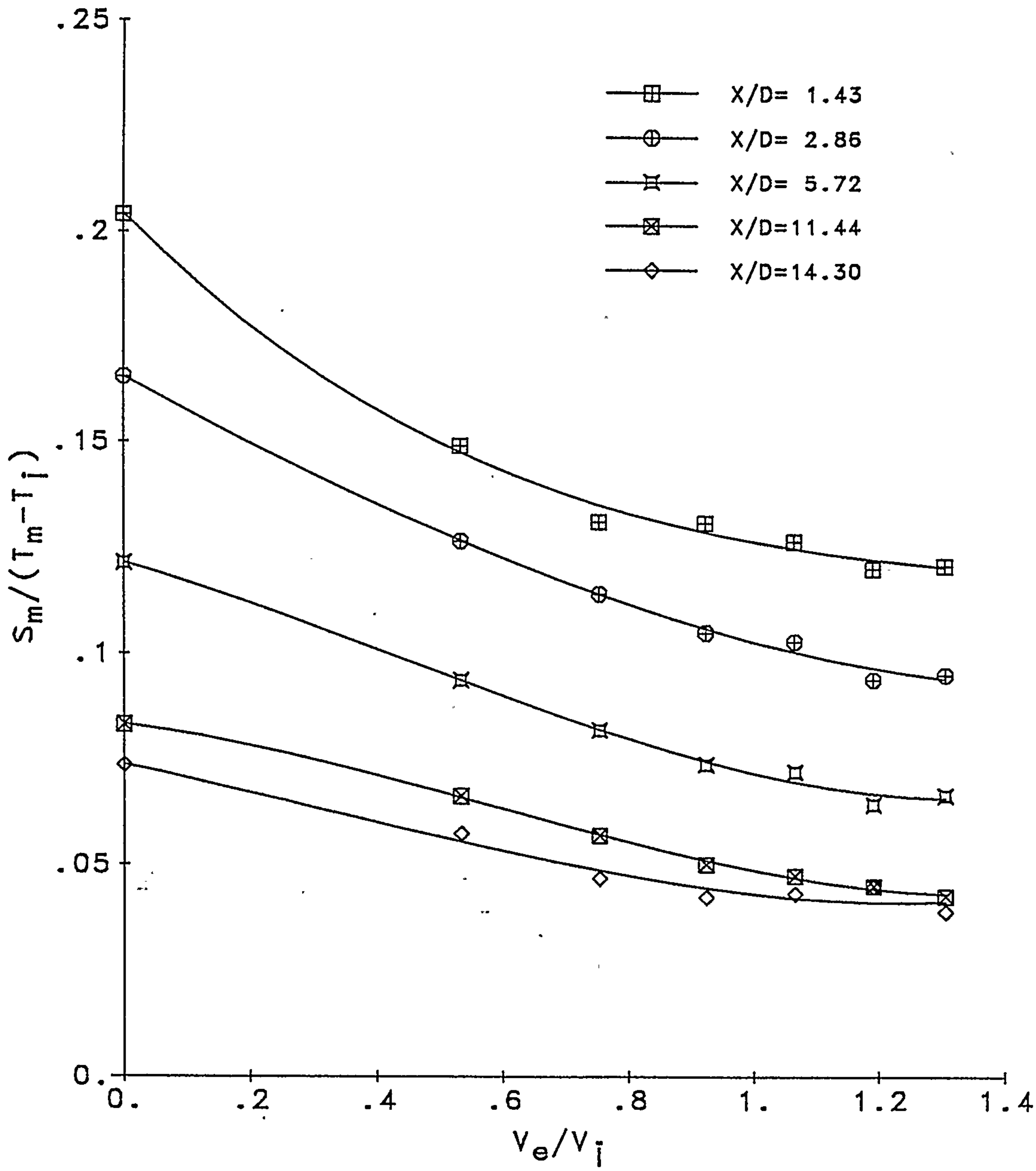

Fig. 5.1.35 Relative Mixing Effectiveness Versus Pulsation Strength, See Fig. 5.1.30 for Other Data.

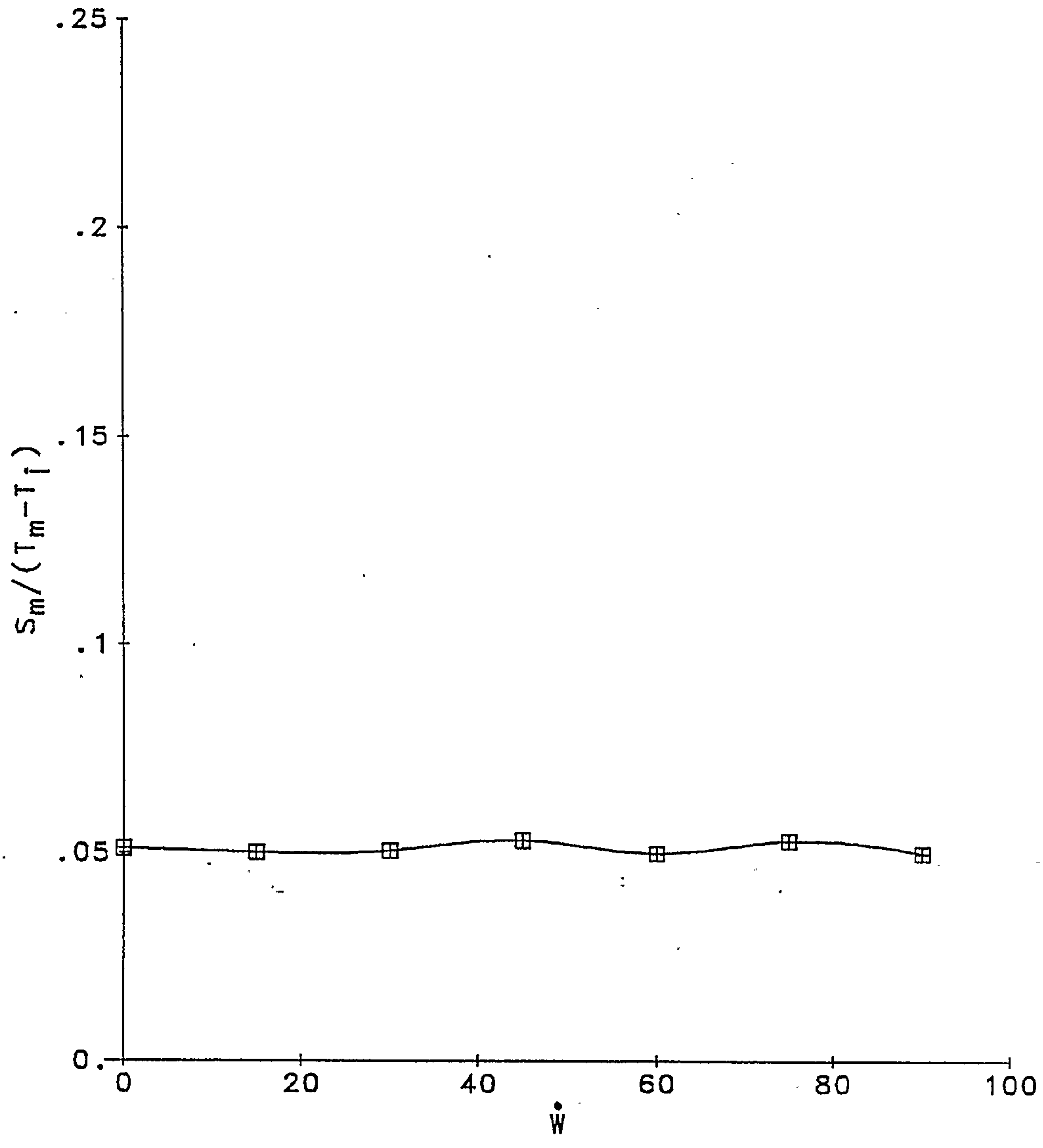

Fig. 5.1.36 The Relative Mixing Effectiveness in the Reference Plane ("noise") Versus Driving Power, See Fig. 5.1.30 for Other Data.

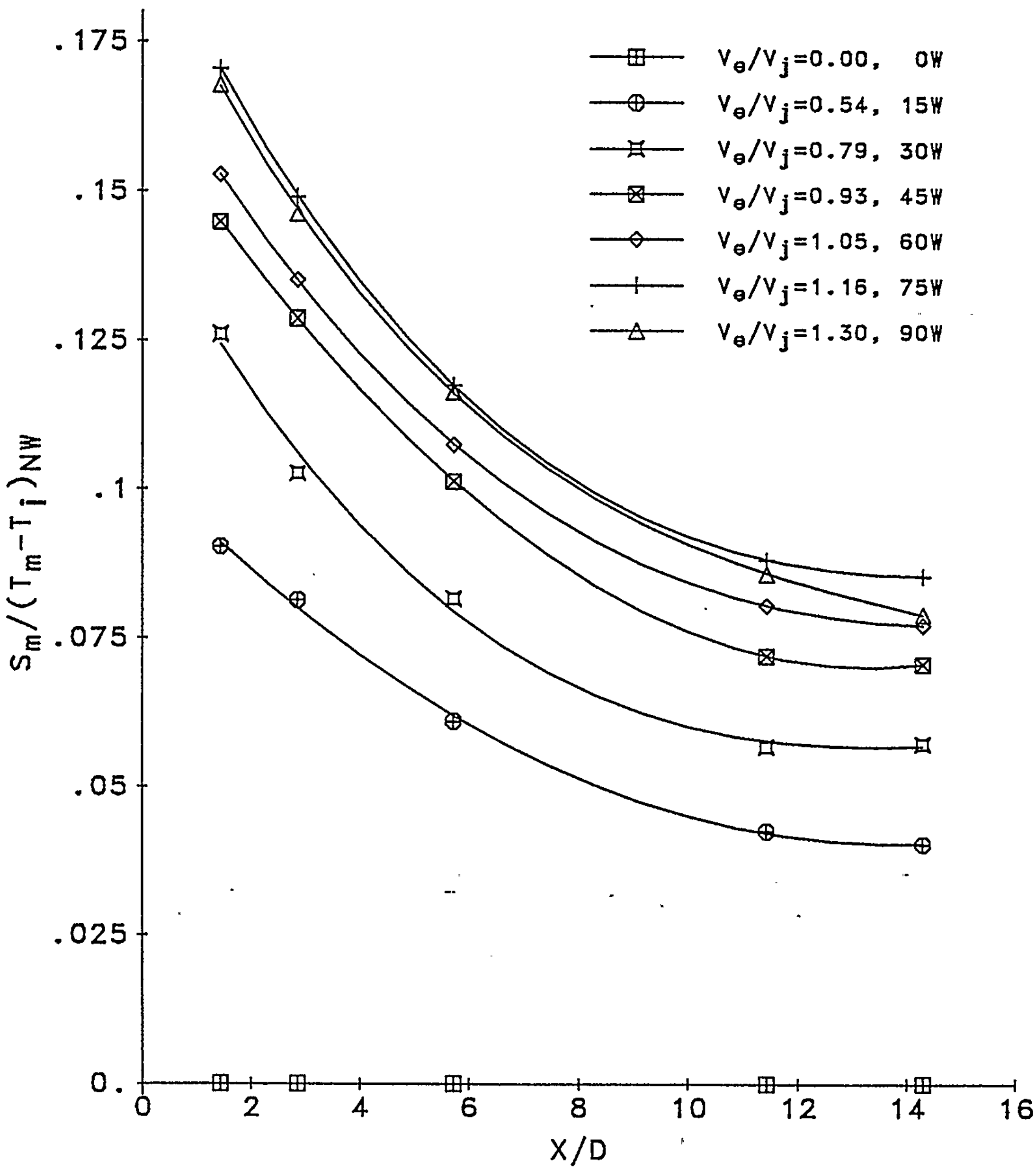

Fig. 5.1.37 The Net Variation of Relative Mixing Effectiveness Versus Down-Stream Distance, See Fig. 5.1.30 for Other Data.

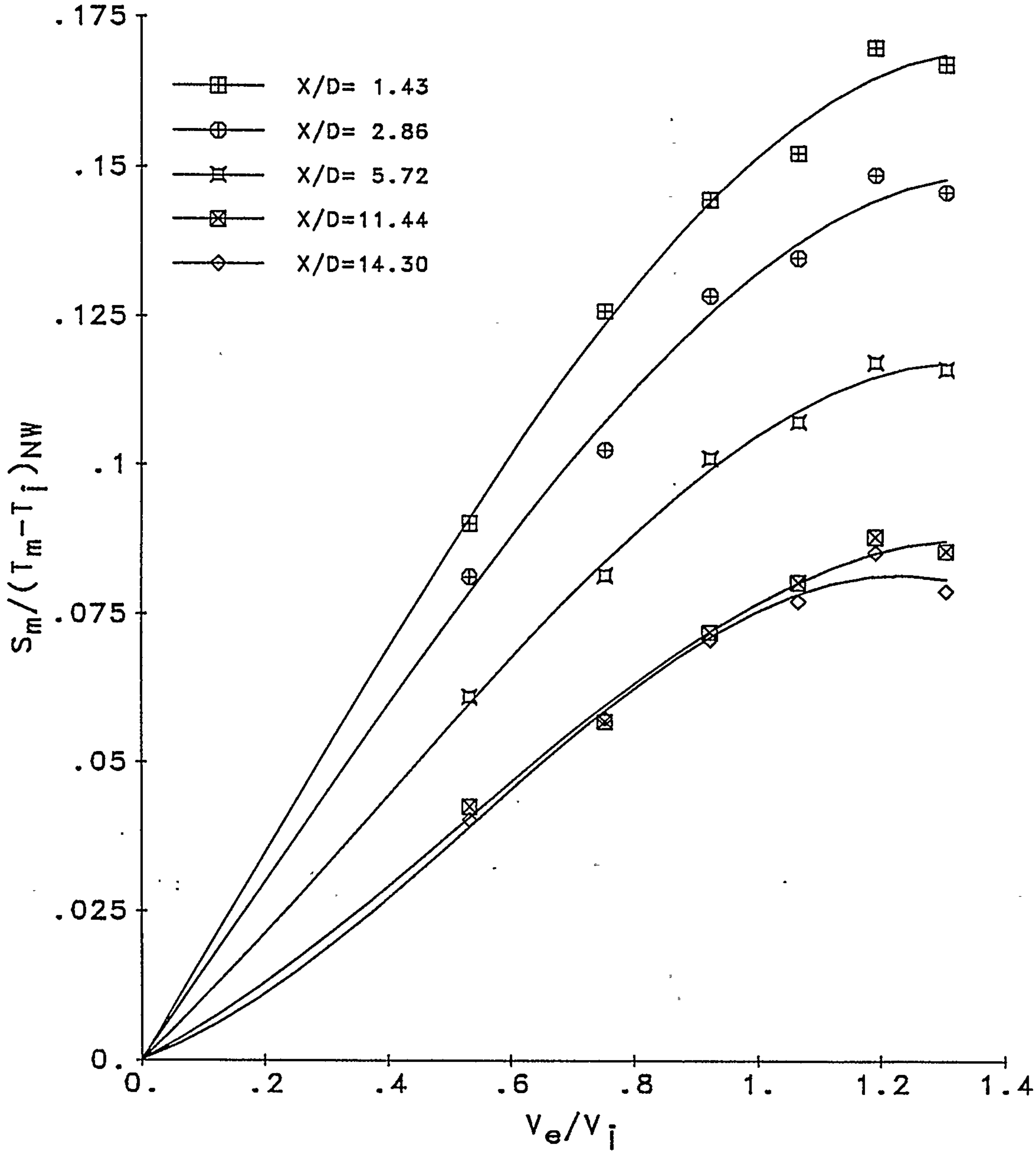

Fig. 5.1.38 The Net Variation of Relative Mixing Effectiveness Versus Pulsation Strength, See Fig. 5.1.30 for Other Data.

5.2 INVESTIGATION OF STROUHAL NUMBER EFFECT ON JET PENETRATION INTO THE CROSSFLOW

5.2.1 EXPERIMENTAL CONDITIONS AND PROCEDURE

These experiments consist of the temperature field measurements under "no-drive" and "drive" flow conditions at different Strouhal numbers $S_t=(fD/V_j)$. Momentum flux ratio, J, and power number, $\sqrt{\dot{W}} / \left(V_j \sqrt{\dot{M}_j} \right)$ were kept constant. The comparison was done in the transverse plane at a distance X/D=2.86 from the jet orifice. Because of the necessity of maintaining a 204Hz driving signal frequency, the variation in the Strouhal number was confined to changes in the jet velocity, V_j. This condition caused quite a complex experimental procedure. First of all, any change in the jet velocity resulted in variation of the jet momentum flux magnitude. Therefore, to preserve the momentum flux ratio, the crossflow conditions had to be adjusted. This in consequence required simultaneous setting of the main air mass flow and fuel delivery rates to the combustor in order to ensure as close as possible a constant temperature magnitude in the test chamber. Finally, the value of the power number had to be adjusted by setting the amplifier power output. Such a complex procedure was successfully completed only by means of the computer data acquisition system, which enabled control of the flow parameters during the experiment (Chapter 4.4).

The values of the experimental parameters (ranges and variation) are listed below;

- Strouhal number St=0.1866 to 0.3522
- power number average value $\sqrt{\dot{W}} / \left(V_j \sqrt{\dot{M}_j} \right) = 5.99$ (-10.0 to 5.8%),
- excitation velocity ratio $V_e/V_j = 1.13$ (-10.0 to 6.0%),
- jet to crossflow momentum flux ratio average value J=3.02 (-8.6 to 15.8%),
- average temperature of the crossflow 195.0^0C (±1.7%),
- average temperature of the jet $T_j=39.4^0C$ (-6.1 to 8.1%),
- jet velocity V_j=11.54-21.79 m/s,
- crossflow velocity U_∞=7.67-16.02 m/s,
- jet to crossflow mass flow ratio $\dot{M}_j/\dot{M}_\infty$=0.0156 to 0.0185,
- jet Reynolds number Re_j=11849 to 21720,
- crossflow Reynolds number Re_∞=35652 to 62606.

Temperature profiles for no jet flow, for particular mass flow conditions were also measured at the X/D=2.86 transverse plane. Fig. 5.2.1 shows that the difference in mass flow conditions has virtually no influence on the temperature profile.

The upper limit of the Strouhal number range was constrained by poor stability of the flow at low crossflow velocities (below U_∞=7.0 m/s). The lower limit of the Strouhal number range was due to problems in achieving a sufficient pressure gradient in the jet branch to maintain a constant momentum flux ratio. Simply, at high velocities the pressure losses in the jet branch could not be accommodated by the throttle valve opening.

5.2.2 TEST RESULTS "WITHOUT ACOUSTIC DRIVE"

In the "no-drive" case, the difference in mass flow conditions under the same momentum flux ratio should not cause changes in the temperature field. This is substantiated by the behaviour of the Θ_m and Θ parameters in Figs. 5.2.2 and 5.2.3 respectively. In addition, the centre-plane Θ profiles (Fig. 5.2.4) clearly show the conservation of the jet penetration. These graphs are in excellent agreement in terms of the order of magnitude of parameters and the field distribution. In conclusion, the flow pattern remained virtually unchanged under different mass flow conditions.

5.2.3 TEST RESULTS "WITH ACOUSTIC DRIVE"

The experimental results for the "drive" case are presented in the form of Θ_m and Θ contours, Fig. 5.2.5 and Fig. 5.2.6 respectively, together with centre-plane Θ profiles in Fig. 5.2.7, for different Strouhal number conditions. The contours show not only strong change in comparison to the "no-drive" case but also definite change with the Strouhal number variation. Investigation of the Θ_m maps (Fig. 5.2.5), shows that the jet position changes with an increase of the Strouhal number. The Θ parameter contours (Fig. 5.2.6) even show some interference between the jet zone (toroidal vortex) and the tunnel ceiling at St=0.2844 and 0.2969. This is confirmed by the unusual shape of the centre-plane Θ profiles for these cases (Fig. 5.2.7).

5.2.4 DISCUSSION

The overall Strouhal number effect is shown best by the jet penetration. The available data normalized in the form, $\Delta Y/Y_o$, are plotted against Strouhal number, St, in Fig. 5.2.8. The values presented in the graph were obtained from the centre-plane vertical Θ profiles (Figs. 5.2.4 and 5.2.7). Very clearly the optimum penetration occurs at St=0.29, hence for a given acoustic excitation (constant relative pulsation strength V_e/V_j) maximum penetration will be obtained at this Strouhal number. Experimental points at St=0.2844 and 0.2969 have been excluded due to profile distortion caused by the action of the travelling toroidal vortices, which were very strong due to these test being close to the optimum St (Fig. 5.2.7).

Θmax is well defined and should therefore be an effective indicator of Strouhal number effect. This is presented in Fig. 5.2.9 where the minimum value indicates the optimum St (Θmax minimizes as $T \Rightarrow T_m$ "with-drive"). The optimum Strouhal number by this approach is therefore St=0.27. The Strouhal number effect may also be assessed by the relative mixing effectiveness S_m. The normalized data as $S_m/(T_m-T_j)$ are presented in Fig. 5.2.10, where the minimum value indicates the most effective mixing, and therefore the optimum Strouhal number is St=0.25, in fair agreement with that found from penetration and Θmax.

The average optimum Strouhal number is therefore 0.27 as determined by penetration and mixing. This is 24% greater than that found from the cold flow work (Ref. 2), St=0.22. However, an optimum St=0.25 for the entrainment rate and mixing found for the free jet in Ref. 1 and Ref. 5 agrees with the St range established by this new work. The optimum St established by the cold flow work is understandably low because of data limitations. There is good agreement with the maximum turbulence optimum St=0.30 obtained by Crow and Champagne (Ref. 24) and confirmed by Seno, Kageyama and Ito (Ref. 31), for free jet centre-line turbulence measurements, which supports an optimum Strouhal number of 0.27 for mixing and penetration.

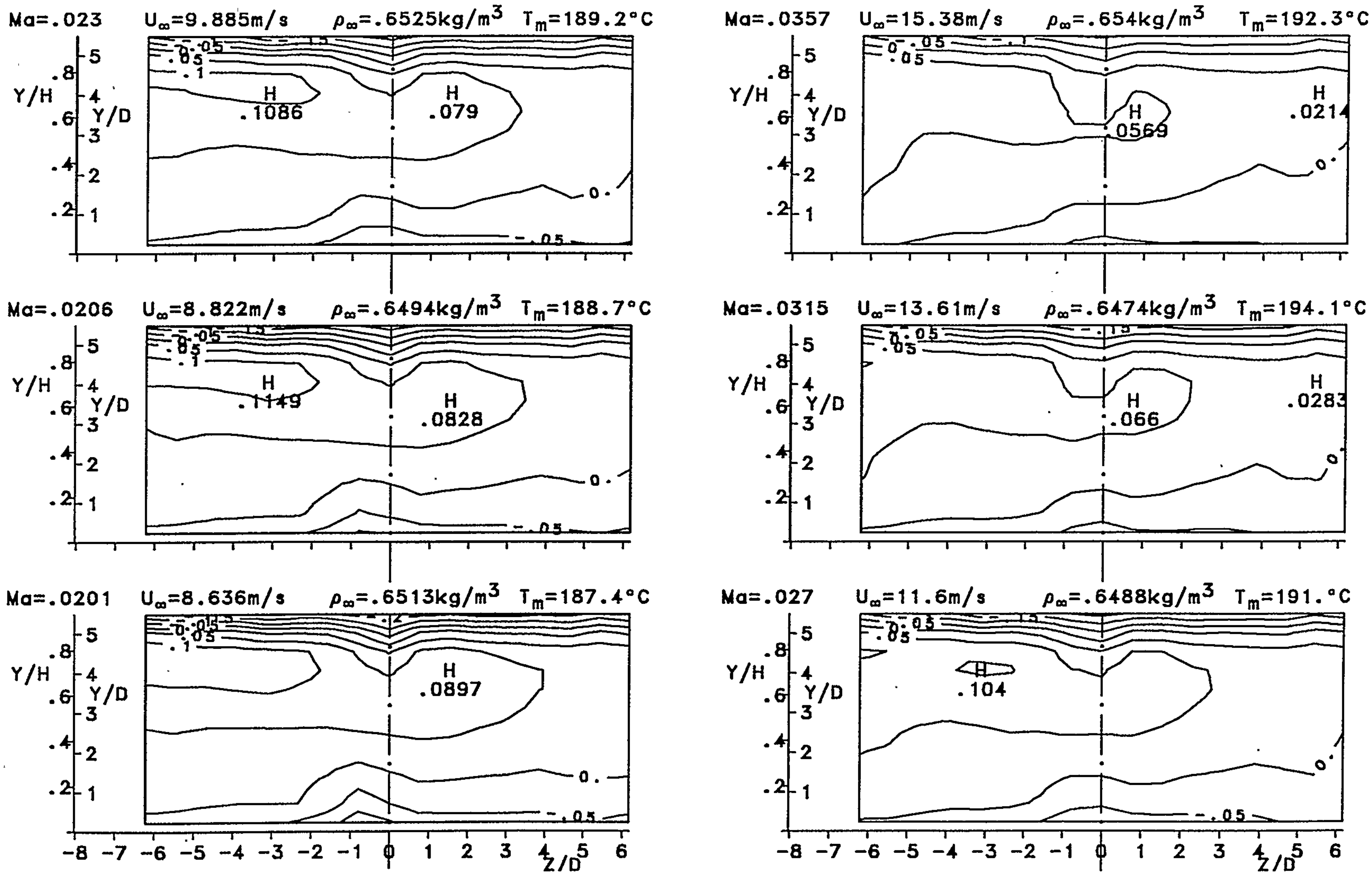

Fig. 5.2.1 Θ_m Mean Temperature Contours for Different Flow Conditions, No Jet Flow, X/D=2.86, Contour Interval 0.05.

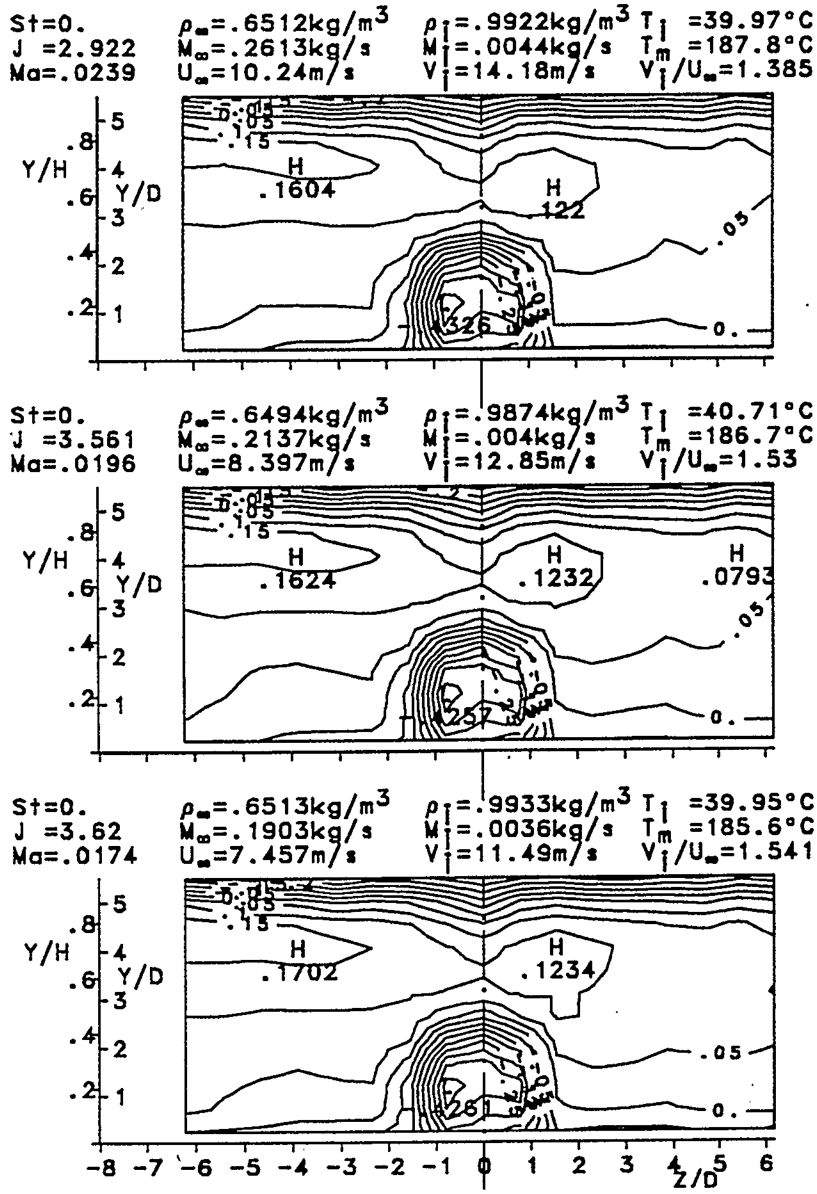

Fig. 5.2.2 θ_m Contour Maps for Different Flow Conditions, "no-drive" Case, D=19.93mm Dia., X/D=2.86, U_∞=7.46-10.24 m/s, Contour Interval 0.05;

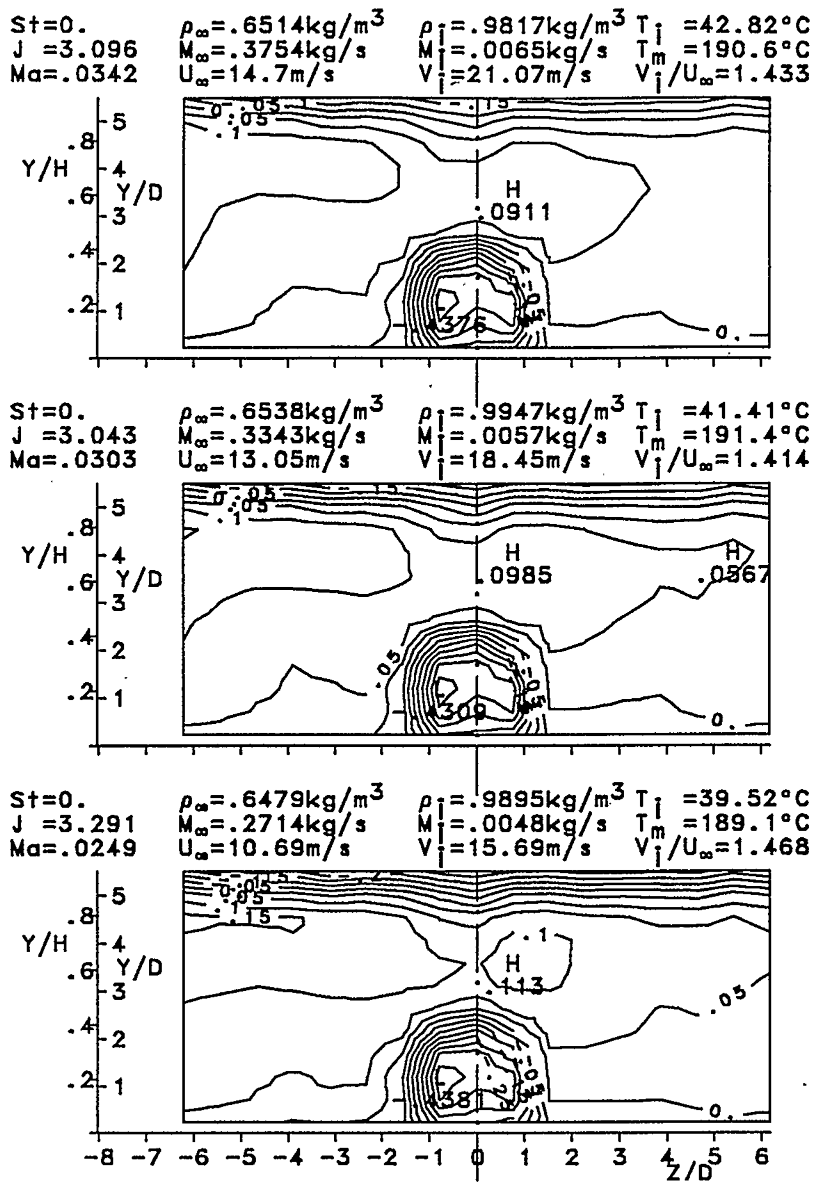

Fig. 5.2.2 continued, U_∞=10.69-14.70 m/s.

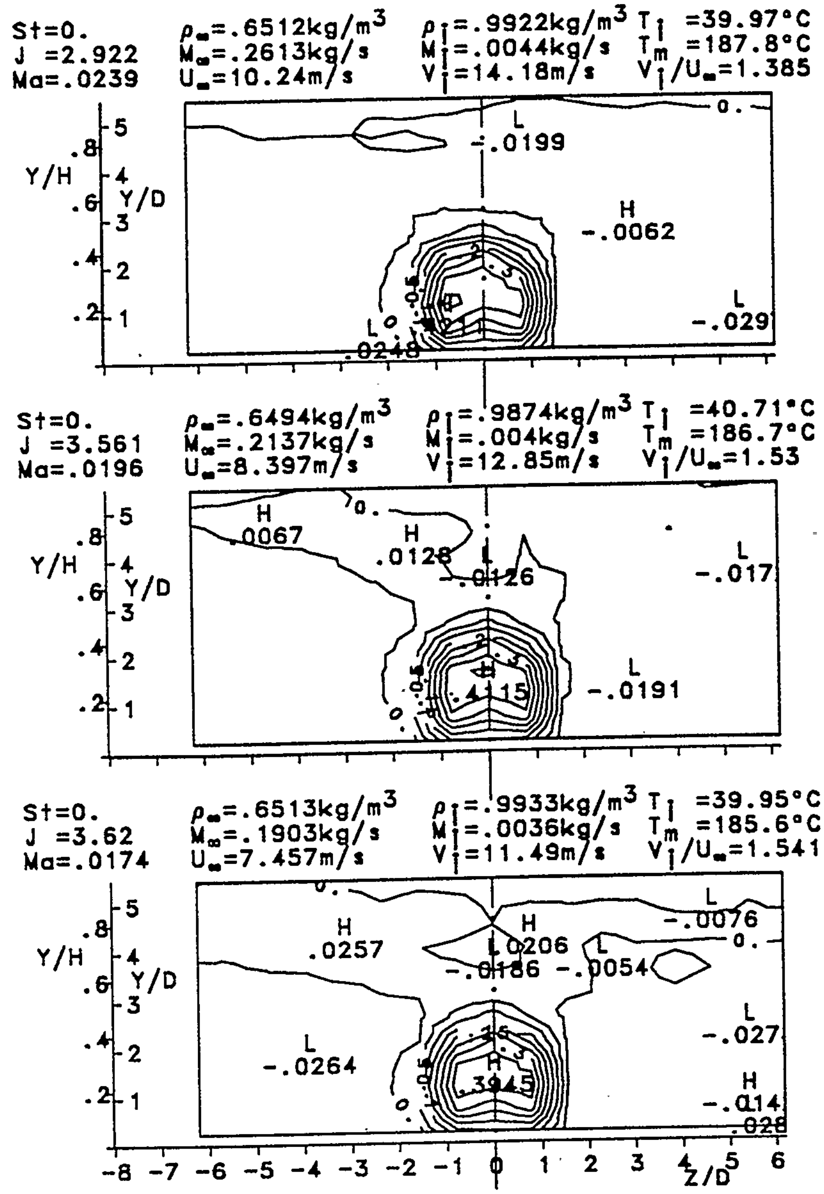

Fig. 5.2.3 θ Contour Maps for Different Flow Conditions, "no-drive" Case, D=19.93mm Dia., X/D=2.86, U_∞=7.46-10.24 m/s, Contour Interval 0.05;

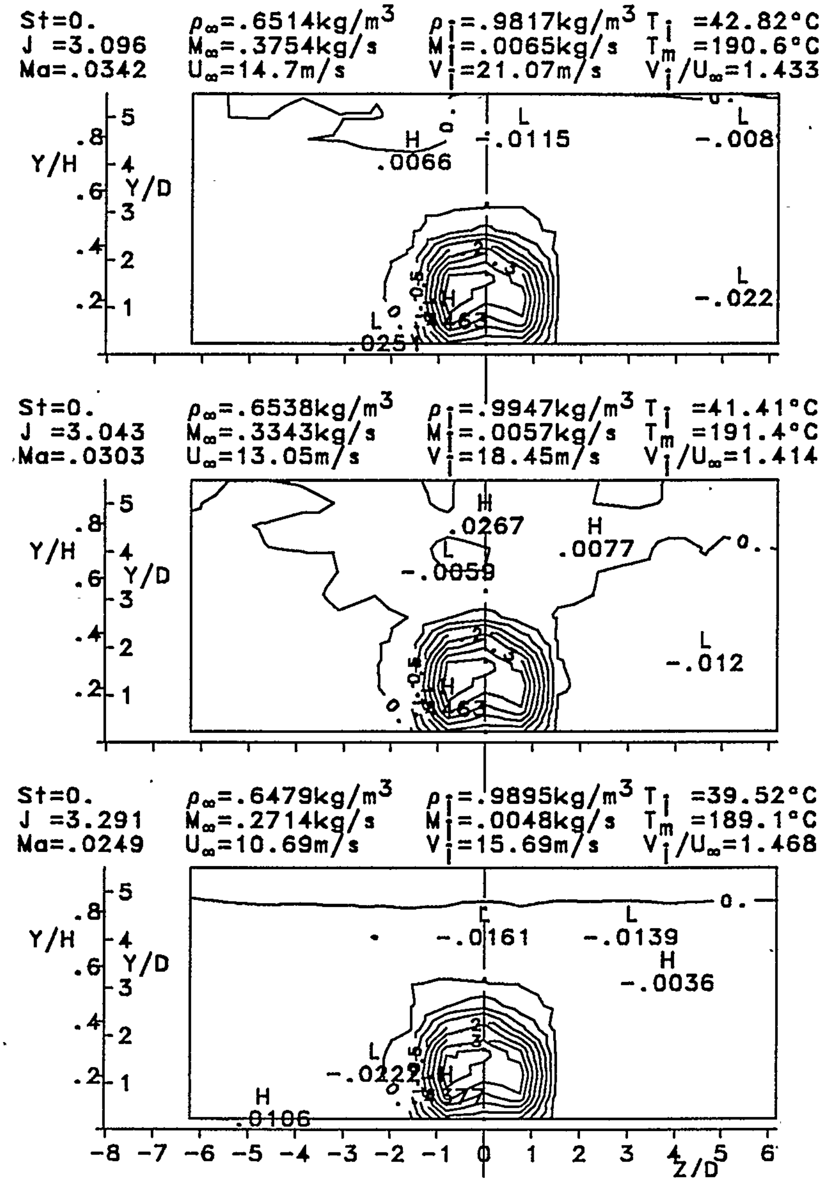

Fig. 5.2.3 continued, U_∞=10.69-14.70 m/s.

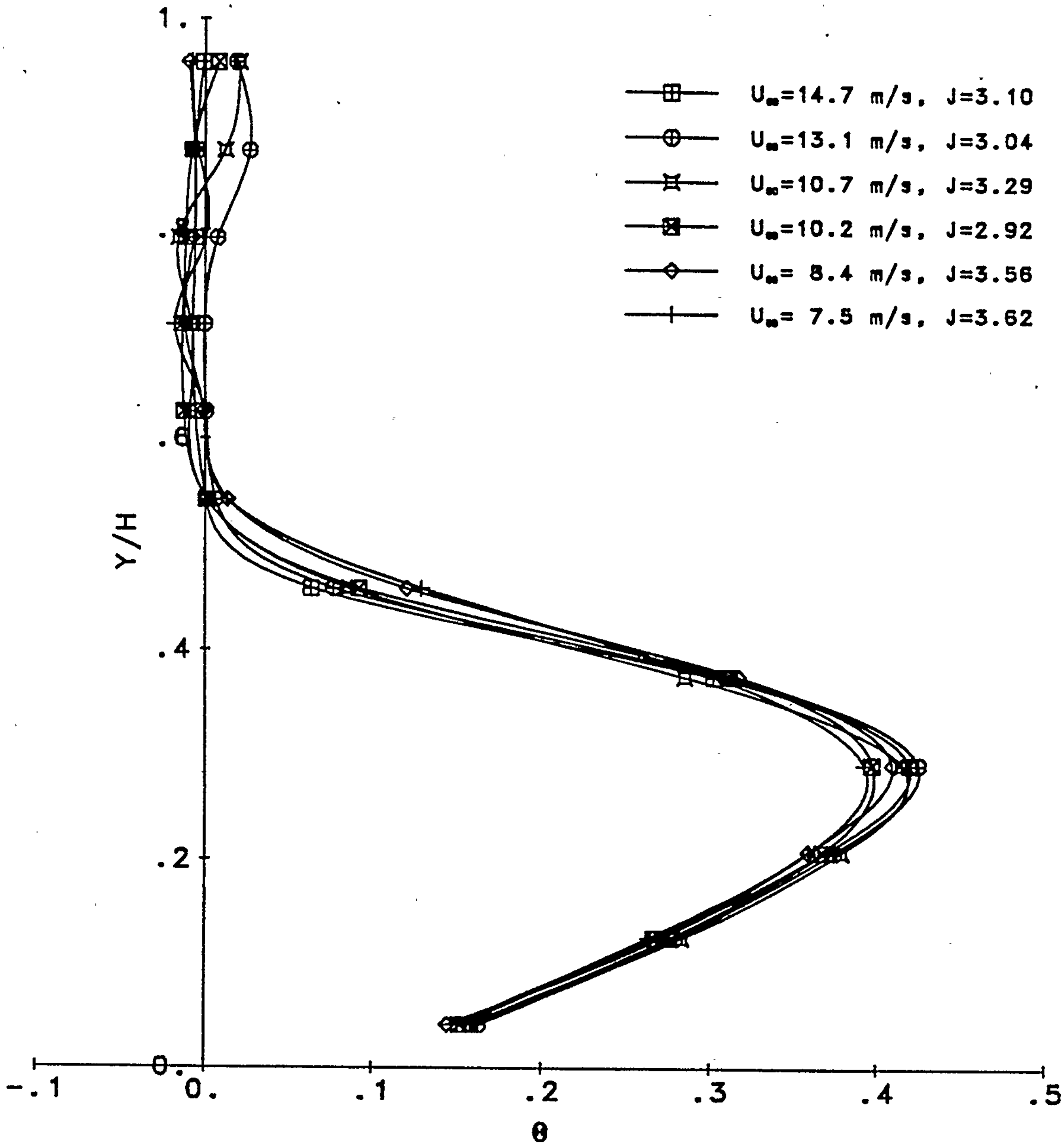

Fig. 5.2.4 Centre-Plane θ Profiles for Different Flow Conditions, D=2.86mm Dia., X/D=2.86, "no-drive" Case.

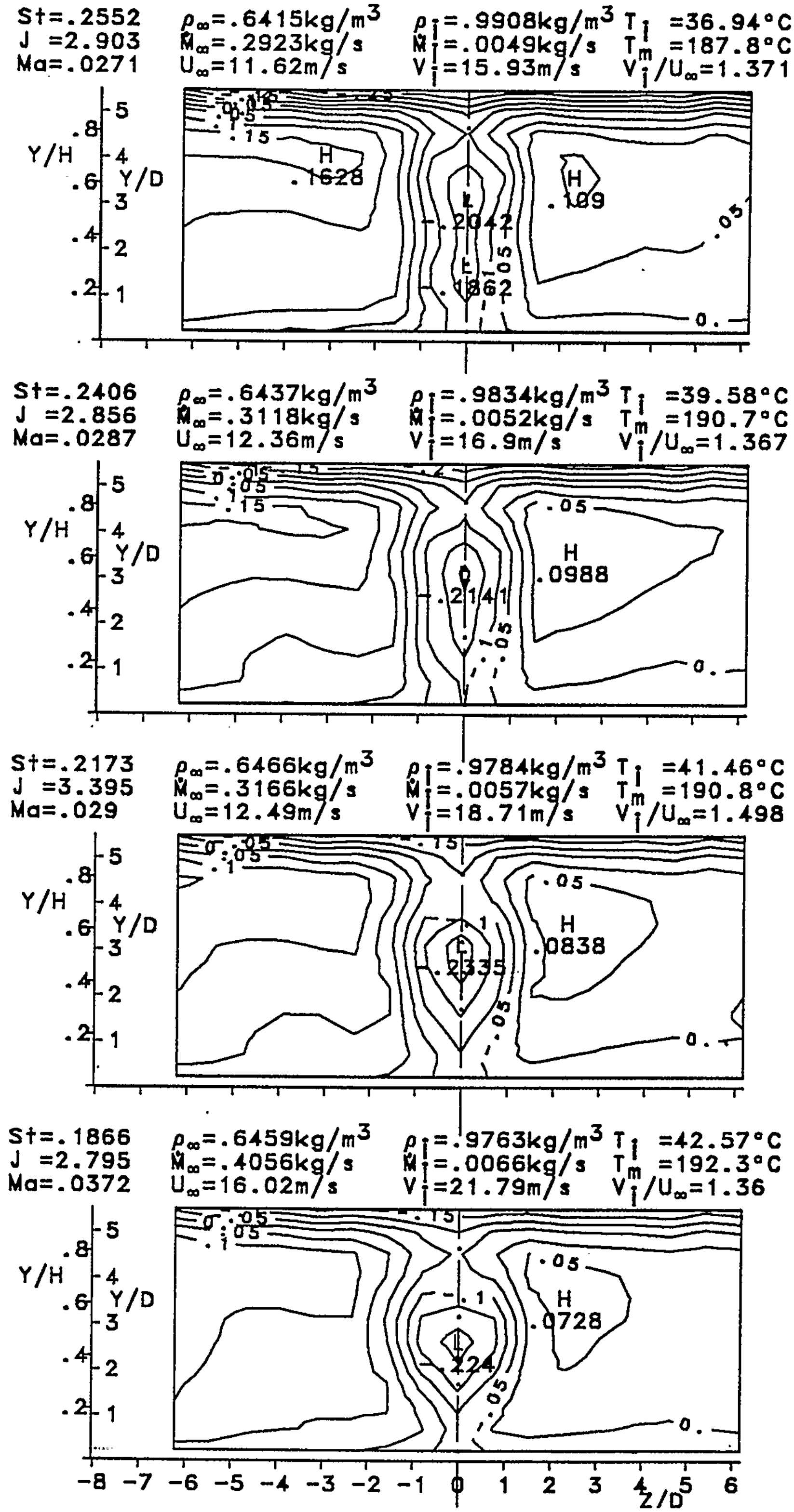

Fig. 5.2.5 Θ_m Contour Maps for Different Strouhal Numbers, St=0.1866-0.2552, D=19.93mm Dia., X/D=2.86, 204 Hz, V_e/V_j=1.13;

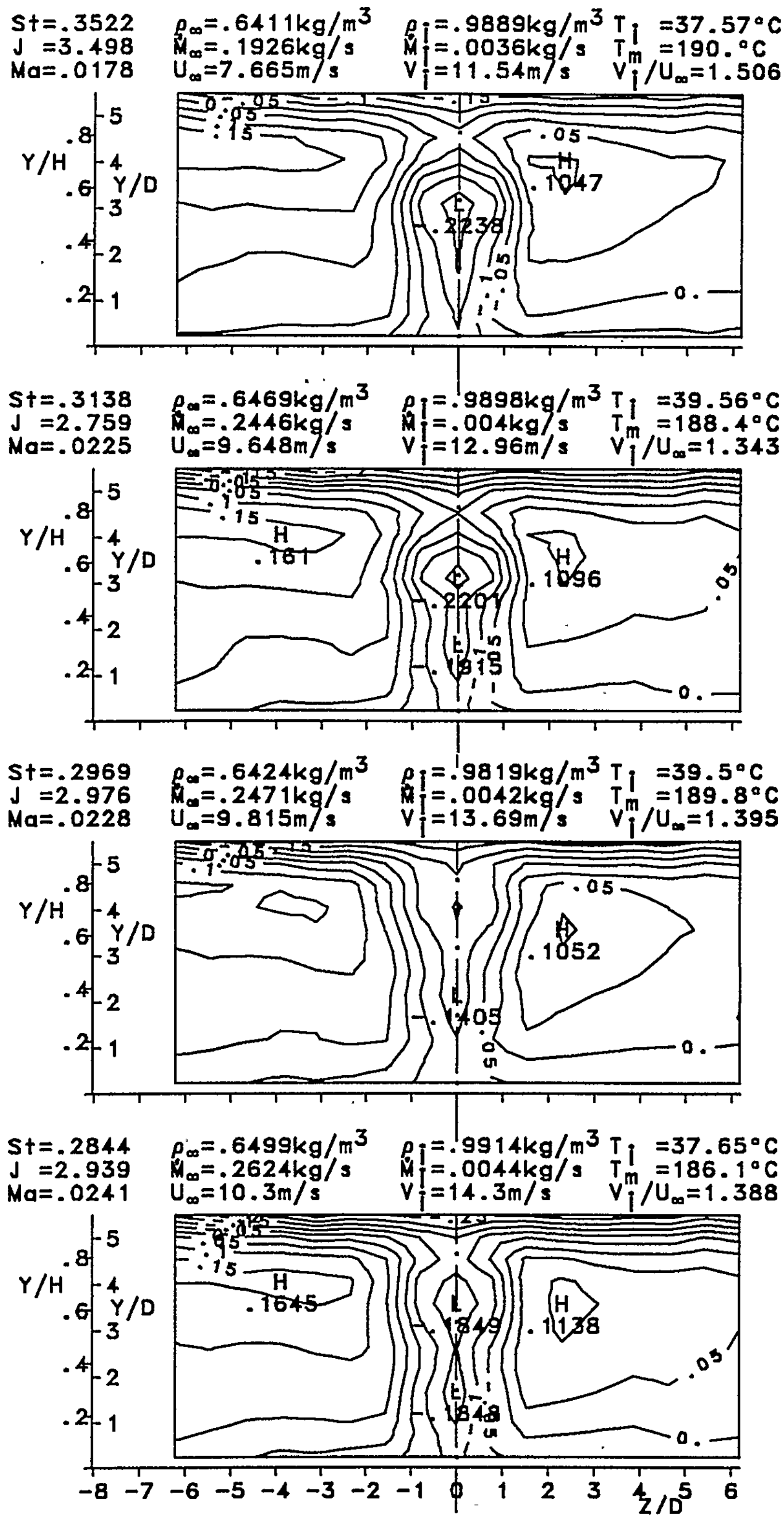

Fig. 5.2.5 continued, St=0.2844-0.3522, Total Re_j Range 11849-21720, Total Re_∞ Range 35652-62606.

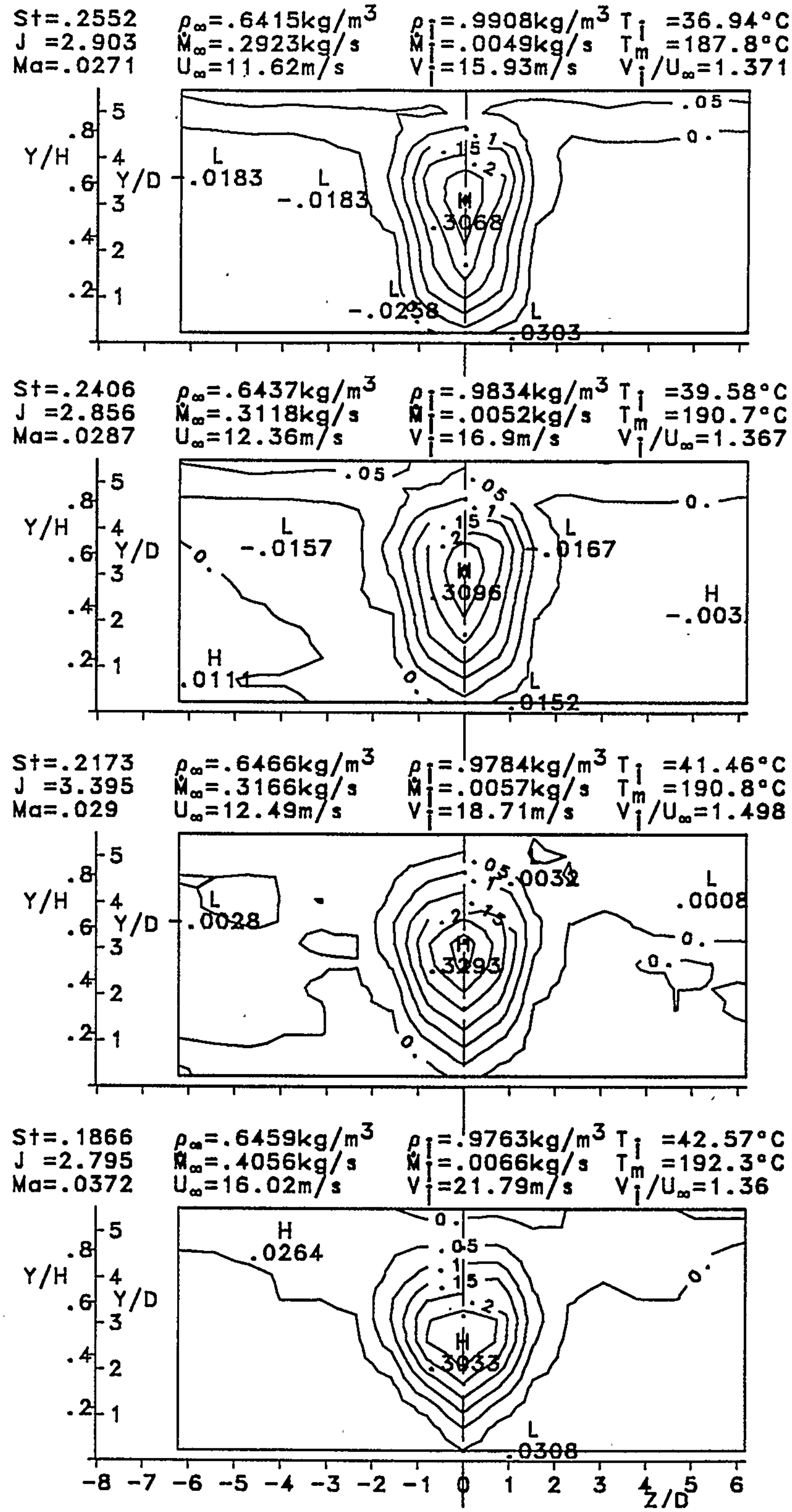

Fig. 5.2.6 θ Contour Maps for Different Strouhal Numbers, St=0.1866-0.2552, D=19.93mm Dia., X/D=2.86, 204 Hz, V_e/V_j=1.13;

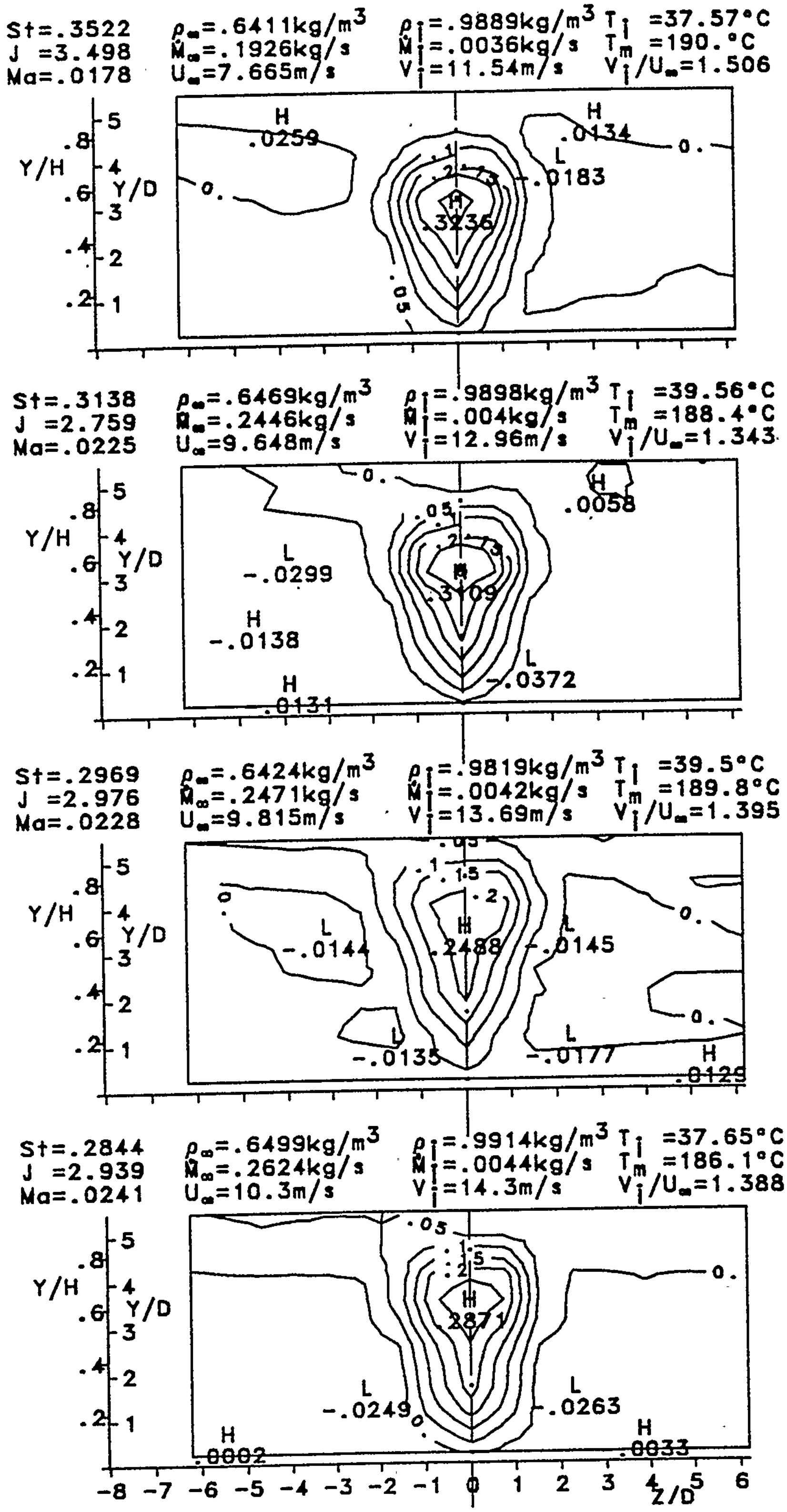

Fig. 5.2.6 continued, St=0.2844-0.3522, Total Rej Range 11849-21720, Total Re_∞ Range 35652-62606.

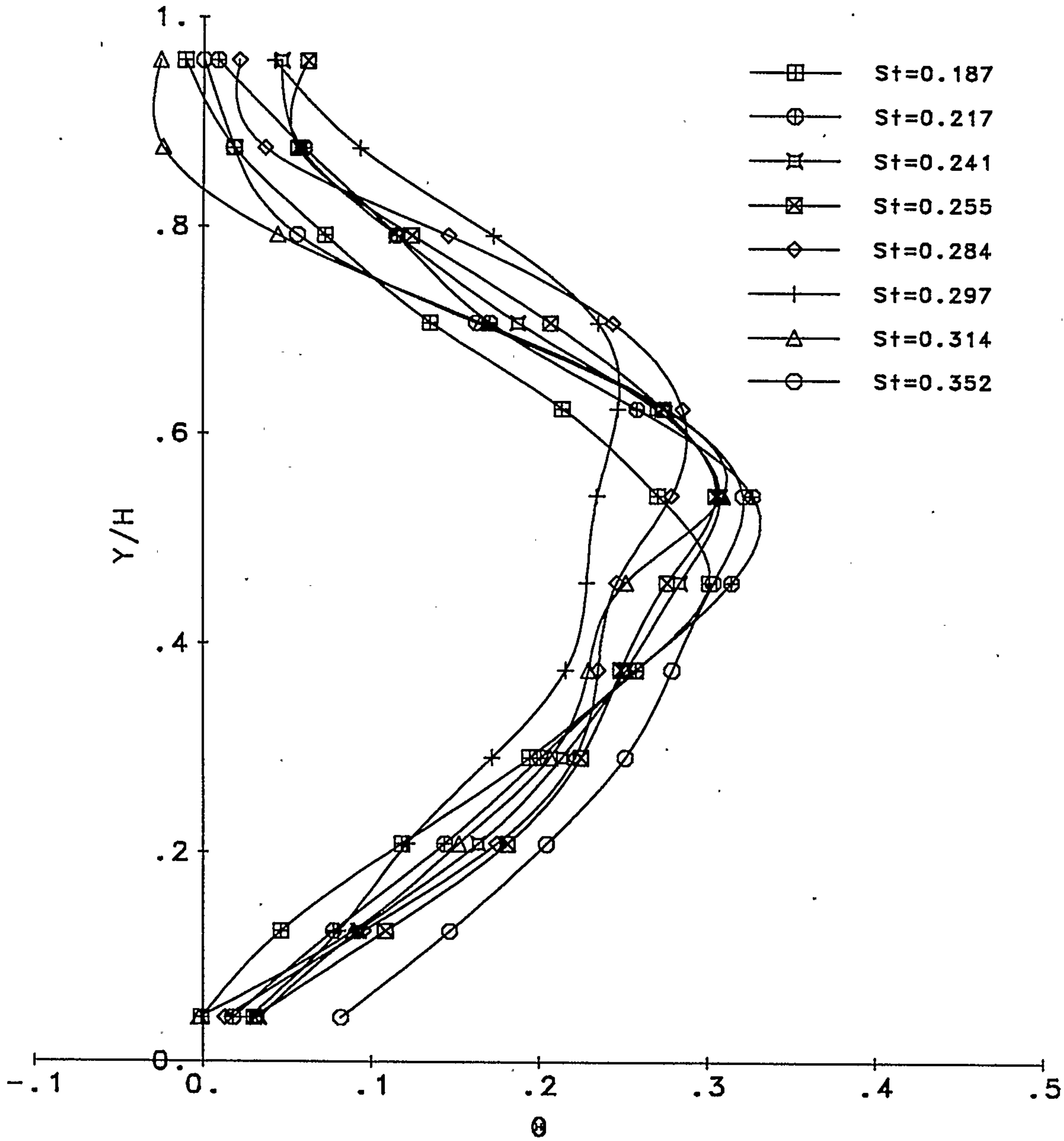

Fig. 5.2.7 Centre-Plane θ Profiles for Different St Conditions, See Fig. 5.2.6 for Other Data.

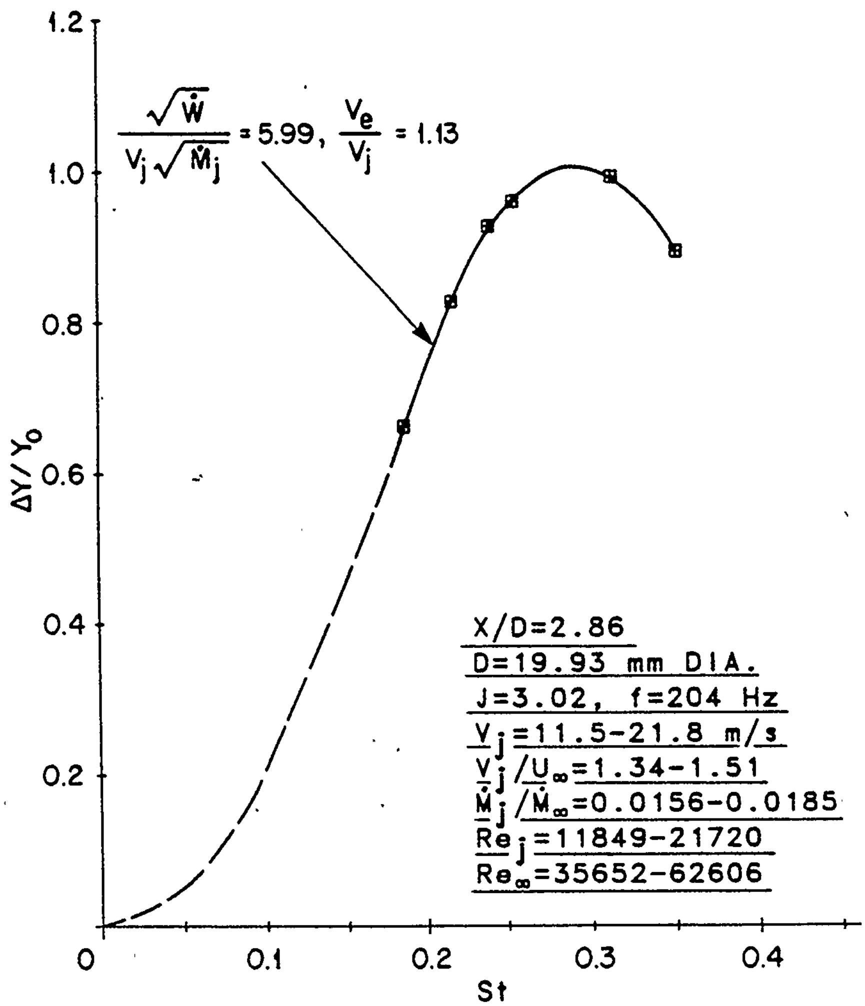

Fig. 5.2.8 Relative Change in Jet Penetration Versus Strouhal Number. Average Conditions, T_j=40°C, $\overline{T}_\infty$=190°C, ρ_j=0.985 kg/m^3, ρ_∞=0.644 kg/m^3.

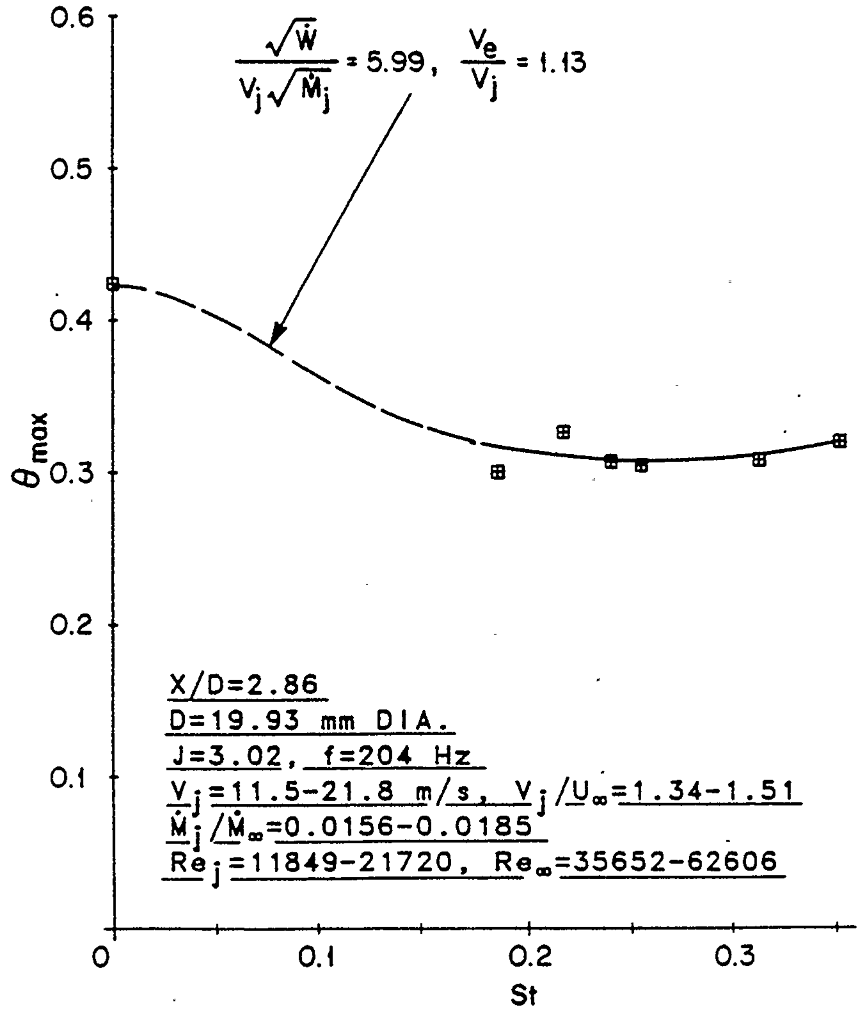

Fig. 5.2.9 θmax Versus Strouhal Number, See Fig. 5.2.8 for Other Data.

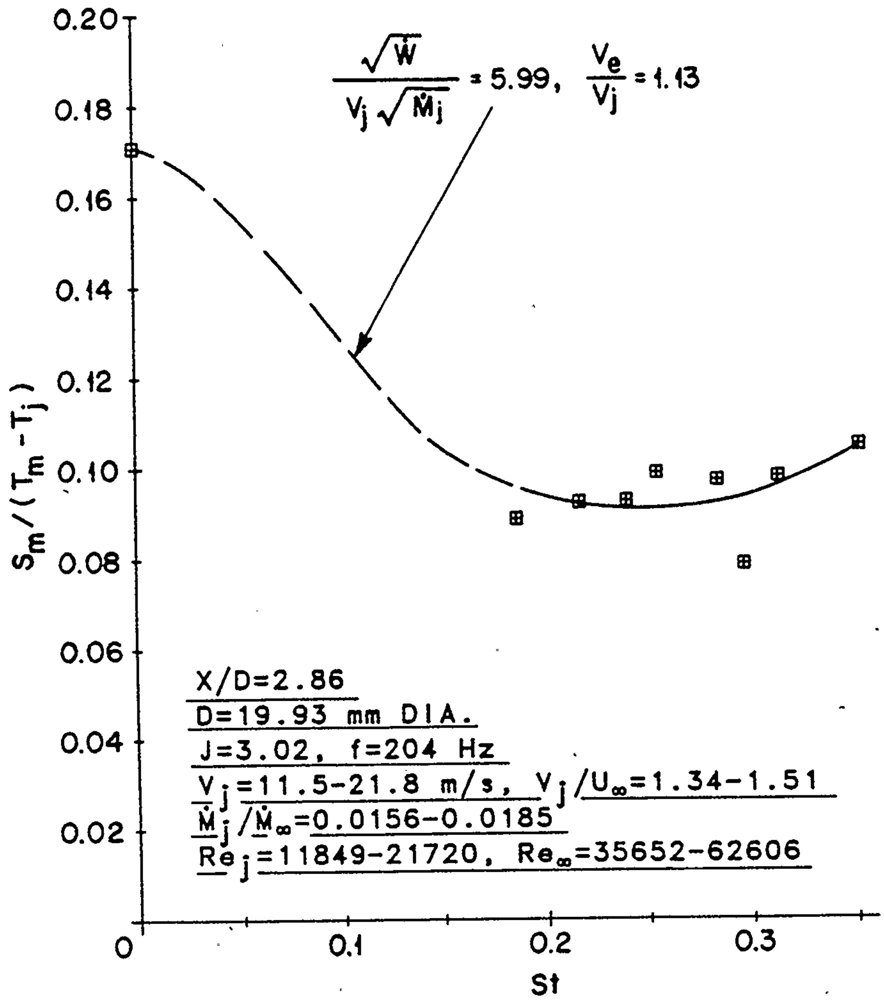

Fig. 5.2.10 Relative Mixing Effectiveness Versus Strouhal Number, See Fig. 5.2.8 for Other Data.

CHAPTER 6

CONCLUSIONS AND RECOMMENDATIONS

6.1 CONCLUSIONS

The experimental investigation into the mixing of an acoustically excited air jet with a confined hot crossflow showed that the excitation produced strong changes in the measured temperature profiles. This resulted in significant increases in mixing zone size, penetration (at least 100% increase), mixing, and the length to achieve a given mixed state was shortened by at least 70%. There was strong modification to the jet-wake region. The increase in the jet penetration and mixing was saturating near 90W, the largest driving power tested. The jet response as determined by penetration and mixing was optimum at a Strouhal number of 0.27. Overall, pulsating the jet flow significantly improved the jet mixing processes in a controllable manner.

6.2 RECOMMENDATIONS FOR FUTURE WORK

This work of necessity, has not been able to address all important aspects available for study. Those remaining are listed below together with the remaining ones from Yu (Ref. 4) and Chin (Ref. 1) as recommendations for future work to carry out;

(1) further investigation of the phenomenon under conditions of different momentum flux ratio, pulsation strength and Strouhal number,

(2) studies of unopposed multiple jets penetration into a hot crossflow,

(3) investigation of a driving phase influence on multiple jets penetration into a crossflow,

(4) investigation of opposed jets projecting into a hot crossflow (including off-set jets),

(5) development of a flow visualization technique, particularly to explore the toroidal vortex shedding, jet-wake region, bound vortices and interactions near the jet orifice,

(6) investigation of the effect of jet orifice shape on the jet(s)-in-crossflow,

(7) detailed measurements on the properties of toroidal vortices near the jet orifice (over about the first ten diameters) for a free jet, and for a jet in crossflow,.

(8) theoretical and experimental investigation of the driver system in order to optimize the jet excitation,

(9) development of a measurement technique for the energy actually pulsating the jet flow.

REFERENCES

1. Ching-Fatt Chin, "An experimental Study of the Mixing Behavior of an Acoustically Pulsed Air Jet with a Confined Crossflow", M.Sc. Thesis, University of Calgary, Department of Mechanical Engineering, December, 1987.
2. Vermeulen, P.J., Ching-Fatt Chin, Yu, W.K., "An experimental Study of the Mixing Behavior of an Acoustically Pulsed Air Jet with a Confined Crossflow", AIAA-88-3296 Paper, July 1988.
3. Vermeulen, P.J., Ramesh, V., Yu, W.K., "Measurement of Entrainment by Acoustically Pulsed Asymmetrical Air Jets", J. of Engineering for Gas Turbine and Power, Trans. ASME., Vol. 108, No.3, July 1986, pp.479-484.
4. Yu, W.K., "An experimental Study of the Mixing Behavior of an Acoustically Pulsed Air Jets", M.Sc. Thesis, University of Calgary, Department of Mechanical Engineering, July 1985.
5. Vermeulen, P.J., Yu, W.K., "An Experimental Study of the Mixing by an Acoustically Pulsed Air-Jet", Int. J. of Turbo & Jet-Engines, Vol.4, No. 3-4, 1987, pp.225-237.
6. Vermeulen, P.J., Odgers, J., Ramesh, V., "Acoustic Control of Dilution-Air Mixing in a Gas Turbine Combustor", J. of Engineering for Power, Trans. ASME, Vol. 104, No. 4, October 1982, pp. 844-852.

7. Vermeulen, P.J., Odgers J., Ramesh V., "Full Load Operation of a Gas Turbine Combustor with Acoustically Controlled Dilution-Air Mixing", Int. J. of Turbo & Jet Engines, Vol. 4, Nos. 1-2,1987, pp.139-147.

8. Vermeulen, P.J., Odgers J., "Acoustic Control of the Exit Plane Thermodynamic State of a Combustor", ASME 24th International Gas Turbine Conference, San Diego, Cal., Paper 79-GT-180, March 12-15, 1979, pp. 1-12.

9. Moussa, Z.M., Trischka, J.W., Eskinazi, S., "The Near Field in the Mixing of a Round Jet with a Cross Stream", J. of Fluid Mechanics, Vol. 80, 1977, pp. 49-80.

10. Chassaing, P., George, J., Claria, A., Sananes, F., "Physical Characteristics of Subsonic Jets in a Cross-Stream", J. of Fluid Mechanics, Vol. 62, 1974, pp. 41-64.

11. Bojic, M.L., Eskinazi S., "Two-Dimensional Mathematical Model of a Nonbuoyant Jet in a Crossflow", AIAA Journal, Vol. 17, 1979, pp.1050-1054.

12. Andreopoulos, J., Rodi, W., "Experimental Investigation of Jets in a Crossflow", J. of Fluid Mechanics, Vol. 138, pp. 93-127.

13. Andreopoulos, J., "Measurement in a Jet Pipe Flow Issuing Perpendicularly into a Cross Flow", J. of Fluids Engineering, Trans. ASME., Vol. 104, 1982, pp. 493-499.

14. Lefebvre, A.W., "Gas Turbine Combustion", Chapter 4, McGraw-Hill, New York, 1983, pp. 117-126.

15. Abramovich, G.N., "The Theory of Turbulent Jets", The M.I.T. Press, Cambridge, Massachusetts, 1963.

16. Fearn, R., Weston R.P., "Vorticity Associated with a Jet in a Cross Flow", AIAA. Journal, Vol. 12, December 1974, pp. 1666--1671.

17. Kamotani, Y., Grebner I., "Experiments on a Turbulent Jets in a Cross Flow", AIAA. Journal, Vol. 10, November 1972, pp. 1425-1429.

18. Holdeman, J.D., Walker, R.E., "Mixing of a Row of Jets with a Confined Crossflow", AIAA. Journal, Vol. 15, 1977, pp. 243-249.

19. Michalke, A., "The Instability of a Compressible Circular Jet with Fine Boundary Layer Thickness", Zeitschrift fur Flugwissenschaften, Vol. 19, Aug./Sept. 1971, pp 319-327.

20. Browand, F.,K., Laufer, J., "The Role of Large Scale Structures in the Initial Development of Circular Jets", Proceedings of the Four Biennial Symposium on Turbulence in Liquids, University of Missouri-Rolla, 1975, pp. 333-344.

21. Sarohia, V., Massier, P.F., "Experimental Results of Large-Scale Structures in Jet Flows and Their Relation to Jet Noise Production", AAIA Journal, Vol. 16, 1978, pp. 831-835.

22. Yule, A.J., "Large-Scale Structure in the Mixing Layer of a Round Jet", J. of Fluid Mechanics, Vol. 89, Part 3, 1978, pp. 413-432.

23 Ho, Chih-Ming, Huerre, P., "Perturbed Free Shear Layer",

Annual Reviews of Fluid Mechanics, Vol. 16, 1984, pp. 365-424.

24. Crow, S.C., Champagne, F.H., "Orderly Structure in Jet Turbulence", J. of Fluid Mechanics, Vol. 48, August 1971, pp. 547-591.

25. Ito, R., Seno, T., "Effect of Exit Geometry on Jet Behavior", J. of Chemical Eng. of Japan, Vol. 12, 1979, pp.430-435.

26. Anderson, A.B.C., "Structure and Velocity of the Periodic Vortex-Ring Flow Pattern of a Primary Pfeifenton (Pipe Tone) Jet", J. of the Acoustic Society of America, Vol. 27, 1955, pp.1048-1053.

27. Anderson, A.B.C., "Vortex-Ring Structure-Transition in a Jet Emitting Discrete Acoustic Frequencies", J. of the Acoustic Society of America, Vol. 28, 1956, pp.914-921.

28. Petersen, R.A., "Influence of Wave Dispersion on Vortex Pairing in a Jet", J. of Fluid Mechanics, Vol. 89, 1978, pp. 469-495.

29. Kibens, V., "Discrete Noise Spectrum Generated by an Acoustically Excited Jet", AAIA Journal, Vol. 18, No.4, April 1980, pp. 434-441.

30. Becker, H.A., Massaro, T.A., "Vortex Evolution in a Round Jet", J. of Fluid Mechanics, Vol. 31, Part 3, 1968, pp. 435-448.

31. Seno, T., Kageyama, S., Ito, R., "Effect of Controlled Pulsation on Axisymmetric Jet Behavior", J. of Chemical Eng.

of Japan, Vol. 20, 1987, pp.128-133.

32. Maxworthy, T., "Some experimental Studies on Vortex Rings", "Some Experimental Studies of Vortex Rings", J. of Fluid Mechanics, Vol. 81, 1977, pp. 465-495.

33. Disselhorst, J.H.M., van Wijngaarden, L., "Flow in the Exit of Open Pipes During Acoustic Resonance", Journal of Fluid Mechanics, Vol. 99, 1980, pp. 293-319.

34. Vermeulen, P.J., Danilowich, M.S., Heylauff, E.P., Price T.W., "The Acoustically Excited Flame", J. of Eng. for Power, Vol. 98, 1976, pp. 147-158.

35.. Binder, G., Favre-Marinet, M. "Mixing Improvement in Pulsating Turbulent Jets", ASME Symposium on Fluid Mechanics of Mixing, Georgia Institute of Technology, Atlanta, GA, June 20-22, 1973,pp. 167-172.

36. Ricou, F.P., Spalding, D.B., "Measurements of Entrainment by Axisymmetrical Turbulent Air Jets", J. of Fluid Mechanics, Vol. 11, 1961, pp. 21-32.

37. Ower, E., Pankhurst, R.C.,"The Measurement of Airflow", 5th Edition, Pergamon Press, 1977.

38. Walker, R.E., Kors, K.L., "Multiple Jet Study - Final Report", NASA CR-121217, 1973.

39. Ramsey, J.W., Goldstein, R.J., "Interaction of a Heated Jet with a Deflecting Stream", J. of Heat Transfer, Trans. ASME, Vol. 93, November 1971, pp. 365-372.

40. Hill W.G., Greene, P.R., " Increase Turbulent Jet Mixing

Rates Obtained by Self-Excited Acoustic Oscillations", Trans. ASME, J. of Fluids Engineering, Vol. 99, No. 3, September 1977, pp. 520-525.

41. Ramaprian, B.R., Haniu, H., "Measurement in Two-Dimensional Plumes in Crossflow", J. of Fluids Engineering, Trans. ASME, Vol. 111, June 1989, pp.130-189.

42. Bergeles, G, Gosman, A.D., Launder, B.E., "The Near-Field Character of a Jet Discharged Normal to a Main Stream", J. of Heat Transfer, Trans. ASME, Vol. 98, 1976, pp. 373-378.

43. Lloyd, S., Brown, A, "Velocity and Turbulence in Pipe Entrance Regions in the Presence of Cross Flow", Transaction of the ASME, Vol. 108, July 1987, pp.498-503.

44. Seno, T., Kageyama, S., Ito, R., "A Modeling of Vortex Rings in an Axisymmetric Pulsed Jet", J. of Chemical Eng. of Japan, Vol. 21, 1988, pp.1-5.

45. Fiedler, H.E., Mensing, P., "The Plane Turbulent Shear Layer with Periodic Excitation", J. of Fluid Mechanics, Vol. 150, 1985, pp. 281-309.

APPENDIX

Pressure	Transducer Type	Measurement Type	Range
P_a	NATIONAL LX 1801 AX Ch.3	absolute	69-138kPa
P_f	NATIONAL LX 1801 AX Ch.7	absolute	69-138kPa
P_∞	NATIONAL LX 1801 AX Ch.4	absolute	69-138kPa
P_r	VALIDYNE P305D - 30	differen[1]	8.6 kPa
P_j	VALIDYNE P305D - 26	differen[1]	3.5 kPa
ΔP_r	VALIDYNE P305D - 20	differen[1]	548.0 Pa
ΔP_f	VALIDYNE P305D - 20	differen[1]	548.0 Pa

Tabl. A1 List of Transducers Used During the Experiment.

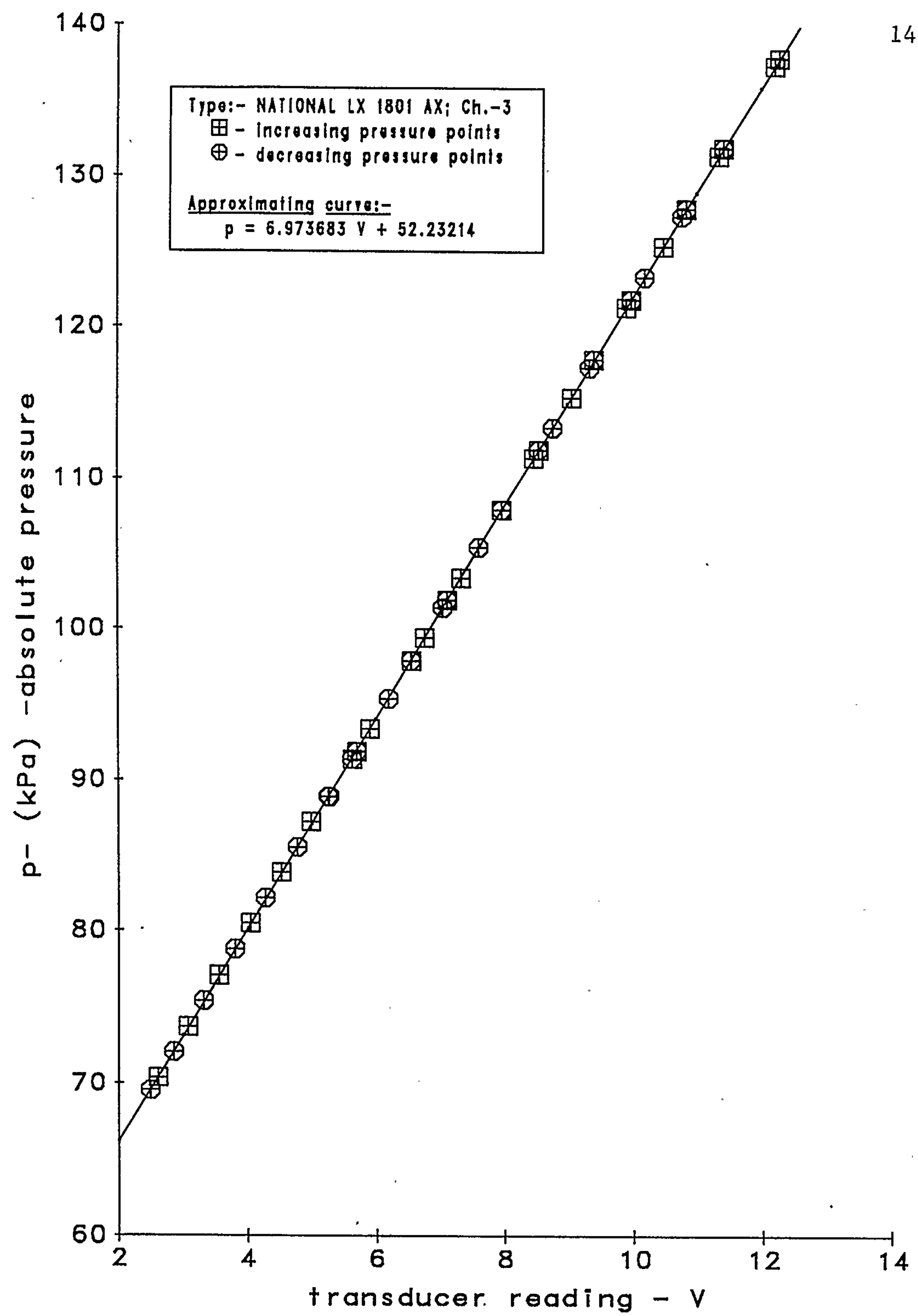

Fig.A1 Calibration of Pressure Transducer.

Type:- NATIONAL LX 1801 AX, Ch.- 3 .

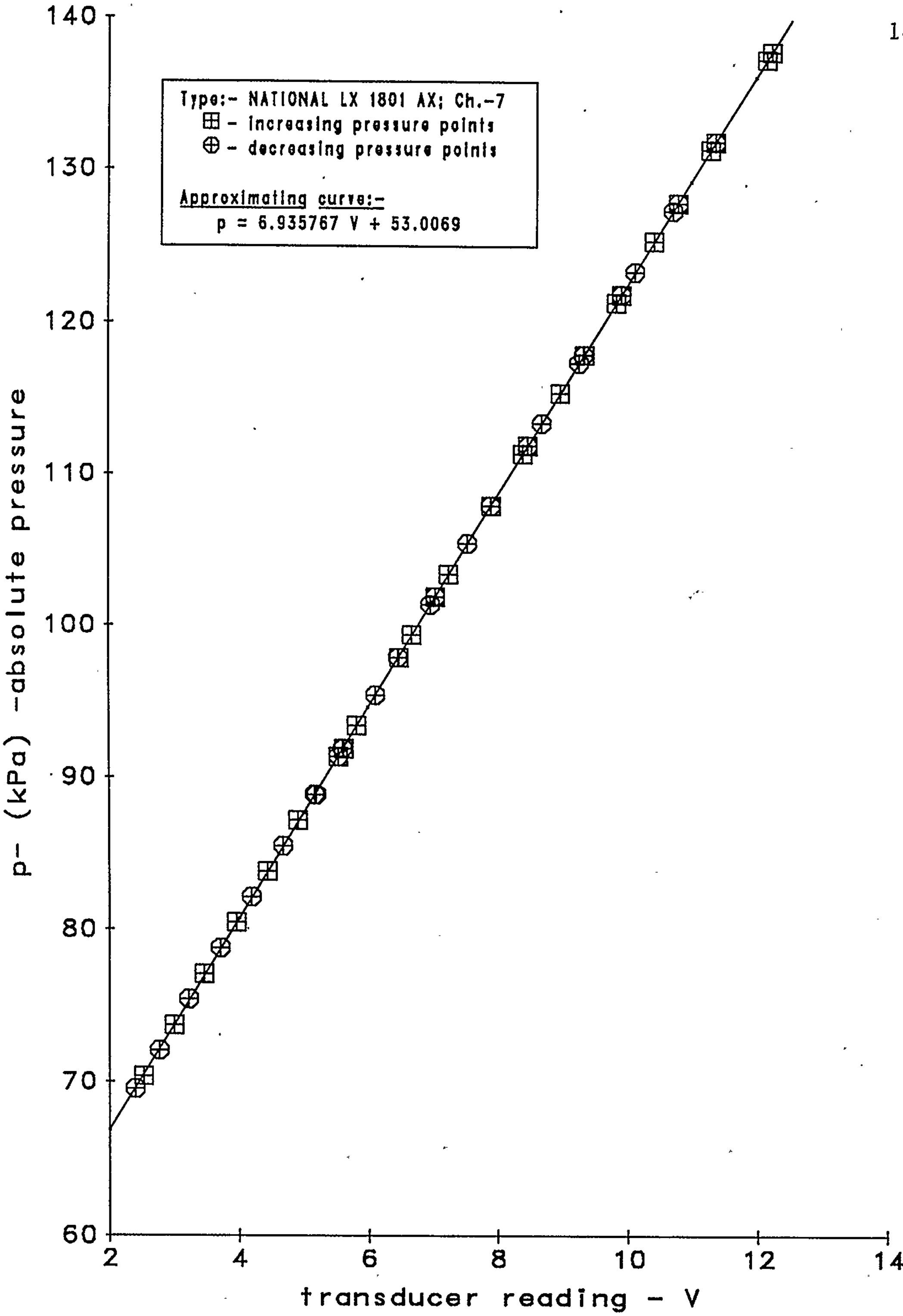

Fig.A2 Calibration of Pressure Transducer.

Type:- NATIONAL LX 1801 AX, Ch.- 7 .

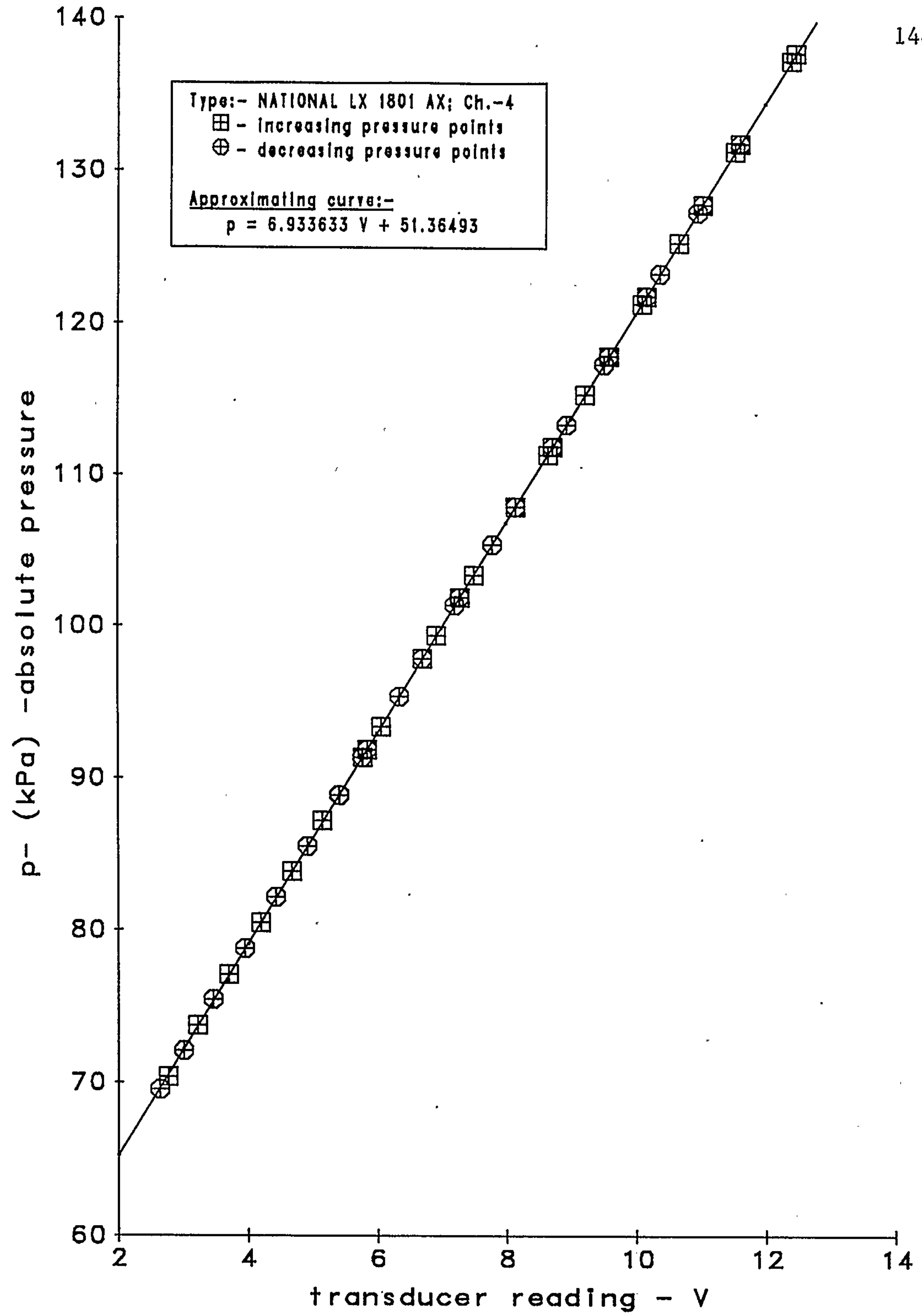

Fig.A3 Calibration of Pressure Transducer.

Type:- NATIONAL LX 1801 AX, Ch.- 4 .

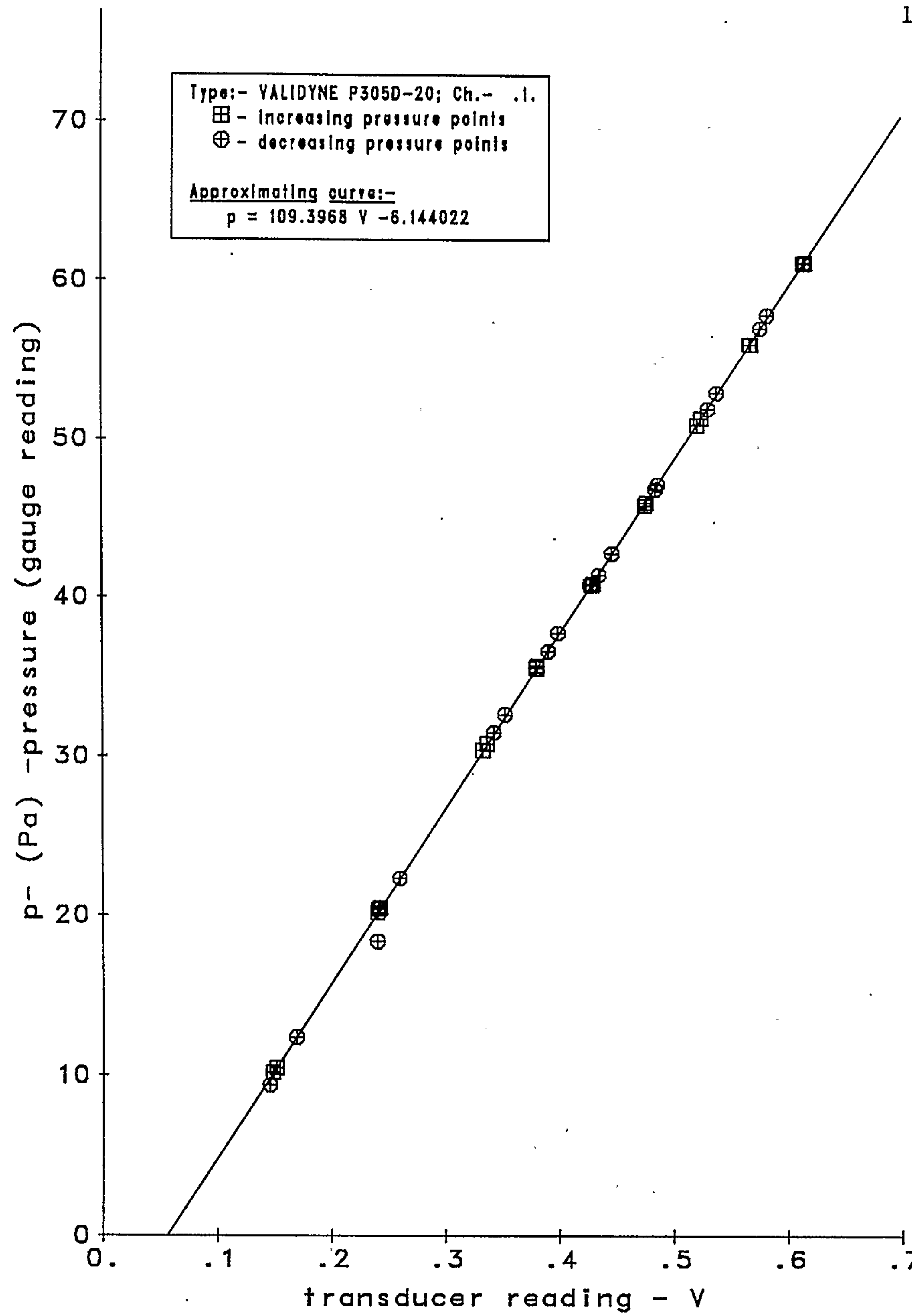

Fig.A4 Calibration of Pressure Transducer.

Type:- VALIDYNE P305D- 20; Ch.- .1.

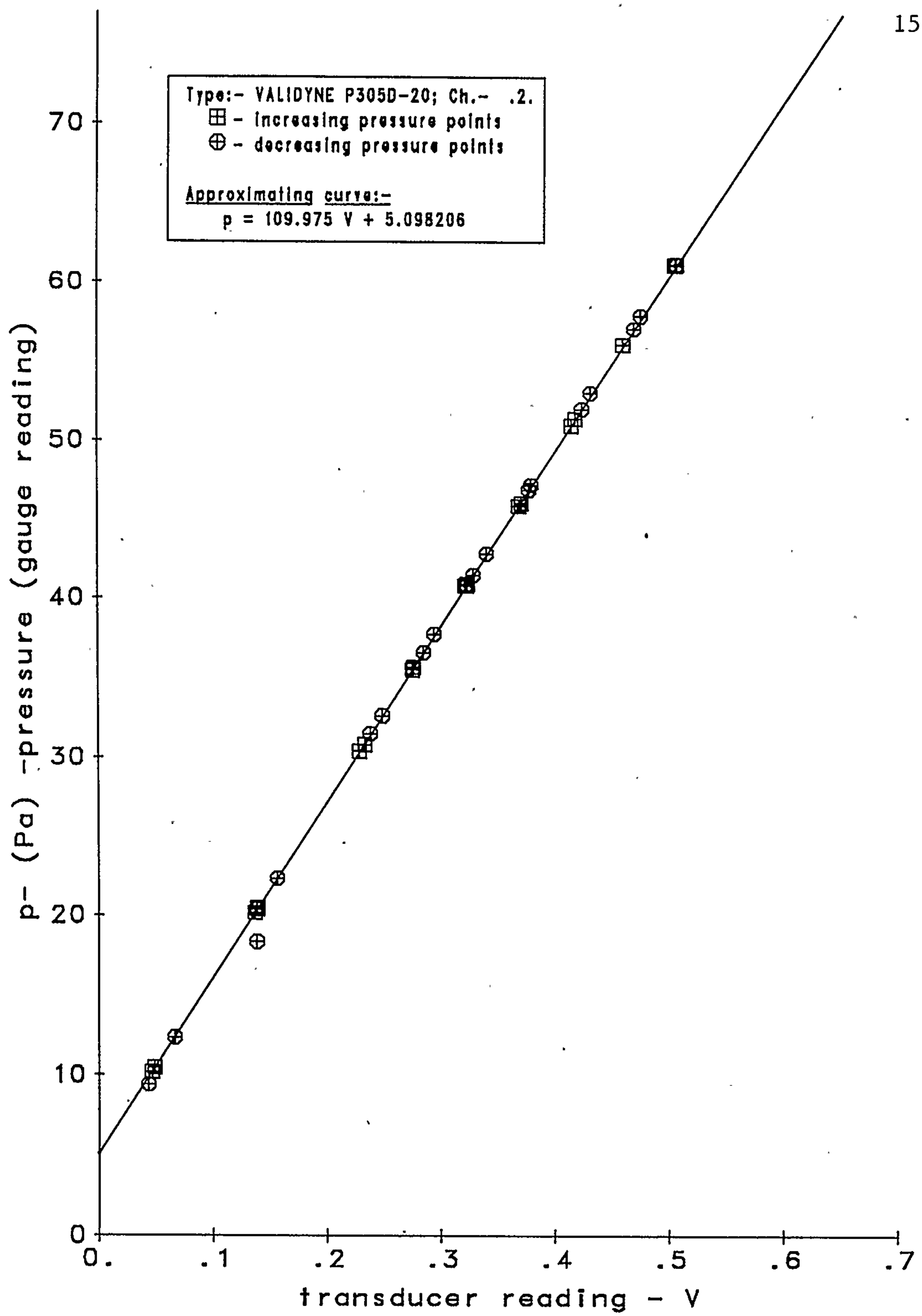

Fig.A5 Calibration of Pressure Transducer.

Type:- VALIDYNE P305D- 20; Ch.- .2.

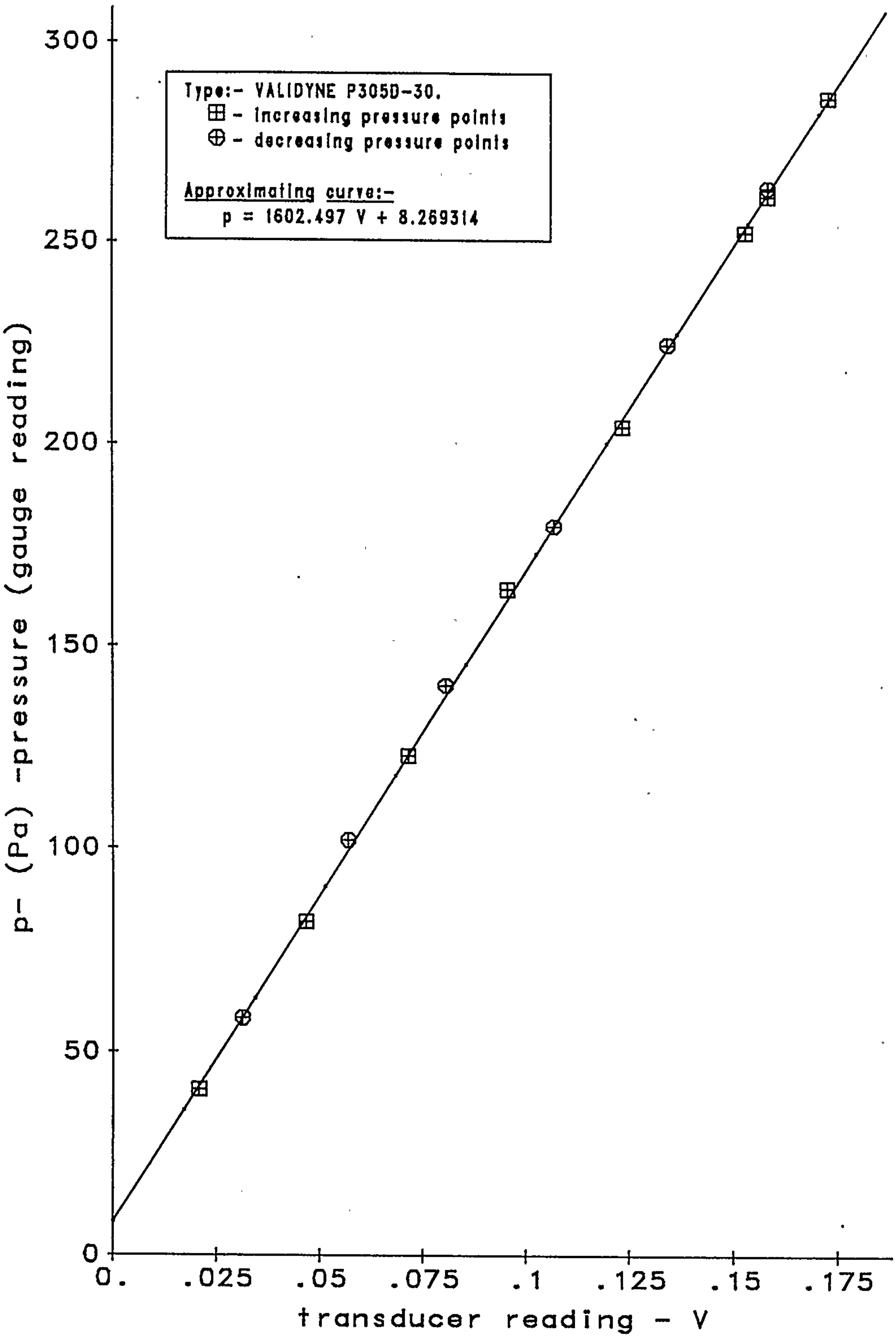

Fig.A6 Calibration of Pressure Transducer.

Type:- VALIDYNE P305D- 30.

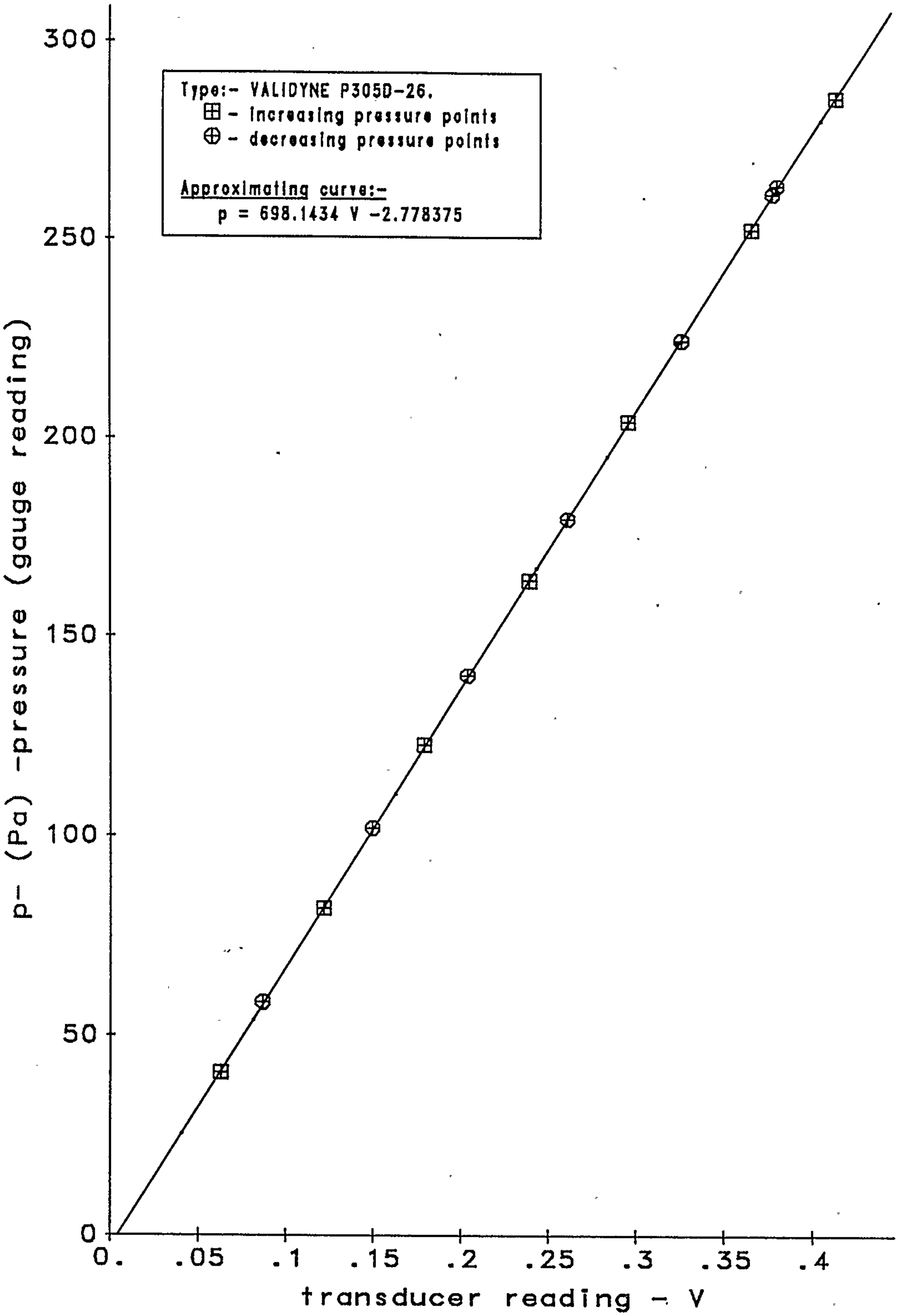

Fig.A7 Calibration of Pressure Transducer.

Type:- VALIDYNE P305D- 26.